

AD _____

GRANT NUMBER DAMD17-94-J-4133

TITLE: A Study of Ultrasonic Wavefront Distortion Compensation

PRINCIPAL INVESTIGATOR: Qing Zhu, Ph.D.

CONTRACTING ORGANIZATION: University of Pennsylvania
Philadelphia, PA 19104-3246

REPORT DATE: September 1996

TYPE OF REPORT: Annual

PREPARED FOR: Commander
U.S. Army Medical Research and Materiel Command
Fort Detrick, Frederick, Maryland 21702-5012

DISTRIBUTION STATEMENT: Approved for public release;
distribution unlimited

The views, opinions and/or findings contained in this report are those of the author(s) and should not be construed as an official Department of the Army position, policy or decision unless so designated by other documentation.

19970220 090

DTIC QUALITY INSPECTED 1

REPORT DOCUMENTATION PAGE

Form Approved
OMB No. 0704-0188

Public reporting burden for this collection of information is estimated to average 1 hour per response, including the time for reviewing instructions, searching existing data sources, gathering and maintaining the data needed, and completing and reviewing the collection of information. Send comments regarding this burden estimate or any other aspect of this collection of information, including suggestions for reducing this burden, to Washington Headquarters Services, Directorate for Information Operations and Reports, 1215 Jefferson Davis Highway, Suite 1204, Arlington, VA 22202-4302, and to the Office of Management and Budget, Paperwork Reduction Project (0704-0188), Washington, DC 20503.

1. AGENCY USE ONLY (Leave blank)		2. REPORT DATE September 1996	3. REPORT TYPE AND DATES COVERED Annual (1 Sep 95 - 31 Aug 96)	
4. TITLE AND SUBTITLE A Study of Ultrasonic Wavefront Distortion Compensation			5. FUNDING NUMBERS DAMD17-94-J-4133	
6. AUTHOR(S) Qing Zhu, Ph.D.				
7. PERFORMING ORGANIZATION NAME(S) AND ADDRESS(ES) University of Pennsylvania Philadelphia, Pennsylvania 19104-3246			8. PERFORMING ORGANIZATION REPORT NUMBER	
9. SPONSORING/MONITORING AGENCY NAME(S) AND ADDRESS(ES) Commander U.S. Army Medical Research and Materiel Command Fort Detrick, Frederick, Maryland 2170-25012			10. SPONSORING/MONITORING AGENCY REPORT NUMBER	
11. SUPPLEMENTARY NOTES				
12a. DISTRIBUTION / AVAILABILITY STATEMENT Approved for public release; distribution unlimited			12b. DISTRIBUTION CODE	
13. ABSTRACT (Maximum 200) The objective of this research is to develop ultrasonic wavefront distortion compensation methods to improve ultrasound resolution in the detection and classification of small breast lesions. A novel ultrasonic wavefront compensation technique which we call Toward Inverse Filtering (TIF) has been experimentally demonstrated last year and further analyzed since then. The well known Inverse Filtering technique is optimal for imaging fidelity but unstable. TIF approaches the performance of Inverse Filtering while demonstrates adequate stability. Experiments with breast specimens have shown that TIF represents a substantial improvement over other compensation algorithms, offering the potential for better visualization of small breast lesions. Last year, our major effects have been devoted to the understanding of TIF and further experimentation with TIF. First, the relationship of TIF with Inverse Filtering has been established, and comparisons of TIF with other compensation algorithms have been made. Second, further experimentation with TIF is in progress. In addition to TIF, another novel compensation approach which we call modified CLEAN algorithm (MCLEAN), although it has limitations in its application to breast imaging, has also been exploited. MCLEAN has shown to improve image quality by canceling coherent multipath image artifacts. The strengths and limitations of MCLEAN have been investigated.				
14. SUBJECT TERMS Breast Cancer			15. NUMBER OF PAGES 83	
			16. PRICE CODE	
17. SECURITY CLASSIFICATION OF REPORT Unclassified	18. SECURITY CLASSIFICATION OF THIS PAGE Unclassified	19. SECURITY CLASSIFICATION OF ABSTRACT Unclassified	20. LIMITATION OF ABSTRACT Unlimited	

FOREWORD

Opinions, interpretations, conclusions and recommendations are those of the author and are not necessarily endorsed by the US Army.

Where copyrighted material is quoted, permission has been obtained to use such material.

Where material from documents designated for limited distribution is quoted, permission has been obtained to use the material.

Citations of commercial organizations and trade names in this report do not constitute an official Department of Army endorsement or approval of the products or services of these organizations.

In conducting research using animals, the investigator(s) adhered to the "Guide for the Care and Use of Laboratory Animals," prepared by the Committee on Care and Use of Laboratory Animals of the Institute of Laboratory Resources, National Research Council (NIH Publication No. 86-23, Revised 1985).

For the protection of human subjects, the investigator(s) adhered to policies of applicable Federal Law 45 CFR 46.

In conducting research utilizing recombinant DNA technology, the investigator(s) adhered to current guidelines promulgated by the National Institutes of Health.

In the conduct of research utilizing recombinant DNA, the investigator(s) adhered to the NIH Guidelines for Research Involving Recombinant DNA Molecules.

In the conduct of research involving hazardous organisms, the investigator(s) adhered to the CDC-NIH Guide for Biosafety in Microbiological and Biomedical Laboratories.

OG Zhn 9/25/96
PI - Signature Date

1 INTRODUCTION.....	1
1.1 Image Degradation Caused by Ultrasonic Wavefront Distortion	1
1.2 Phase Deaberration.....	2
1.3 Compensation of Ultrasonic Wavefront Distortion.....	3
2. SUMMARIES OF ACHIEVEMENTS.....	3
3. UNDERSTANDING AND FURTHER STUDIES OF TIF	3
3.1 Understanding of the TIF Approach	3
3.2 Amplitude Distributions after Nth rooter compression.....	5
3.2.1 Theory.....	5
3.2.1 Experiments	6
4. CORRECTION OF MULTIPATH ARTIFACTS	7
4.1. Significance of Refraction upon Pulse-Echo Imaging	7
4.2. Identification of True Targets.....	7
4.3 Cancellation of False Targets	10
4. FUNDING DIFFICULTIES.....	11
5. SUMMARIES.....	11
6. PUBLICATIONS.....	12
7. REFERENCES	12

Appendices A, B and C

ANNUAL REPORT OF "A STUDY OF ULTRASONIC WAVEFRONT DISTORTION COMPENSATION"

abstract

The objective of this research is to develop ultrasonic wavefront distortion compensation methods to improve ultrasound resolution in the detection and classification of small breast lesions. A novel ultrasonic wavefront compensation technique which we call Toward Inverse Filtering (TIF) has been experimentally demonstrated last year and further analyzed since then. The well known Inverse Filtering technique is optimal for imaging fidelity but unstable. TIF approaches the performance of Inverse Filtering while demonstrates adequate stability. Experiments with breast specimens have shown that TIF represents a substantial improvement over other compensation algorithms, offering the potential for better visualization of small breast lesions. Last year, our major effects have been devoted to the understanding of TIF and further experimentation with TIF. First, the relationship of TIF with Inverse Filtering has been established, and comparisons of TIF with other compensation algorithms have been made. Second, further experimentation with TIF is in progress. In addition to TIF, another novel compensation approach which we call modified CLEAN algorithm (MCLEAN), although it has limitations in its application to breast imaging, has also been exploited. MCLEAN has shown to improve image quality by canceling coherent multipath image artifacts. The strengths and limitations of MCLEAN have been investigated.

1 INTRODUCTION

1.1 Image Degradation Caused by Ultrasonic Wavefront Distortion

Ultrasonic wavefront distortion which includes phase aberration and waveform distortion is developed as coherent waves propagate through an inhomogeneous medium, such as the breast. Wavefront distortion sources inside the breast can be modeled as incoherent scattering and coherent multipath interference. Scattering reduces the target strength, broadens the image lobe [1-2], raises the background level and therefore lowers the image contrast [3]. Multipath interference produces ghost image artifacts or false targets in addition to true targets in the image [4, App.B]. The interference problem is more severe when the aperture is large for high spatial resolution.

Fig.1 shows simple models to illustrate the effects of incoherent scattering and multipath interference upon a point source image or its angular spectrum (intensity distribution). Without medium induced distortion, we should see the diffraction limited coherent spectrum shown in Fig.1a. With the present of medium induced scattering, the overall angular spectrum is the sum of coherent and scattered spectra [5] shown in Fig.1b. Because of scattering, the spectrum is broadened and reduced in strength. The background level is increased and, therefore, image contrast is reduced. The scattered energy increases with the propagation depth. With the presence of both medium induced scattering and coherent multipath interference, the angular spectrum is the superposition of the coherent lobe, coherent interference lobes and the scattering spectrum shown in Fig.1c. The interference lobes, produced by bending and splitting of coherent waves as well as interference of coherent waves with multipath waves caused by refraction and reflection [4], appear as false targets. The strengths and the numbers of interference lobes depend on orientations, curvatures, sizes and numbers of refractive bodies in the insonified medium, and may not be directly related to propagation depth.

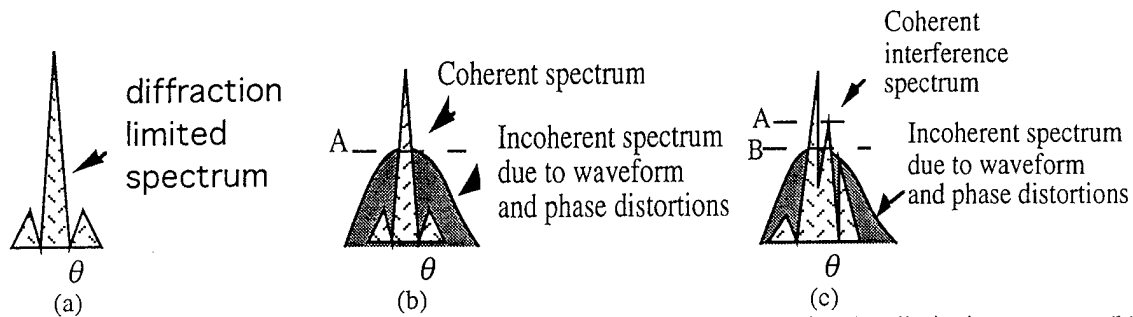


Fig.1. Statistical models of angular source intensity distribution. (a) diffraction limited spectrum. (b) Scattering induced distortion. (c) Refraction and scattering induced distortion. *These simple models are used to better visualize the distortion effect.*

1.2 Phase Deaberration

Adaptive compensation of wavefront distortion is an active area of current research [6]. Two basic phase deaberration algorithms have been developed in [7-9]. The algorithms adjust time delays of received waveforms at different elements of a phased array to compensate delay errors due to an inhomogeneous medium and consequently reduce the scattered energy. Although these two algorithms have been derived from different optimization criteria, their performances are similar; they minimize time delay errors or phase errors but leave waveform *distortion* intact [10]. But when certain correlation properties exist in the wavefront, phase deaberration algorithms are useful to partially remove phase distortion and build up the strength of the coherent field. Waveform distortion remains, as does residual phase distortion, and produces a significantly high background level in the spectrum.

Figs. 2 and 3 schematically show the effects of phase deaberration. Fig.2a shows again the distorted spectrum of Fig.1b. In Fig. 2b (a distribution that had increased coherent spectrum), the implementation of a phase deaberration algorithm results in the partial removal of phase distortion and strengthens the coherent spectrum, yet a significantly high incoherent background level remains in the spectrum due to residual phase errors and waveform distortion. Any phase-deaberration procedures that provide a better phase error estimate than that of basic algorithms would reduce this background level. Wavefront-deaberration algorithms that compensate waveform distortion can further reduce this background level [3]. In contrast, when a distribution is compensated by a phase deaberration algorithm, coherent multipath interference is affected in the following way: As shown in Fig.3a, if the primary spectrum (sharp peak) is stronger than secondary interference spectra (secondary peaks), the scattered energy removed by the phase deaberration process strengthens the primary spectrum by folding the removed scattered energy into the primary field. As a result the ratio of primary lobe to interference lobes is improved (Fig.3b). If, however, the primary spectrum is weaker than the interference spectra, the scattered energy removed by deaberration process may strengthen the interference spectra. The corrected result could therefore be worse than without correction. However, we have seen no evidence of this so far in our experiments reported in App.B.

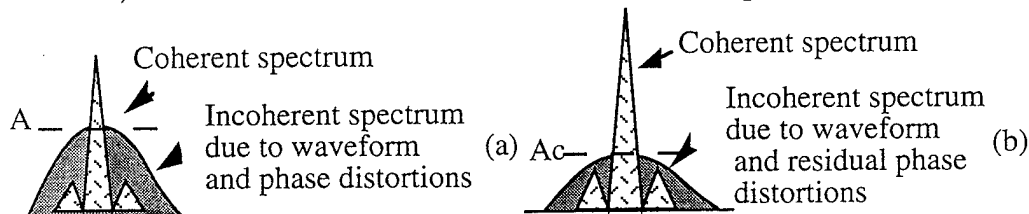


Fig. 2. (a) Distorted spectrum shown in Fig.1b. (b) After phase compensation .

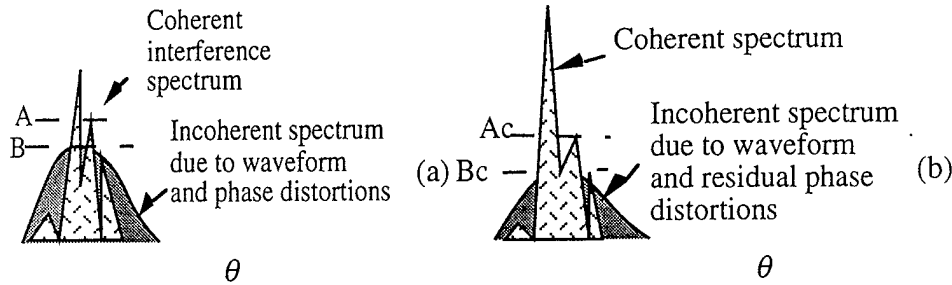


Fig. 3. (a) Distorted spectrum shown in Fig.2c. (b) After phase compensation.

1.3 Compensation of Ultrasonic Wavefront Distortion

The compensation of wavefront distortion presents a more difficult problem, because there is no general way to reduce waveform distortion. Liu and Waag [11] have improved the time-delay type compensation algorithm by backpropagating the received waveforms to an optimal distance and then performing time-delay compensation at this distance. Backpropagation partially compensates waveform distortion produced by wave propagation from the backpropagation distance to the receiving aperture. We have developed a novel Toward Inverse Filtering (TIF) algorithm which is a spectrum amplitude compression operation ([3] and App.B) that when used in combination with phase deaberration and backpropagation, provides a general means of reducing waveform distortion and therefore reducing the incoherent background level in the image.

2. SUMMARIES OF ACHIEVEMENTS

In the past, the time-delay type algorithms have been applied to *in vivo* breast data measured from one-dimensional phased arrays [12,10] and the improvement in imaging quality is not significant because of the difficulty in obtaining a good estimate of phase aberration profile and because of the *wavefront amplitude distortion*. Since wavefront aberration resulting from medium inhomogeneities has no preferred orientations, adaptive compensation, therefore, is a 2-D problem of capturing the entire 2-D wavefront and constructing a 2-D weight vector for the array. In the last two years, we found that by applying the time-delay type algorithm to *in vitro* one-way 2-D breast data, the algorithm suppressed scattered energy and folded it into the target image, restoring the mainlobe diffraction shape to the -20 dB region. [13-14]. We also found that an additional 4-5 dB improvement can be obtained by applying Liu and Waag's algorithm (App.B). With the introduction of a novel amplitude compression technique in addition to phase deaberration techniques ([3], and App.B), we are able to improve all the correction algorithms and restore the mainlobe diffraction shape down to -30 dB which is a necessary condition to image small breast lesions and lesion architecture.

In the last year, our major efforts have been devoted to the understanding and further studies of TIF.

3. UNDERSTANDING AND FURTHER STUDIES OF TIF

The improvement in image quality using TIF was demonstrated experimentally and further analysis has been performed to establish relationship of TIF with other correction algorithms.

3.1 Understanding of the TIF Approach

The following discussions use the correction of a point source image as an example to compare different correction methods and to introduce TIF. But TIF is not limited to point source targets and is applicable to a diffuse scattering medium (see App.B discussion section), such as the breast. This section is taken from App.B.

Consider complex signal vectors S_0 and S received at an array in the absence and presence of distortion, respectively. S_0 and S are functions of position in the array which is identified by element number. The multiplicative distortion $A \exp(j\phi)$ is the ratio of S to S_0 . Fig.4 shows such a distortion vector f for some instantaneous sample of the radiation field. The optimum compensation transformation is the right-most one which carries the distortion component of the complex sample to the intersection of the x-axis and the unit circle, for then both amplitude and phase are corrected. The left-most transformation is matched filtering (MF) which squares the amplitude and conjugates the phase. MF is theoretically optimum for maximizing SNR on a white, Gaussian channel. It is an optimum solution for detection (radar) but not so when fidelity is an important criterion, as in imaging. But it does satisfy the requirement for phase correction. Examples of MF algorithms are Dominant Scatterer Algorithm (DSA) [15] and Time Reversal Mirror (TRM) [16]. We should expect that MF algorithms are useful when wavefront distortion resides principally in phase, with amplitude relatively unaffected. Otherwise MF algorithms would be less effective than if amplitude were ignored and phase only were corrected. By squaring the wavefront amplitude, the MF algorithms increase amplitude variance which contributes to the increase of energy in the sidelobe region [3].

Consider what happens when a phantom consisting of a random phase screen is placed at a receiving transducer. The element signal samples are correct in amplitude and distorted only in phase by a random additive component. Phase aberration correction, consisting of phase conjugation (PC), is then the optimum compensation. The signal amplitude is unchanged and phase error is completely compensated by conjugation. This operator is represented by the 2nd (from the left) transformation. Time delay compensation (TDC) is in the same class.

The right-most transformation which corrects both amplitude and phase is the inverse filter (IF). It is theoretically ideal for fidelity but has drawbacks. Because the IF adjusts the channel gain to be the reciprocal of the signal strength, at points in the receiving aperture where signal strength is weak the enhanced channel gain raises the noise to the point where SNR can be impaired. This is particularly troublesome when there is coherent refractive interference in the receiving array. A second potential problem, which we have avoided by not working too close to the IF point, is that an IF is unstable when the distorting medium has zeroes in the complex plane. Thus the right-most transformation carries the correction too far.

The complex weights of MF, PC and IF are, respectively, A , 1 and A^{-1} , each multiplied by $\exp(-j\phi)$. The signal after weighting is A^2 , A and 1 . The first and last are far from optimum for the reasons given. The 3rd from the left transformation is a compromise. The correction vector is $A^{-1/2} \exp(-j\phi)$. The signal after weighting is $A^{1/2}$ (called later the square rooter or rooter). Another transformation to the right of the square rooter is fourth rooter (signal amplitude is $A^{1/4}$ after weighting). In general, the correction vector is $A^{-(M-1)/M} \exp(-j\phi)$ and signal amplitude is $A^{1/M}$ after transformation of the M th rooter; this operation is a ***Toward Inverse Filtering (TIF) approach***. In App., we demonstrate both theoretically and experimentally that low order rooters (square rooter and fourth rooter), in addition to phase deaberration at the aperture, can significantly improve contrast resolution without encountering stability problem.

DEABERRATION TRANSFORMATIONS

MF = matched filter (SNR)
 DSA = dominant scatterer algorithm
 TRM = time reversal mirror
 PC = phase conjugation
 TDC = time-delay compensator
 BPT = Backpropagation and
 time-delay compensation
 SR = square rooter
 (compromise amplitude weight)
 IF = inverse filter (fidelity)

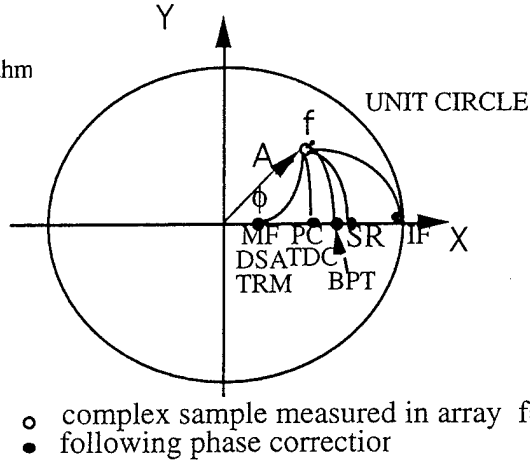


Fig.4. Deaberration transformations. f is distortion vector for instantaneous sample of the radiation field. Transformations to the real axis all correct phase. Left (MF) maximizes SNR but increases amplitude distortion. Right (IF) maximizes imaging fidelity but increases noise. SR is good compromise.

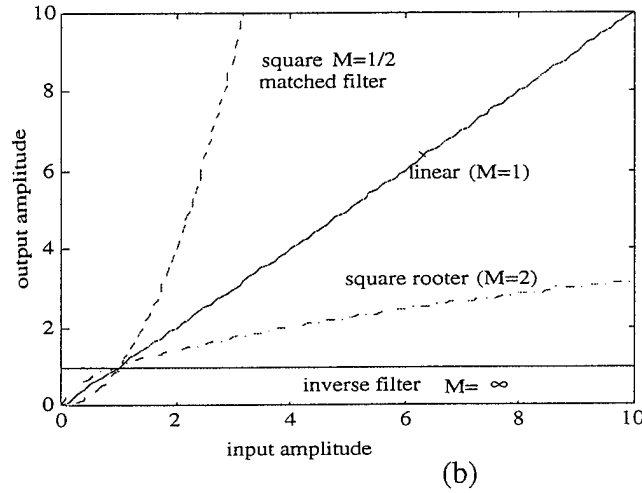


Fig.5. Plots of the input and output amplitude transforms.

Backpropagating the received wavefront to an optimal backpropagation distance and performing phase deaberration at this optimal distance (BPT) [2] provides first order correction of wavefront amplitude distortion, due to propagation from the backpropagation distance to the receiving aperture, and therefore, performs better than phase deaberration at the aperture. In App.B, we demonstrate experimentally that BPT transformation is somewhere to the right of TDC and PC and left of PC and rooter. We also demonstrate that square rooter in addition to BPT can significantly improve the performance of BPT.

The rooter transformation upon wavefront amplitude is a nonlinear compression operation (Fig.5). The detailed evaluation of the effects of this operation upon image can be performed by studying the amplitude distributions of images before and after the operation. This topic is studied in next section.

3.2 Amplitude Distributions after Nth rooter compression

3.2.1 Theory

The objective of this study is to extract scatterer characteristics, as a function of the TIF compression parameter, from TIF compressed amplitude signals. Scatterer characteristics are useful for tissue characterization.

Ultrasonic B-scan images obtained by steering a pulsed acoustic beam through a plane or a volume and positioning the echoes on a display to show their relative origin contain speckle due to constructive and destructive interference of signals from the resolution cell formed by the beam width and pulse length. The extent of speckle formation is determined by the number of backscattered echoes contributing to the received signal at the transducer at each particular instant of time. For completely random and highly concentrated scatterers, a Rayleigh distribution is used to characterize the amplitude signals of the fully developed speckle field [17]. When scatterer concentration is not high, a K distribution appears to be a more appropriate model to characterize the speckle field [18-19]. The compression operation introduced in App. alters amplitude distribution from Rayleigh or K distribution, and also changes first order statistics of amplitude. In order to extract scatterer characteristics, which are useful for tissue characterization, the amplitude distribution and first order statistics need to be studied as a function of the compression parameter N . Unlike log-compression in which the distribution and first order statistics after compression depend upon imaging systems[20-21], the N th rooter compression is independent from the system. The theoretical distribution, mean and variance of the N th rooter have been derived and are given in Table I. Rayleigh distribution has been assumed for uncompressed amplitude data. A similar study will be done with K distribution.

Table I. Amplitude Distribution and First Order Statistics

Distribution	Mean	Variance
Reyleigh $\frac{x}{\sigma^2} \exp(-\frac{x^2}{2\sigma^2})$	$\sqrt{\frac{\pi}{2}} \sigma$	$\frac{4 - \pi}{2} \sigma^2$
N th rooter $\frac{N x^{2N-1}}{\sigma^2} \exp(-\frac{x^{2N}}{2\sigma^2})$	$(2\sigma^2)^{\frac{1}{2N}} \frac{\Gamma(\frac{1}{2N})}{2N}$	$(2\sigma^2)^{\frac{1}{N}} \{ \frac{\Gamma(\frac{1}{N})}{N} - [\frac{\Gamma(\frac{1}{2N})}{2N}]^2 \}$

3.2.1 Experiments

Experimental system:

The experimental set-up is shown in the following diagram. A disk transducer which provides the focused beam at fixed distance is used for pulse-echo. The center frequency of the disk transducer is 5 MHz and the bandwidth is 80%. A 2-D synthetic aperture is formed by moving the disk transducer with a micropositioner in two dimensions. Element position accuracy is controlled within 2 microns. Each received waveform is sampled at 1024 points $/(4 \mu\text{s}/\text{Div} \times 10 \text{ Divs}) = 25 \text{ MHz}$ which is well above the Nequest sampling rate, and stored in a desktop computer. The entire experiment is under preprogrammed computer control. The output 2-D data set includes a received waveform from each receiving-element position.

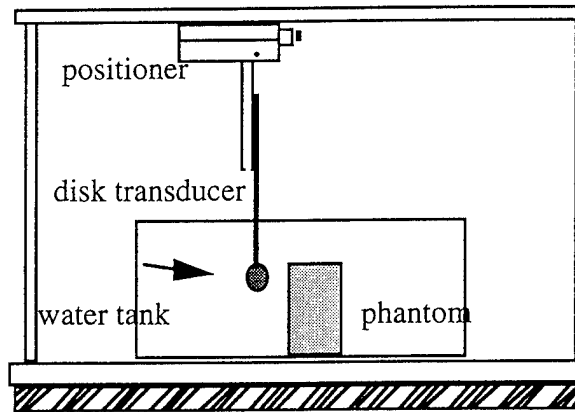


Fig. 5. A synthetic pulse echo imaging system (front view).

Experiments with Phantoms:

Experiments have been conducted with scattering phantoms to verify the theoretical results. The phantoms were made of Acrylamide gel (Boehringer Mannheim Biochemicals Corporation) which was typically used for DNA studies as an electrophoresis gel [22-23]. The gel was made in batches as needed and composed of a solution of distilled, degassed water, Acrylamide, ultrapure and Bis-Acrylamide. Scattering particles made of glass spheres (with size distribution of several μm to a few hundred μm) were added to the gel. The particle density was estimated using the method given in [24]. In order to produce polymerization, components of ammonium persulfate and tetramethylethylenediamine (known as TEMED) were also added. First experiment data indicate that the system signal-to-noise ratio is not adequate. The signal-to-noise ratio has been improved by replacing the original pulser with a reflectoscope which provides up to 750 V peak to peak transmit voltage. We should be able to obtain experimental data in a few of weeks.

4. CORRECTION OF MULTIPATH ARTIFACTS

To further increase contrast resolution, false targets produced by coherent multipath have to be canceled (see Fig3b secondary peaks). Multipath interference, however, is a much more difficult problem than scattering. Because it is not a stochastic process, two distinct steps are required to deaberrate refraction-contaminated data. It is first necessary to recognize which energy is simple scattering and which is not. The second is to remove, coherent interference energy. §4.1 discusses the significance of multipath interference. §4.2 provides in vitro evidence that subarray diversity images are useful for identification and §4.3 introduces our approach to removing multipath energy [App.C].

4.1. Significance of Refraction upon Pulse-Echo Imaging

High resolution, high dynamic range breast imaging implies seeing a black cyst 60 - 70 dB weaker than a bright speckled target. In App. B, we show that 30 dB image contrast on reception is obtainable through the use of TIF. In pulse echo, refracted energy from the targets insonified by the subbeam will arrive at angles of $1 - 3^\circ$ from the target direction (App. B) and therefore in the sidelobe region of an array. The sidelobe level of the receiving beam will be ~ -30 dB. The average level of refracted multipath is found to be -10 dB relative to the target image (App. B) and therefore the average multipath signal level entering the system is $\sim (10+30)$ dB = -40 dB below the echo strength of the illuminated target. Cancellation algorithms must suppress these multipath signals to achieve 60 - 70 dB contrast resolution. Hence about 20 - 30 dB further cancellation is required.

4.2. Identification of True Targets

Principle: We have found that geometric techniques may be able to provide false target identification information. Fig.6 illustrates the case where a single source and 1-D reception are used for descriptive convenience. The same principle is applicable to a multiple source distribution and 2-D configuration. A source radiates into a scattering and refractive medium and its radiation field is received by a receiving aperture. The source image obtained from any aperture is the superposition of the image lobe, image artifacts caused by coherent interference and an incoherent scatter spectrum. The location of the image lobe generally remains the same when viewed from different apertures, such as the left and right halves of the aperture, while the locations, sizes and shapes of the image artifacts are likely to change because the fields intercepted by different subapertures encounter refractive bodies with different orientations, curvatures and sizes. The incoherent spectrum is statistically the same in each subaperture image. Therefore, the locations of the large lobes in different subaperture images can be used to distinguish the image lobe from image artifacts.

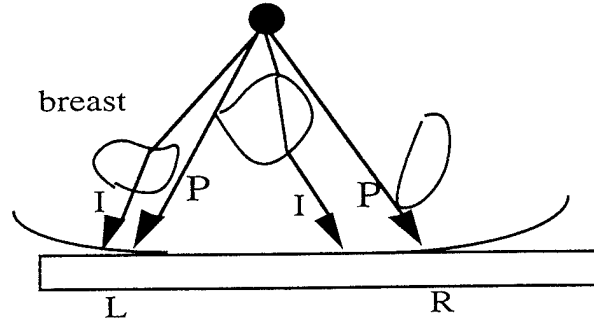


Fig.6. Illustration of diversity. P refers primary field and I interference field. The interference fields change with propagation path.

Experiments: The 2-D measurement system and procedure were described by Hinkelmann et al. [14]. Fig.7 illustrates the set-up of the measurement system. A breast specimen was placed between a hemispherical source and a 2-D receiving array. The 2-D array consisted of a 92-mm 1-D linear array translated 46 mm perpendicular to its axis to form a synthetic 2-D array 92 mm x 46 mm. Element pitch in the receiving transducer was 0.72 mm and a reflecting mask reduced the receiving elevation to 1.44 mm. The frequency was 3.7 MHz and the bandwidth was 2 MHz. Waveforms were measured at each element, from which 2-D wavefronts were reconstructed as functions of time. 3-D image data were calculated by using the angular spectrum technique. The final 2-D image is obtained by detecting the peak pressure value at each position in the image plane within the transient period.

Results: Fig. 8 shows an example of single-frequency diversity images. Part (a) is the -20 dB contour of the entire aperture image brs006 and (b) is the same sample image after applying time-delay correction (TDC). The improvement is significant because of partial removal of scattered energy. Large multipath lobes remain and decrease image contrast. (c)-(f) are obtained from four subapertures after applying TDC. The real target remains in the same location (center lobe). False targets move and change size and shapes when viewed from the different subapertures. For example, the lobe with -13 strength located at (4.3 mm, 2.9 mm) in (b) does not appear in (c), therefore it is a false target and should be removed.

From our *in vitro* samples (9 out of 16) that have well-defined multipath, we found that 2-D subarray diversity images in general are useful for identification while 1-D subarray images fail to provide identification most of the time because of incomplete

distortion information. From our three pairs of measurements with two sources located 12 mm apart, we also found 2-D subarray diversity images are useful for identification. However, when two sources are located close to each other, the constructive and destructive interference of real targets with the multipath targets may create difficulty in identification.

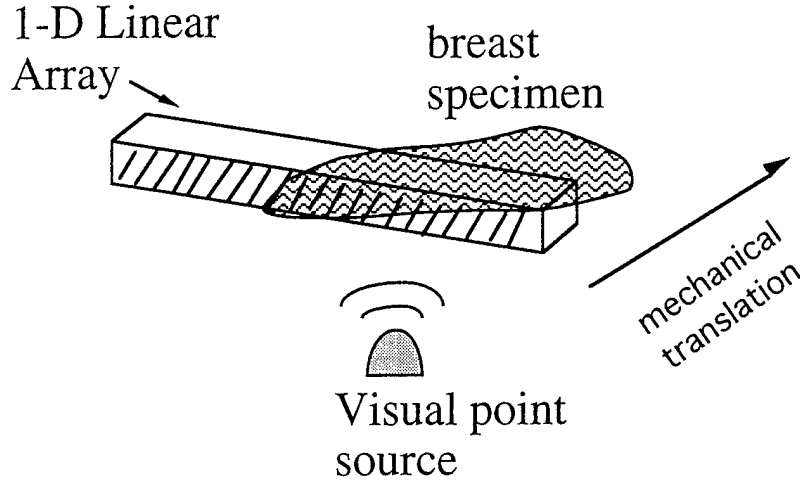


Fig.7. 2-D in vitro measurement system of University of Rochester.

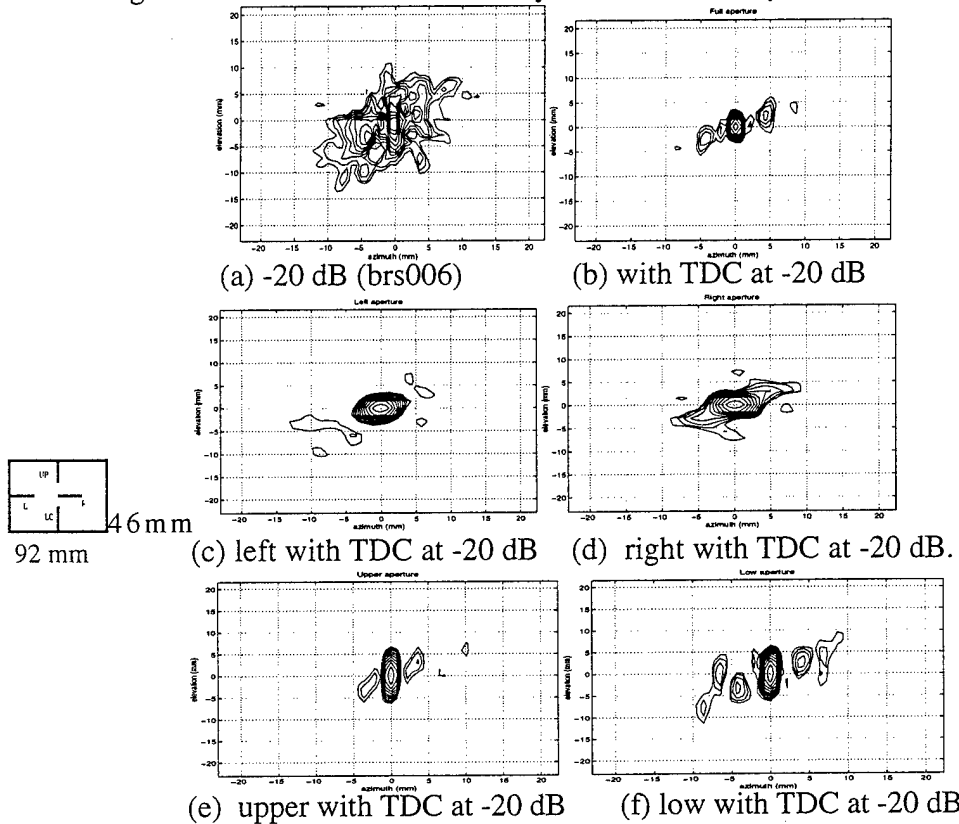


Fig.8. Quadruple spatial diversity discloses false targets. Images are obtained at center frequency. Contour maps are at -20 dB level. Real target remains in place in subarray images while multipath target changes location, size and shape. (a) Contour map of the full-aperture image brs006 at -20 dB before TDC (b) Contour map of the same sample at -20 dB after TDC. (c) Image from left half of array after TDC. 46x 46 mm. (c) From right half after TDC. (d) From upper half (23x92mm) after TDC. (e) From low half after TDC.

4.3 Cancellation of False Targets

Once the true targets are distinguished from the false ones, CLEAN which will be described later or some other cancellation procedure has to be performed to reconstruct the original refractive artifact-free scene or to cancel the false targets.

CLEAN is a nonlinear deconvolution procedure originated in radio astronomy in the 1960s [25], extended to radar in 1980s [26] and applied to ultrasound in 1990s[27]. The simplest CLEAN procedure is described as following. The diffraction pattern $f(u)$ is shown in Fig.9a. The procedure begins with the original dirty image $A_0(u)$ (Fig.9b). The strongest source is found and its complex amplitude a_0 and coordinates u_0 are measured. An image of that source is found by convolving the radiation pattern with a δ -function of strength a_0 located at u_0 (Fig.9b). Some fraction of this image is subtracted from $A_0(u)$. The result of this first iteration is a new image, $A_1(u)$,

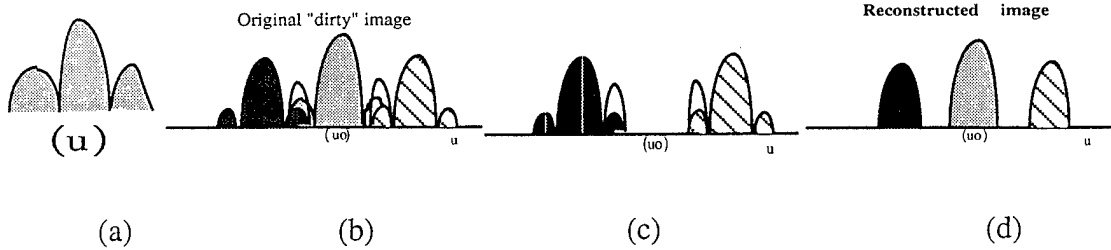


Fig. 9 Illustration of the clean procedure. (a) "Dirty image" of three point targets is the envelope of the coherent sum of the three images. (b) After the first iteration of the clean procedure. The strongest target is subtracted out as well as its sidelobes. Final result of cancellation process is a list of targets (strengths and locations) $A_i \delta(u - u_i)$. (c) Final reconstructed image $= \sum_i A_i \delta(u - u_i) * f(u)$.

from which all energy from the strongest source has been removed, including its sidelobe energy (Fig.9c). The process continues until the subtraction procedure produces images with negative values. The result at this stage is a list of detected sources. The next step is to calculate a CLEAN beam that has the resolving power of $f(u)$ but without its sidelobe distortion. The final image is the convolution of the CLEAN beam and each of the detected sources (Fig.9d).

However, the above CLEAN procedure cannot be directly applied to an image that is contaminated by image artifacts, because CLEAN will pick up true targets as well as false targets. A clever use of CLEAN is to apply it to true targets only after first identifying them, which are found by the diversity technique described above and demonstrated in in previous section.

The above modified CLEAN (MCLEAN) procedure is done at each frequency after Fourier decomposition of wideband pulses. The 3-D transient image is obtained by summation of the 2-D MCLEANed images at all discrete frequencies. Fig.10a is the narrowband image of Fig.8b at -30 dB contour after coherent CLEAN. CLEAN has picked up 30 false targets in addition to the true target. After location diversity, all false targets are identified. Table I in App. C gives the identification result of this example. No misclassification occurs in this frequency. The peak of the noise floor after CLEAN is 23.4 dB lower than the peak value before CLEAN. Since the original peak artifact to peak target ratio is -13.0 dB, the dynamic range has been improved by 10.4 dB using MCLEAN. MCLEAN has been repeated on all 39 discrete frequencies. Two misclassifications occur in two CW images. In one case, a false target was identified as true and in another true was identified as false. However, these cases happen in CW images obtained from the low and/or high frequency ends where the signal to noise ratio is low. Fig.10b is the MCLEANed wideband sample image, after peak detection of the 3-D transient image, at -30 dB level. The wideband water path image at -30 dB shown in

Fig.10c can be used for comparison. The false target which appeared at one frequency does not contribute much to the final wideband image because of its low strength. The true target, which was identified as false, was removed before the summation to form the 3-D wideband image. The result is the 0.01 dB reduction of the true target strength compared with its strength before MCLEAN. The peak of the wideband noise floor after MCLEAN is -25.1 dB lower than the peak value of the true target before MCLEAN. Since the peak artifact to peak target ratio in wideband image before MCLEAN is -14.5 dB, the dynamic range has been improved by 10.6 dB by MCLEAN.

The statistics of the performance of MCLEAN upon 7 samples with well-defined multipath artifacts are given in Table II of App. C. An average of 7.3 dB dynamic range improvement is obtained with negligible target strength reduction.

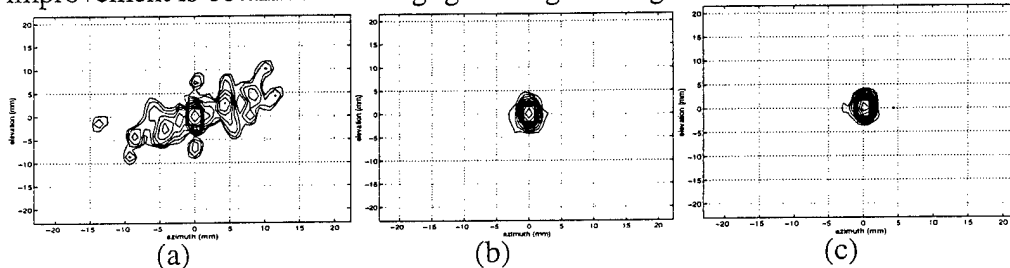


Fig.10. (a) Reconstructed image of Fig.7(c) at -30 dB level after coherent CLEAN. (b) -30 dB contour of 3-D transient MCLEANed image of brs006 after peak detection. (c) -30 dB contour of water path image.

The diffraction pattern used in App. C was only modified by varying the focusing speed to match the distorted mainlobe as well as refractive lobes to obtain better subtraction. The dynamic range can be further improved if the diffraction pattern is modified by perturbing higher order focusing terms to improve the subtraction.

The coherent CLEAN described above is based on the assumption that the scene consists of isolated and independent targets. However, this assumption does not hold well in breast ultrasound imagery as most scenes contain contiguous or diffuse targets. Therefore, this method has limitations in its application to breast imaging.

4. FUNDING DIFFICULTIES

The matching fund for this project (US ARM, DAMD 17-93-J-3014) was ended by December 1995. Since then, PI was not able to devote 100% of her effort to this project. Furthermore, there is no budget in this grant to purchase materials necessary for the continuation of this research. Efforts have also been devoted to preparing proposals to NIH and Whitaker Foundation to seek more funding for this research.

5. SUMMARIES

Previous studies indicate that ultrasonic wavefront distortion sources inside the breast are incoherent scattering and coherent multipath interference. Scattering reduces the target strength, broadens the image lobe, raises the background level and therefore lowers the image contrast. Multipath interference produces ghost image artifacts or false targets in addition to true targets in the image. A novel ultrasonic wavefront compensation technique which we call Toward Inverse Filtering (TIF) is aimed at compensating the scattering induced distortion upon breast imaging. Analysis and experiments with breast specimens have shown that TIF affords a substantial improvement in image contrast over other compensation algorithms, offering the potential for better visualization of small breast lesions. Further studies of TIF are planned or in progress. Coherent multipath interference is a much difficult problem, because it is not a stochastic process. we have developed a novel compensation approach which we call modified CLEAN algorithm (MCLEAN).

MCLEAN has shown to improve image quality by canceling coherent multipath image artifacts, but it has limitations in its application to breast imaging.

6. PUBLICATIONS

Journal Publications

1. Zhu, Q., Steinberg, B. D., "Modelling and Correction of Incoherent Wavefront Distortion," Special issue of *Anal. J. Sci. Tech. Imaging* (invited), Wiley, in press.
2. Zhu, Q., Steinberg, B. D. "Wavefront Deaberration: An Toward Inverse Filtering Approach," submitted to *IEEE Transactions on Ultrasonics, Ferroelectrics, and Frequency Control*, (April 15, 1996).
3. Zhu, Q. and Steinberg, B.D., "Correction of Multipath Interference by Spatial Location Diversity and Coherent CLEAN," *Proc. IEEE Ultrasonic Symp.* 1367-1370 (Nov.1995)
4. Zhu, Q., Correction of Ultrasonic Wavefront Distortion," 38 Annual Meeting of American Association of Physicists in Medicine, Philadelphia, PA (July 1996) (invited talk).

Future Presentations

1. Zhu, Q. and Steinberg, B.D., "A Toward Inverse Filtering Approach for Wavefront Deaberration," 1996 IEEE Ultrasonics Symposium, San Antonio, Texas November 3-6, 1996.
2. Zhu, Q., Steinberg, B.D. and Sullivan, D., "Compensation of Acoustic Wavefront Distortion," Radiological Society of North America, Dec. 1996.

7. REFERENCES

- [1] Moshfeghi, M. and Waag, R.C., In Vivo and in Vitro Ultrasound Beam Distortion Measurements of a Large Aperture and a Conventional Aperture Focused Transducer, *Ultrasound Med. Biol.* 5, 415-428 (1988).
- [2] Trahey, G.E., Freiburger, P.D., Nock, L.F., and Sullivan, D.C., "In Vivo Measurements of Ultrasonic Beam Distortion in the Breast," *Ultrason. Imag.* 13, 71-90 (1991).
- [3] Zhu, Q. and Steinberg, B.D., "Modelling and Correction of Incoherent Wavefront Distortion," Invited paper, *Anal. J. Sci. Tech. Imaging*, Wiley, (in press).
- [4] Zhu, Q. and B. D. Steinberg, "Large-Transducer Measurements of Wavefront Distortion in the Female Breast," *Ultrasonic Imaging* 14: 276-299 (1992).
- [5] Ishimaru, A. (1978), *Wave Propagation and Scattering in Random Media*, Academic Press, New York.
- [6] Wavefront Deaberration Workshop, In conjunction with 20th International Symposium on Ultrasonic Imaging and Tissue Characterization, June 7-9, 1995, Arlington, VA.
- [7] Flax, S. W. and O'Donnell, M. "Phase Aberration Correction using Signals from Point Reflectors and Diffuse Scatterers: Basic Principles," *IEEE Trans. Ultrason. Ferroelec. Freq. Cont.*, 35(6):758-767, Nov. 1988.
- [8] Nock, L., Trahey, G. E., and Smith, S.W., "Phase Aberration Correction in Medical Ultrasound Using Speckle Brightness as a Quality Factor," *J. Acoust. Soc. Am.*, 85(5) 1819-1833 (1989).
- [9] Attia, E.H. and Steinberg, B.D. (1989), "Self-Cohering Large Antenna Arrays Using the Spatial Correlation Properties of Radar Clutter," *IEEE Trans. Antennas Prop.*, AP-37(1), 30-38.
- [10] Zhu, Q., Steinberg, B. D. and Arenson, R., "Wavefront Amplitude Distortion and Image Sidelobe Levels -Part II: In Vivo Experiments," *IEEE Transactions on Ultrasonic, Ferroelectrics and Frequency Control* (40) 754-761 (1993).

- [11] Liu D-L and Waag, R.C., "Correction of Ultrasonic Wavefront Distortion Using Backpropagation and Reference Waveform Method for Time-shift Compensation," J. Acoust. Soc. Am. 96, 649-660 (1994).
- [12] Freiburger, P.D., Sullivan, D.C., LeBlanc, B. H., Smith, S. W., and Trahey, G.E., "Two Dimensional Ultrasonic Beam Distortion in the Breast: In vivo measurements and effects," Ultrason. Imag. 14(4), 398-414 (1992).
- [13] Zhu, Q. and Steinberg, B. D., "Modeling, Measurement and Correction of Wavefront Distortion Produced By Breast Specimens," Proc. IEEE Int'l Symp. Ultrason. Ferroelec. Freq. Contr., Cannes, Nov. 1994.
- [14] Hinkleman, L.M., Liu, D-L., Waag, R.C., Q. Zhu and B.D.Steinberg, "Measurement and correction of ultrasonic pulse distortion produced by the human breast," JASA (97) No.3, 1958-1969 (1995).
- [15] Steinberg,B.D, "Radar Imaging from a Distorted Array: The Radio Camera Algorithm and Experiments," IEEE. Trans. Antennas Propag., **AP-29**(5) 740-748 (Sept. 1981).
- [16] Fink, M., "Time reversal of ultrasonic fields – part I: basic principles," IEEE Trans. Ultrason. Ferroelec. Freq. Contr., vol. 39, pp. 555-566, 1992.
- [17] J.W. Goodman, "Statistical properties of laser speckle patterns," in laser speckle and related phenomena, edited by J.C. Dainty (Springer-verlag, berlin, 1984).
- [18] L. Weng, J.M. Reid, P. Mohana Shankar, and K. Soetanto, "Ultrasound speckle analysis based on the K distribution," J. Acoust. Soc. Amer., vol. 89, no. 6, pp. 2992-2995, June 1991.
- [19] Narayanan V. M., Shankar, P. M., and Reid, J. M., " Non-Rayleigh Statistics of Ultrasound Backscattered Signals," IEEE Trans. Ultrason. Ferroelec. Freq. Contr., vol 41, No.6., November, 1994.
- [20] Kaplan, D and Ma, Q., "On the Statistical Characteristics of Log-compressed Rayleigh Signals: Theoretical Formulation and Experimental Results," J. Acoust. Soc. Am. 95 (3), March 1994.
- [21] Dutt, V. and Greenleaf J., " Statistics of the log-compressed echo envelope," J. Acoust. Soc. Am. 99(6), June 1996.
- [22] Weng, Li, Ph.D Dissertation, Dept. of Biomedical Engineering and Science Institute, Drexel University, PA, 1990.
- [23] Molthen, RC, Ph.D Dissertation, Dept. of Biomedical Engineering and Science Institute, Drexel University, PA, 1996.
- [24] Sleaf G. E., and Lele P., "Tissue Characterization based on scatterer number density estimation," IEEE IEEE Trans. Ultrason. Ferroelec. Freq. Contr., vol 35, No.6., November.
- [25] Hobbom, J. A., "Aperture Synthesis with Non-Regular Distribution of Interferometer Baselines," Astron. Astrophys. Suppl., Vol. 15, pp. 417-426, 1974.
- [26] Tsao, J. and B.D. Steinberg, "Reduction of Sidelobe and Speckle Artifacts in Microwave Imaging: The Clean Technique," IEEE Trans. Antennas and Prop., Vol. 36, No. 4, April 1988, pp. 543- 556.
- [27] Cohen, N., "Practical real-time deconvolution and image enhancement of medical ultrasound," Biological Image Processing and 3D Microscopy, ed. by R. Acharya, C. Cogswell and D. Goldgof, SPIE, Bellingham WA 1992.

Appendices

Appendix A: Zhu, Q. and Steinberg, B. D., "Modeling and Correction of Incoherent Wavefront Distortion" will appear in special issue of International Journal of Imaging Systems and Technology . Invited.

Appendix B: Zhu, Q. and Steinberg, "Deaberration of Incoherent Wavefront Distortion: An Approach Toward Inverse Filtering," submitted to IEEE Transactions on Ultrasonic, Ferroelectrics and Frequency Control (April 16 1996).

Appendix C: Zhu, Q. and Steinberg, B.D., "Correction of Multipath Interference by Spatial Location Diversity and Coherent CLEAN", Proc. of IEEE Ultrasonic Symposium, Seattle Washington, 1367-1370 (Nov.1995).

Will appear in Special Issue of International Journal
of Imaging Systems and Technology, Wiley
(invited)

Modelling and Correction of Incoherent Wavefront Distortion

Qing Zhu, Department of Radiology
Bernard Steinberg, Valley Forge Research Center, The Moore School of Electrical
Engineering, University of Pennsylvania, Philadelphia, PA 19104

ABSTRACT — There are two types of wavefront distortion inside the female breast, incoherent scattering and coherent interference. Adaptive wavefront compensation algorithms developed so far are useful for correction of incoherent distortion caused by scattering. The performances of these algorithms differ according to the extent of wavefront amplitude distortion. It is shown analytically and experimentally in this paper that the matched filtering approach while optimal for detection is not so for imaging when the wavefront amplitude is distorted in addition to phasefront distortion. Matched filtering algorithms increase wavefront amplitude variance and therefore decrease image contrast. The inverse filtering approach while ideal for fidelity is not stable when SNR is low. An approach toward inverse filtering, amplitude compression operation in addition to phase deaberration, is introduced in this paper. Analysis and experiments show that its performance is superior to matched filtering algorithms and to time-delay type correction algorithms without introducing stability problems.

I. INTRODUCTION

In principle, high ultrasound resolution can be achieved with very large ultrasound transducers. However, large transducers are more susceptible to wavefront distortion caused by inhomogeneous tissue because the transducers cover large volumes of tissue and the beams interact with more spatial variations in tissue composition. The distortion inside the female breast falls into two categories: incoherent scattering reduces the target strength, broadens the image lobe [1-2] and raises the background level and therefore lowers the image contrast [3-4]. Refraction creates coherent multipath interference that produces false targets or image artifacts in addition to true targets in the image [10],[4]. The interference problem is more severe when the aperture is large.

Numerous efforts have been made to correct wavefront distortion produced by breast, liver and abdominal wall [9],[13-17]. Basic deaberration algorithms [5-7] are recognized to be suitable only for weak scattering that can be modeled as a thin random phase screen located in the plane of the receiving aperture [8-9],[18]. Extensions of the basic algorithms are made to correct amplitude distortion caused by strong scattering or distributed scattering [8-9]. A model-based approach, that used *a priori* information of the speeds of the rectus muscle layers inside the abdominal wall, has been developed to correct double image artifacts caused by refraction [17]. The proposed technique is not model based and therefore is freed from the necessity of having a prior information about the source of the distortion.

The motivation of this study stems from the following. The algorithms [5-9] that require no *a priori* knowledge about the propagating medium function differently upon

incoherent scattering and coherent interference; therefore it is important to understand the effects of the two distortion processes upon the image and then apply suitable correction mechanisms to the algorithms. The scattered energy increases with the propagation depth in the breast; therefore the performance of descattering algorithms [5-9] is expected to deteriorate with depth. Modeling and quantification of depth dependent distortion and correction are extremely valuable for the design of next generation high quality breast scanners.

In this paper we analyze, through modeling and experiment, image distortion caused by scattering and coherent interference, and the extent to which image quality improvements are affected by deaberration. Wavefront compensation algorithms based on matched filtering are first recognized to be unsuitable for imaging in distributed scattering because the algorithms increase wavefront amplitude distortion and therefore decrease image contrast. A compression operation on wavefront amplitude, akin to inverse filtering, which can significantly reduce wavefront amplitude variance is introduced. We demonstrate through experiments that a combination of the amplitude compression and either phase-deaberration at the aperture or backpropagation plus phase-deaberration at some optimal distance from the aperture can significantly improve image contrast and restore the mainlobe diffraction shape to a -30 dB level. Linear regression analysis of sidelobe energy vs. propagation depth from available data indicates that good focusing with high contrast resolution throughout the 100 mm propagation depth by deaberration is possible.

II. SCATTERING MODELS

The wave propagation problem is formulated similarly to the line-of-sight propagation problem through a tenuous distribution of particles [19]. A narrowband wave is used to simplify the description and derivation. The analytic results can be taken as rules of thumb applicable to the wideband case to characterize contrast resolution due to wavefront amplitude and phase distortions.

An ultrasound wave (either spherical or planar) propagates in an inhomogeneous medium (Fig.1). It consists of coherent and incoherent waves. The incoherent wave is also called a scattered wave. As the wave propagates, the coherent intensity I_c is attenuated due to absorption and scatter, and the incoherent intensity I_i is scattered broadly.

A. Weak Scattering

The field E at a receiving aperture is predominantly coherent and the magnitude of the incoherent field is much smaller than that of the coherent field. E is the sum of the coherent and incoherent fields.

$$E(x) = E_c(x) + E_i(x) \quad (1)$$

$$E_c(x) \gg E_i(x), \quad \langle E_c(x_1)E_i(x_2) \rangle = 0 \text{ and } \langle E_i(x) \rangle = 0 \quad (2)$$

where $\langle \rangle$ is the ensemble average and x is the spatial variable at the receiving aperture.

The spatial correlation or mutual coherence function of the field at the aperture is given by $\Gamma = \langle E(x_1)E(x_2) \rangle$. Since $\langle E_i(x) \rangle = 0$ and $\langle E_c(x_1)E_i(x_2) \rangle = 0$, the spatial correlation function satisfies $\Gamma = \Gamma_c + \Gamma_i$. If the receiver is located in the far field or within the focal region of the source, the angular source intensity distribution or intensity image is the Fourier transform of the spatial correlation function and equals the summation of the coherent and *statistically* smoothed symmetrical incoherent spectra (Fig.2(a)). For each realization, however, the incoherent spectrum can have valleys and hills. The Fourier relationship between the incoherent spatial correlation function Γ_i and incoherent spectrum is commonly known as the Van-Cittert Zernike theory [20].

The wavefront distortion is primarily in the phasefront and can be modeled approximately as due to a thin, random phase screen located in the plane of the receiving aperture and defined by a spatial correlation distance. Such distortion is correctable by phase-deaberration or time-delay compensation algorithms [5-7]. The algorithms operate upon the incoherent field. They fold the scattered energy into the coherent field and thereby restore the full diffraction-limited image (Fig.2(b)).

The most relevant wavefront measurement in a weak scattering field is the spatial correlation function of the phasefront or time-delay profile as reported by several groups [1],[16],[21-22]. From this information, the performance of the phase deaberration process can be predicted.

B. Strong Scattering or Distributed Scattering

The coherent component is attenuated and the incoherent component is scattered broadly. Wavefront amplitude is distorted in addition to phasefront distortion. A more suitable representation of the field is the Rytov model. A distributed random distortion medium can be represented as a cascade of thin, independent distortion layers (Fig.3(a)) or phase screens [19]. At the i th layer, the field can be written as $E_i = A_i \exp(j\phi_i)$. Phasefront distortion is developed due to time shift through each layer. Wavefront amplitude distortion is developed as the phase-aberrated wavefront propagates through the medium to successive layers (Fig.3(b)). Let $E_0 = A_0 \exp(j\phi_0)$ be the reference field. The distorted field is then a product of contributions from each layer

$$E(x) = E_0 E_1 E_2 \dots E_i \dots E_N \quad (3)$$

The amplitude of $\frac{E(x)}{E_0(x)}$ denoted as A_t is $A_t = A_1 A_2 \dots A_i \dots A_N$ and the phase $\phi_t = \phi_1 + \phi_2 + \dots \phi_i \dots + \phi_N$. Assume that the layers are statistically independent and have common statistics; therefore $A_i = \bar{A} + \delta A_i$ and

$$A_t = (\bar{A})^N \prod_{i=1}^N (1 + \frac{\delta A_i}{\bar{A}}) = (\bar{A})^N (1 + \sum_{i=1}^N \frac{\delta A_i}{\bar{A}} + \text{higher order products}) \quad (4)$$

Since \bar{A} is close to unity and $\frac{\delta A_i}{\bar{A}}$, $i=1,2,\dots,N$, are independent variables, the amplitude variance of A_t normalized to $(\bar{A})^N$ is $\sigma_{A_t}^2 \approx N \sigma_{\frac{\delta A}{\bar{A}}}^2$, where $\sigma_{\frac{\delta A}{\bar{A}}}^2$ is the normalized amplitude variance of a single screen. $\sigma_{A_t}^2$ grows linearly with the total number of phase screens N and therefore with the propagation distance D . The phase variance $\sigma_{\phi_t}^2 = N \sigma_{\phi}^2$, where σ_{ϕ}^2 is the variance of a single phase screen; therefore $\sigma_{\phi_t}^2$ grows linearly with N and D .

The overall spectrum (sum of coherent and incoherent spectra) is broadened (see outline of Fig.4(a)) and reduced in strength. The background level is increased and therefore image contrast is reduced.

The scattered energy increases with the propagation depth. The energy ratio (ER), which is the energy outside the main image lobe to the energy inside the main image lobe, is a useful tool to quantitatively evaluate the depth-dependence distortion upon image contrast. The relationship between ER and propagation depth D (see Appendix for derivation) is

$$ER = C(\sigma_{\phi}^2 + \sigma_{A_t}^2) = CN(\sigma_{\phi}^2 + \sigma_{\frac{\delta A}{\lambda}}^2) = C \frac{D}{d} (\sigma_{\phi}^2 + \sigma_{\frac{\delta A}{\lambda}}^2) \quad (5)$$

where C is a function of the source illumination profile and d is the thickness of the screen and is approximately the correlation distance of the medium. ER linearly grows with the propagation distance. This relationship is analogous to the average sidelobe floor in the radiation pattern of an array with errors [23] and to the average sidelobe floor in an arbitrary source distribution imaged through a distorting medium [18]. Eq. (5) can be applied to wideband as an approximation.

So long as certain correlation properties exist in the wavefront, phase compensation algorithms are still useful in strong scattering to partially remove phase distortion and build up the strength of the coherent field (Fig.4(b)). Wavefront amplitude distortion remains, as does residual phase distortion, and produces a significantly high incoherent background level in the spectrum. Any phase-deaberration procedure that provides a better phase error estimate than that of the basic algorithms [5-7] can reduce this background level. Wavefront-deaberration algorithms that take amplitude distortion into account can further reduce this background level if the algorithms reduce wavefront amplitude variance.

Consider the distortion vector $\mathbf{f} = \frac{E}{E_o} = A_t \exp(j\phi_t)$. Fig.5 shows such a distortion vector \mathbf{f} for some instantaneous sample of the radiation field. The optimum compensation weight vector or transformation $w_{opt} = A_t^{-1} \exp(-j\phi_t)$ is the right-most one which carries the distortion component of the complex sample to the intersection of the x-axis and the unit circle, for then both amplitude and phase are exactly corrected. The left-most transformation $w = A_t \exp(-j\phi_t)$ is matched filtering (MF) which squares the amplitude and conjugates the phase. MF is theoretically optimum for maximizing SNR on a white, Gaussian channel. It is an optimum solution for detection but not when fidelity is an important criterion, as in imaging. But it does satisfy the requirement for phase correction. Examples of MF algorithms are Dominant Scatterer Algorithm (DSA) [24] and Time Reversal Mirror (TRM)[8]. We should expect that MF algorithms are useful when wavefront distortion resides principally in phase, with amplitude relatively unaffected. Otherwise MF algorithms would be less effective than if amplitude were ignored and phase only were corrected. Later we show that by squaring the amplitude, a MF algorithm increases the wavefront amplitude variance and thereby increases the energy in the sidelobe region.

Consider what happens when a phantom consisting of a random phase screen is placed at a receiving transducer. The element signal samples are correct in amplitude and distorted only in phase by a random additive component. Phase aberration correction (PAC), consisting of phase conjugation (PC), is then the optimum compensator. The signal amplitude is unchanged. This operator is represented by the 2nd (from the left) transformation. Time delay compensation (TDC)[5-7] is in the same class.

The right-most transformation which corrects both amplitude and phase is the inverse filter (IF). It is theoretically ideal for fidelity but has drawbacks. Because the IF adjusts the channel gain to be the reciprocal of the signal strength, at points in the receiving aperture where signal strength is weak the enhanced channel gain raises the noise to the point where SNR can be impaired. This is particularly troublesome when there is coherent refractive interference in the receiving array. A second potential problem, which we have avoided by not working too close to the IF point, is that an IF is unstable when the distorting medium has zeroes in the complex plane. Thus the right-most transformation carries the correction too far.

The complex weights of MF, PC and IF are, respectively, A_t , 1 and A_t^{-1} , each multiplied by $\exp(-j\phi_t)$. The signal after weighting is A_t^2 , A_t and 1. The first and last are far from optimum for the reasons given. The 3rd from the left transformation is a compromise. The correction vector is $A_t^{-1/2} \exp(-j\phi_t)$. The signal after weighting is $A_t^{1/2}$ (called later the square rooter). Another transformation to the right of the square rooter is fourth rooter (signal amplitude is $A_t^{1/4}$ after weighting). In general, the correction vector is $A_t^{-(M-1)/M} \exp(-j\phi_t)$ and signal amplitude is $A_t^{1/M}$ after transformation of the Mth rooter. In part C, we demonstrate experimentally that low order rooters (square rooter and fourth rooter), in addition to phase deaberration at the aperture, can significantly improve contrast resolution without encountering the stability problem.

The dominant scatterer algorithm (DSA) developed in narrowband radar [24] is designed for adaptively focusing a large distorted receiving array upon a point target and is a matched filter process in space. DSA creates a compensating weight vector w from the complex conjugate of the received echo, i.e., $w = A_t \exp(-j\phi_t)$. The DSA-corrected receiving beam is the Fourier transform of $w A_t \exp(j\phi_t) = A_t^2$. Consequently, DSA uses wavefront amplitude to provide additional SNR gain than phase conjugation only, for which $w = \exp(-j\phi_t)$. However, when the wavefront amplitude is distorted, the amplitude weight further increases the sidelobe level in the beam. The measure in the increase is the increased wavefront amplitude variance. Since $A_t^2 = A_1^2 A_2^2 \dots A_t^2 \dots A_N^2$, therefore eq. (4) is changed to

$$A_t^2 = (\bar{A})^{2N} \prod_{i=1}^N \left(1 + \frac{\delta A_i}{\bar{A}}\right)^2 = (\bar{A})^{2N} \left(1 + \sum_{i=1}^N 2 \frac{\delta A_i}{\bar{A}} + \text{higher order products}\right) \quad (6)$$

The variance of square amplitude $\sigma_{A_t^2}^2 \approx 4N\sigma_{\frac{\delta A}{\bar{A}}}^2$ which is 4 times larger than without amplitude weight. Assuming phase error $\sigma_{\phi_t}^2$ is compensated, ER will rise from $C \frac{D}{d} \sigma_{\frac{\delta A}{\bar{A}}}^2$ to $C \frac{D}{d} 4\sigma_{\frac{\delta A}{\bar{A}}}^2$ which is about a 6 dB decrease in image contrast.

The time reversal mirror (TRM) developed by Fink [8] provides optimal focusing of a wideband transducer upon a target through a scattering medium and is a matched filter

process in both space and time (waveform). The operation reverses the received waveforms, retransmits them through the medium and then focuses the array on the target. The transmitting beam pattern is the convolution of the received waveforms and their time-reversed version. In the frequency domain, TRM is a phase conjugation procedure (with amplitude weight) at each frequency within the signal band. It is anticipated that TRM focusing produces poorer illumination in the neighborhood of the target than phase conjugation focusing does for the reason discussed in the previous paragraph.

Square root amplitude weighting changes eq. (4) to

$$A_i^{1/2} = (\bar{A})^{N/2} \prod_{i=1}^N \left(1 + \frac{\delta A_i}{\bar{A}}\right)^{1/2} = (\bar{A})^{N/2} \left(1 + \sum_{i=1}^N \frac{\delta A_i}{2\bar{A}} + \text{higher order products}\right) \quad (7)$$

The amplitude variance $\sigma_{A_i^{1/2}}^2 \approx \frac{N\sigma_{\delta A}^2}{4}$ which is 4 times less than with unit amplitude weight.

Assuming phase error is compensated. ER will reduce from $C \frac{D}{d} \sigma_{\delta A}^2$ to $C \frac{D}{4d} \sigma_{\delta A}^2$ which

implies about a 6 dB increase in image contrast. Mth rooter will reduce the amplitude variance by 2M if the SNR is still adequate. This nonlinear transformation upon wavefront amplitude is a compression operation (see Fig.6). The detailed evaluation of the effects of this compression operation upon image can be performed by studying the amplitude distributions of images before and after the operation. This is a subject of a later study.

Backpropagating the received wavefront to an optimal backpropagation distance and performing phase deaberration at this optimal distance (BPT) [5] provides first order correction of wavefront amplitude distortion due to propagation from the backpropagation distance to the receiving aperture and therefore performs better than phase deaberration at the aperture. In part C, we demonstrate experimentally that the BPT transformation is somewhere to the right of TDC and PC and left of PC and rooter. We also demonstrate that square rooter in addition to BPT can significantly improve the performance of BPT.

The relevant measurement in a strong scattering region is wavefront amplitude variance [15] (narrowband) or wavefront energy fluctuation [16],[21] (wideband) in addition to arrival time variance. Since wideband waveforms can be Fourier decomposed into a set of narrowband complex wavefronts within a signal band, waveform distortion therefore implies complex wavefront amplitude distortion and vice versa. In the following text, waveform distortion and wavefront amplitude distortion are used indistinguishably.

C. Correction upon Scattering Samples

To develop an understanding of deaberration, our studies have concentrated on one-way propagation measurements and corrections of point source fields. The 2-D measurement system and procedure were described in [16],[11]. Briefly, a breast specimen was placed between hemispherical source and receiving array. The 2-D array consisted of a 92-mm 1-D linear array translated 46 mm perpendicular to its axis to form a synthetic 2-D array 92 mm x 46 mm. Element pitch in the receiving transducer was 0.72 mm and a reflecting mask reduced the receiving elevation to 1.44 mm. Frequency was 3.7 MHz. Bandwidth was 2 MHz. Waveforms were measured at each element, from which 2-D wavefronts were reconstructed as functions of time. 3-D image data were calculated by (1) Fourier decomposition of the temporal waveforms at each (x,y) position in the aperture,

(2) calculation of a complex CW 2-D image at each Fourier frequency in the focal plane by using the angular spectrum technique [18], and (3) summation of the 2-D images to form the 3-D transient image. The final 2-D image used in this report was obtained by detecting the peak pressure value at each (x,f,yf) position in the image plane within the transient period. Contour maps of 2-D point source images at different thresholds were used to quantitatively evaluate image quality. The implementations of different correction methods and correction results were reported in [11]. The total measurements made were 16 with breast sample thickness varied from 1 to 4 cm. The following is a typical example of correction upon a scattering sample.

Figs.7 (a) and (b) show -6 dB contour plots of images obtained from the water path and the 3.5-cm breast tissue path (brs005). Contour spacing is 1 dB. Abscissa and ordinate are azimuth and elevation in mm in the image plane. Fig.7(a) shows the system diffraction pattern at -6 dB. The azimuthal beamwidth is about 1.5 mm (at a distance of 180 mm) meaning that the point (or lateral) resolution is 1.5/180 or 8.3 mrad. Because the size of the receiving array in elevation is half the size in the array direction, the width of the image in elevation is twice as large as in azimuth. When tissue is present (b), the image lobe is broadened. In (b) the beamwidth has grown from 1.5 mm to 3 mm in azimuth and 3.1 mm to 9.3 mm in elevation and the point resolution has worsened approximately 2:1 in azimuth and 3:1 in elevation. A symmetrical scattering pattern appears when the threshold is reduced. Fig.7 (c) shows a -20 dB contour plot of the sample image brs005. Contour spacing is 2 dB. Energy is spread out over a large area. No distinct structure or multipath lobe can be identified from the image.

Fig.8 (a)-(g) shows the correction result of the sample image brs005 by using different methods. Part (h) is the -30 dB level contour of a water path image. The contour spacings in Fig.8 are the outer contour levels divided by 10. Fig. 8 (a)-(c) shows TDC at -6, -20 and -30 dB levels (see Fig.7(b) and (c) for comparison). Image quality improved significantly and the system diffraction pattern is restored up to -20 dB level. The symmetrical scattering pattern outlined by outer contours at the -30 dB level is caused by residual phase errors after phase deaberration and incoherent amplitude distortion. Fig.8 (d) is the correction result of PC at the -30 dB level. Because of the complete removal of phase errors except for a 2π jump, the scattering pattern is further improved as compared to (c). Fig. 8 (e) is the result of BPT, and the scattering pattern is much better than that of PC at the aperture. The optimum backpropagation distance of this tissue sample is 30 mm. It is interesting to note that the beamwidth is narrower than that obtained through other methods. The reason is that the actual aperture is moved 30 mm closer to the source and the beamwidth is $(R\text{-optimal backpropagation distance}) \frac{\lambda}{L}$ instead of $R \frac{\lambda}{L}$, where R is the distance between source and the receiving aperture, and L is the aperture size. Fig.8 (f) is the correction result of PC and square rooter on wavefront amplitude at -30 dB. The pattern is very close to the system diffraction pattern (see (h) for comparison). Fig.8(g) is the result of wideband DSA at the -30 dB level. The correction result is worse than those of other methods.

Correction statistics of a simple metric, the lowest level at which mainlobe diffraction shape is maintained when different methods are used, are given in [11]. The average levels of using wideband DSA, PC and PC and rooter are 14.8 (std. 2.34), 19.5 (2.61) and 25.4 dB (2.55 dB), respectively. These results closely agree with the analysis in Section II of 6 dB decrease and increase in image contrast from squaring the amplitude (DSA) to amplitude intact (PC) and amplitude intact to square root of the amplitude (PC and rooter). The average levels of using TDC and BPT are 19.3 (2.43) and 24.0 dB(1.99 dB).

III. SCATTERING AND REFRACTION MODEL

A. Strong Scattering and Refraction Model

In a refractive medium coherent rays can be bent and split after they pass through tissue beds with different sound speeds [10]. The interference of refracted coherent ray bundles with incident rays produces image artifacts which appear as false targets. A simple representation of such a field is

$$E(x) = E_0 E_1 E_2 \dots E_i \dots E_N + E_{r1}(x) e^{j f_1(x)} + E_{r2}(x) e^{j f_2(x)} \quad (8)$$

where $f_1(x)$ and $f_2(x)$ define directions of secondary fields caused by refraction (see Fig.9).

The angular source intensity distribution is the superposition of the intensity image lobe, coherent interference lobes and incoherent spectrum (Fig.10(a)). The strengths and the numbers of interference lobes depend on orientations, curvatures, sizes and numbers of refractive bodies in the insonified medium, and may not be directly related to propagation depth. Although the chance of incident rays passing through more refractive bodies increases with the propagation depth, the strengths of interference lobes resulting from multiple refraction may not be significant compared with those resulting from single refraction. One quantitative measure of coherent interference phenomenon is the ratio of a large interference lobe or artifact to image lobe. For nine samples that were determined to have significant levels of coherent interference, the ratio varied randomly from sample to sample and showed no increase with thickness. The average strength (peak value) is 10 dB (std. 4 dB) [11]. Another quantitative measure is the total number of large refractive lobes in each image. The average is 2 and standard deviation is 0.53. The lobe number is independent of propagation depth. The refractive lobes are tightly clustered around the main lobe with an average radius of 5.6 mm (std. 1.8 mm) which is about 2 degrees. This is because the speed variations across glandular tissue and fat boundaries are small (5-10%).

The correction mechanism in a strong scattering and refraction medium is interesting. If the primary field is stronger than secondary refraction fields, the scattered energy removed by the deaberration process strengthens the primary field by folding the removed scattered energy into the primary field. As a result the ratio of image lobe to interference lobe is improved (Fig.10(b)). If, however, the primary field is weaker than the refracted field, the scattered energy removed by the deaberration process may strengthen the refracted field. The corrected result could then be worse than without correction. However, we have seen no evidence of this so far in our experiments reported in [11].

TRM or wideband DSA on reception is a matched filter process in both space and time, resulting in maximization of the signal relative to the background white noise. Correlation-based time-delay compensation algorithms, on the other hand, perform a different function; they adjust time-delay to maximize image sharpness or image contrast. In a refractive medium, the problem is more complicated. Neither TRM or wideband DSA nor time-delay algorithms have a way of knowing which signal is real and which is an artifact caused by coherent multipath. Because TRM or wideband DSA is a spatial matched filter its weight vector forms a lobular radiation pattern that matches the sum of both the real and false signals. Hence all targets, whether real or false, are enhanced. In our experiments reported in [11], with nine samples that have well-defined multipath artifacts, we found an

average 5 dB (std.2.5 dB) increase in peak artifact to image lobe ratio by using wideband DSA rather than by using time-delay compensation.

BPT backpropagates waveforms to the optimum distance before applying time-delay compensation. It removes wavefront amplitude distortion caused by propagation and reduces residual phase distortion by improving the performance of time-delay correction, but will not remove large lobes caused by refraction. A simple thought experiment is convincing: Backpropagating two plane waves produces two plane waves at whatever distance the waves are backpropagated.

Thus it is important to understand the deaberration operations and to design appropriate algorithms that offer optimal performance in the corresponding distorting medium. Aperture measurement alone can not distinguish between wavefront distortions caused by refraction or by strong scattering. Distinction can be made in the image domain where refraction appears as large, coherent interference lobes while strong scattering spreads into an incoherent background. While the refracted energy may or may not be significantly larger than the energy in the incident wave, it nevertheless produces image artifacts which will destroy the quality of a high resolution image.

B. Correction upon Samples with Well-defined Multipath

In most breast samples (9 out of 16), scattering and coherent interference are both present. Fig.11 (a) and (b) are -10 dB contour plots of images obtained from the water path and the 4-cm breast tissue path (brs006). Contour spacing is 2 dB. In tissue image (b), three lobes instead of one central image lobe appear. Inner contours of the image lobe are close to the system diffraction pattern (Fig.11(a)) while the outer contours are highly irregular due to scattering. The point resolution is worsened by approximately 2:1 in azimuth and 3:1 in elevation. Two refractive lobes appear at (-4, -2.5) and (3.5, 1.5), and their strengths are -6 and -8 dB. A closer examination is obtained from 45 degree cuts (Fig.12) of the Fig.11 (a) and (b) images. In Fig.12 (a), the peak sidelobe is -36 dB, which is the best we can obtain from the measurement system. In the tissue image, two large sidelobes (-6 dB and -8 dB) appear on either side of the mainlobe. The two nulls between the lobes are deep (left : -13 dB below peak, right: -15 dB), which is a typical coherent interference phenomenon [15].

A symmetrical scattering pattern generally appears when the threshold is reduced, as shown Fig.11(c) with a -16 dB threshold contour and contour spacings of approximately 1.5 dB. The outer contours show a roughly symmetrical pattern typical of scattering while the inner contours show an asymmetric lobular interference pattern.

Fig.13 shows correction results of the sample image brs006 after applying different methods. The contour spacings are the outer contour levels divided by 10. Fig.13(a) is the -16 dB contour map of applying TDC (see Fig.11(c) for comparison)). Image quality improved significantly because of the minimization of the phasefront distortion caused by scattering. The area within the -16 dB inner contour is reduced by a factor of 11. The mainlobe pattern is close to the system diffraction pattern although the area is still 1.6 times larger than the area in water at the same level. Two large lobes remain as expected and appear as two additional sources. Fig.13(h) is the correction result at a -16 dB level of applying wideband DSA. It is evident that the procedure enhances interference in this example; the artifacts are 5 dB higher than in Fig.13(a). Figs.13(b) and (c) show -25 and -30 dB contour plots of TDC. In Fig.13(b) the outer contours show an asymmetric interference pattern with scattered energy distributed around the two interference lobes. In Fig.13(c) the outer contours show the more symmetrical scattering pattern caused by incoherent wavefront amplitude distortion and residual phase distortion. Fig.13(d) is the result of PC at -30 dB. The approximately symmetrical scattering pattern outlined by outer

contours in (c) is improved due to better phase deaberration. The energy is more concentrated around the image lobe and interference lobes. Part (e) is the result of BPT, and the scattering pattern is further improved as compared with the result of PC at the aperture. The backpropagation distance of this sample is 50 mm. Part (f) is the result of PC and square rooter at -30 dB. The pattern is very close to the system diffraction pattern. PC and fourth rooter shown in Fig.13(g) restores the diffraction-limited image to a -30 dB level.

It is interesting to note that the strengths of the two interference lobes are also reduced by 8 dB after TDC and PC. They are further reduced by 5, 7 and 15 dB after BPT, PC and square rooter, and PC and fourth rooter, respectively. The improvement comes from the scattered energy which is originally distributed around the mainlobe and each of the refracted multipath lobes. This energy is coherently added back, by the deaberration process, to the dominant lobe, which in this case is the mainlobe. The overall result is an improvement of the image lobe to the interference lobe ratio.

Determination of whether interference was coherent or scattered was based upon whether or not large lobes could be removed by applying phase-deaberration algorithms. Another indicator is whether or not a lobe location moves (scattering) or remains relatively the same (refraction) after the phase deaberration process. Both means were used to identify whether these lobes were produced by refraction or scattering. Large lobes in nine samples are believed to be caused by the interference process. In these samples, we have found an average of a 10 dB (std. 4dB) improvement in the range of 5-16 dB after TDC, due to the coherent strengthening of the mainlobe.

IV. EXPERIMENTS

The significance of appropriate amplitude weighting discussed in Section II is experimentally evaluated using ER introduced in eq. (5). When phase error is removed, ER is proportional to $\sigma_{A_t}^2$. The detailed measurement procedures of ER and $\sigma_{A_t}^2$ are reported in [11]. Fig.14 shows regression plots of ER, measured after reducing the phase error using PC, wideband DSA, and PC and square rooter, vs. $\sigma_{A_t}^2$. The three methods compensate phase errors. ER and $\sigma_{A_t}^2$ measured in water using the three correction procedures are also incorporated into the three data sets to represent the system performance. The linear relationships are statistically significant. The average ERs are 103% (std. 33.9%), 25% (6.9%) and 6.8% (1.6%) when wideband DSA, PC and PC and rooter are used, respectively. An approximate factor of 4 reduction in ER from amplitude squaring (wideband DSA) to amplitude intact (PC) and amplitude intact to square root of amplitude (PC and rooter) is obtained. The results agree with the analysis in Section II and indicate that intelligent use of amplitude weighting is crucial for improving image contrast.

Scattered energy increases with the propagation depth as predicted by eq. (5) and performances of descattering algorithms deteriorate with propagation depth. In Ref.11, regression plots of ER vs. approximate thickness of 16 breast samples were given by using 7 descattering procedures. The regression plot without correction was also given. The linear relationships were statistically significant. Fig.15 shows partial results taken from Ref.11. The five curves in the figure are obtained by using wideband DSA (circle), TDC (solid square), PC (triangle), PC and rooter (solid triangle) and no correction (solid circle). ER reduction from amplitude weighting (wideband DSA) to square root of amplitude weighting (PC and rooter) is clearly shown by the regression plots. The regression lines are extrapolated to 100 mm propagation depth, which is considered the average maximum penetration depth required for breast.

Before we discuss the predicted performance of the descattering algorithms at 100 mm depth, we need to find the relationship between ER and image contrast, which is defined as the lowest level of the mainlobe diffraction shape. Image contrast increases monotonically with ER. Table I lists the measured average ER (first row) and the measured average image contrast (second row) when different correction methods as well as no correction are used [11]. The relationship between ER and image contrast can be predicted by using ER and image contrast obtained from PC (or any correction method) as base line (bold numbers in Table I). For example, the measured image contrast with PC is 19.5 dB. The ER ratio of PC alone to PC and rooter is $2.5 / 6.8 = 3.7$, corresponding to increase of 5.7 dB. Thus the predicted image contrast is $19.5 \text{ dB} + 5.7 \text{ dB} = 25.2 \text{ dB}$ which closely agrees with the measured value 25.4 dB. The third row of Table I lists the predicted image contrast based on the measured ER. The predicted values are in reasonably good agreement with the measured values except for the pair without correction. The reason is due to ER measurement error in images without correction. For some severely distorted images, it is often difficult to identify the mainlobe region.

At 100 mm depth ER after PC reaches 85% which corresponds to 14.0 dB image contrast. Therefore, PC, the best linear phase correction procedure at the aperture, is likely to result in only ~14 dB image contrast at this depth. ER after wideband DSA reaches 324.3% which corresponds to only ~8.4 dB image contrast. ER after PC and rooter reaches 22% , which provides ~20.1 dB image contrast. ER after TDC reaches 148% , which offers only ~11.8 dB image contrast.

The data used to test the analysis developed in Section II are sparse; nevertheless they do provide information for designers of next generation high quality breast scanners.

V. DISCUSSION

A. Application to Diffuse Scattering Medium

The compression operation upon wavefront amplitude, in addition to phase deaberration or BPT, introduced in the paper is applicable to a diffuse scattering medium. Experiments with TDC and rooter and TDC alone show that ER can be reduced from 44.2% to 28.6%, the ratio of which indicates 1.3 dB improvement in image contrast. However, experiments with PC and rooter and PC alone show that ER can be reduced from 25.1% to 6.8%, which is about 6 dB improvement in image contrast. The large difference is due to the fact that PC corrects phase in every signal spectrum while TDC makes single correction which applies to all frequencies. The consequence is that TDC leaves significant phase residual. Therefore, to successfully improve image contrast, good phase deaberration is the first crucial step to reduce ER, and followed by amplitude compression such as rooter.

B. Application to Coherent Interference upon Pulse-echo Imaging

High resolution, high dynamic range breast imaging implies seeing a black cyst 60 dB weaker than a bright speckled target. In this paper, we show that 30 dB image contrast on reception is obtainable by taking low order rooters provided that phase error is completely compensated. In pulse echo, refracted energy from the targets insonified by the subbeam will arrive at angles of $1 - 3^\circ$ from the target direction [11] and therefore in the sidelobe region of array. The sidelobe level of the receiving beam will be ~ -30 dB. The average level of refracted multipath is found to be -10 dB relative to the target image [11] and therefore the average multipath signal level entering the system is $\sim (10+30) \text{ dB} = -40 \text{ dB}$ below the echo strength of the illuminated target. Cancellation algorithms [16-17] must

suppress these multipath signals to achieve 60 dB contrast resolution. Hence about 20 dB further cancellation is required.

VI. CONCLUSIONS

We conclude, through analysis and experiment, that 1) matched filtering compensation algorithms while optimal for detection are not suitable for imaging in distributed scattering, because the algorithms increase wavefront amplitude variance and therefore decrease image contrast; and 2) low order rooters upon wavefront amplitude, akin to inverse filtering, in addition to phase deaberration can significantly improve image contrast without encounter stability problem. Further study is needed to optimize the required degree of compression as a function of SNR and image contrast.

Incoherent scattering and coherent multipath affect an image differently. Scattering reduces target strength, broadens the image lobe and increases background level while refraction creates coherent multipath interference which produces false targets or image artifacts. Adaptive compensation algorithms developed so far are useful to partially remove the scattered energy and coherently add it back to the coherent image. The result is the improvement of both lateral and contrast resolution to a large extent. The ratio of image lobe to artifacts is also improved because of the strengthening of the coherent field by descattering processes.

ACKNOWLEDGMENTS

The *in vitro* measurements were done with the collaboration of Ms. Laura M. Hinkelman and Prof. Robert C. Waag, Departments of Electrical Engineering and Radiology, University of Rochester, Rochester, who also give valuable comments on the paper. Invaluable consultation was provided by Dr. Kai Thomenius, Director of Research, Interspec, Inc., Ambler, PA., a division of ATL, in the course of this study. Funding was provided by the Army (DAMD 17-93-J-3014 and DAMD 17-94-J-4133) and NSF (BCS92-09680).

APPENDIX

Let $s(u)$ represent the complex angular source distribution, where $u = \sin(\theta)$ and θ is the angle from the array normal. Its complex radiation field in the axis of the receiving array in a homogeneous medium is the inverse Fresnel transform of $s(u)$ or inverse Fourier transform of $s(u)$ after correcting for near-field curvature and is denoted as $E_o(x)$. In an inhomogeneous medium, the radiation field is $i(x) = \alpha W(x) E_o(x) M(x)$ where $w(x)$ is the aperture weighting function, $M(x) = A_t \exp(j\phi_t)$ is the medium induced distortion and α is a constant to reflect any signal loss. The complex image is

$$\hat{s}_i(u) = \alpha F[W(x) E_o(x) M(x)] = \alpha f(u) * s(u) * F(M(x)) \quad (1)$$

where $F(M(x)) = \mu(u)$ is the angular impulse response of the medium. F denotes Fourier transform. The subscript i denotes inhomogeneous medium. For $\alpha = 1$ and $M(x) = 1$, the complex image corresponds to the image in homogeneous medium and is denoted as $\hat{s}_h(u)$.

The derivation is made with discrete rather than continuous variables. Thus x is replaced by $n=1, 2, \dots, N$, where N = number of elements in the array. The following assumptions are made:

1. Medium induced amplitude and phase errors are uncorrelated.
2. The phase errors of $\phi_t(n)$, $n=1, 2, \dots, N$, are statistically uncorrelated random variables with a common probability density function (pdf).
3. The amplitude errors of $A_t(n)$, $n=1, 2, \dots, N$, are statistically uncorrelated random variables with a common pdf.

The complex image $\hat{s}_i(u)$ can be written as

$$\hat{s}_i = \alpha F[E_o(n)A_t(n)] = \alpha \sum_{n=1}^N E_o(n)A_t(n) \exp(jkndu) \quad (2)$$

where the aperture taper $W(n)$ has been chosen as unity.

The image intensity is the product of (2) and its complex conjugate:

$$\begin{aligned} \hat{s}_i(u) \hat{s}_i^*(u) &= \alpha^2 \sum_{n=1}^N \sum_{m=1}^N E_o(n)E_o^*(m)A_t(n)A_t(m) \exp(j(\phi_t(n) - \phi_t(m))) \exp(jk(n-m)du) \\ &= \alpha^2 \left\{ \sum_{n=m}^N E_o(n)E_o^*(n)A_t^2(n) + \right. \\ &\quad \left. \sum_{n \neq m}^N E_o(n)E_o^*(m)A_t(n)A_t(m) \exp(j(\phi_t(n) - \phi_t(m))) \exp(jk(n-m)du) \right\} \end{aligned} \quad (3)$$

The average intensity is

$$\begin{aligned} \overline{\hat{s}_i(u) \hat{s}_i^*(u)} &= \alpha^2 \left\{ \sum_{n=m}^N E_o(n)E_o^*(n) \overline{A_t^2(n)} + \right. \\ &\quad \left. \sum_{n \neq m}^N E_o(n)E_o^*(m) \overline{A_t(n)A_t(m)} \exp(j(\phi_t(n) - \phi_t(m))) \exp(jk(n-m)du) \right\} \\ &= \alpha^2 \left\{ \sum_{n=m}^N E_o(n)E_o^*(n)(\sigma_{A_t}^2 + (\overline{A_t})^2) + \sum_{n \neq m}^N E_o(n)E_o^*(m)(\overline{A_t})^2 \overline{\exp(j(\phi_t(n) - \phi_t(m)))} \exp(jk(n-m)du) \right\} \end{aligned} \quad (4)$$

where $\overline{A_t(n)A_t(m)} = \overline{A_t(n)}\overline{A_t(m)} = \overline{A_t}^2$ and

$\overline{\exp(j\phi_t(n))\exp(-j\phi_t(m))} = \overline{\exp(j\phi_t(n))}\overline{\exp(-j\phi_t(m))} = \overline{\exp(j\phi_t)}^2$ because of the assumptions 2 and 3, respectively.

$$\begin{aligned} \overline{\hat{s}_i(u) \hat{s}_i^*(u)} &= \alpha^2 \left\{ \sum_{n=m}^N E_o(n)E_o^*(n)(\sigma_{A_t}^2) + \sum_{n=m}^N E_o(n)E_o^*(n)(1 - \overline{\exp(j\phi_t)}^2)(\overline{A_t})^2 \right. \\ &\quad \left. + \overline{A_t}^2 \overline{\exp(j\phi_t)}^2 \sum_{n=1}^N \sum_{m=1}^N E_o(n)E_o^*(m) \exp(jk(n-m)du) \right\} \end{aligned} \quad (5)$$

The term $\overline{A_t}^2 \overline{\exp(j\phi_t)}^2 \sum_{n=m}^N E_o(n)E_o^*(n)$ is added to the second term of (4) resulting in the third term of (5). The same term is subtracted from (4) resulting in the second term of (5).

$$\begin{aligned} \overline{\hat{s}_i(u) \hat{s}_i^*(u)} &= \alpha^2 \left\{ \sum_{n=m}^N E_o(n) E_o^*(n) (\sigma_{A_t}^2) + \sum_{n=m}^N E_o(n) E_o^*(n) (1 - \overline{\exp(j(\phi_t)^2)}) (\overline{A_t})^2 \right. \\ &\quad \left. + (\overline{A_t})^2 \overline{\exp(j(\phi_t)^2)}^2 \hat{s}_h(u) \hat{s}_h^*(u) \right\} \end{aligned} \quad (6)$$

Integration with respect to u on both side of eq. (6) yields

$$\begin{aligned} &\int_{\text{mainlobe}} \hat{s}_i(u) \hat{s}_i^*(u) du + \int_{\text{sidelobe}} \hat{s}_i(u) \hat{s}_i^*(u) du \\ &= \alpha^2 \left\{ \int_{\text{mainlobe}} \left[\sum_{n=m}^N E_o(n) E_o^*(n) (\sigma_{A_t}^2) + \sum_{n=m}^N E_o(n) E_o^*(n) (1 - \overline{\exp(j(\phi_t)^2)}) (\overline{A_t})^2 \right] du \right. \\ &\quad \left. + \int_{\text{mainlobe}} (\overline{A_t})^2 \overline{\exp(j(\phi_t)^2)}^2 \hat{s}_h(u) \hat{s}_h^*(u) du \right. \\ &\quad \left. + \alpha^2 \left\{ \int_{\text{sidelobe}} \left[\sum_{n=m}^N E_o(n) E_o^*(n) (\sigma_{A_t}^2) + \sum_{n=m}^N E_o(n) E_o^*(n) (1 - \overline{\exp(j(\phi_t)^2)}) (\overline{A_t})^2 \right] du \right. \right. \\ &\quad \left. \left. + \int_{\text{sidelobe}} (\overline{A_t})^2 \overline{\exp(j(\phi_t)^2)}^2 \hat{s}_h(u) \hat{s}_h^*(u) du \right\} \right\} \end{aligned} \quad (7)$$

$$\begin{aligned} \text{ER} &= \frac{\Delta \text{energy} - \text{outside} - \text{mainlobe}}{\text{energy} - \text{inside} - \text{mainlobe}} \\ &= \frac{\int_{\text{sidelobe}} \sum_{n=m}^N E_o(n) E_o^*(n) du \{ \sigma_{A_t}^2 + (1 - \overline{\exp(j(\phi_t)^2)}) \overline{A_t}^2 \}}{\int_{\text{mainlobe}} (\overline{A_t})^2 \overline{\exp(j(\phi_t)^2)}^2 \hat{s}_h(u) \hat{s}_h^*(u) du} \end{aligned} \quad (8)$$

where $\int_{\text{sidelobe}} (\overline{A_t})^2 \overline{\exp(j(\phi_t)^2)}^2 \hat{s}_h(u) \hat{s}_h^*(u) du$ is small compared with the rest of the sidelobe terms and is dropped from the numerator and

$\int_{\text{mainlobe}} \left[\sum_{n=m}^N E_o(n) E_o^*(n) (\sigma_{A_t}^2) + \sum_{n=m}^N E_o(n) E_o^*(n) (1 - \overline{\exp(j(\phi_t)^2)}) (\overline{A_t})^2 \right] du$ is small compared with another mainlobe term and is dropped from the denominator. Since $\overline{A_t}$ is close to unity and $\overline{\exp(j(\phi_t)^2)}$ is also close to unity when the phase error is moderate, therefore the right side of (8) is $C \{ \sigma_{A_t}^2 + (1 - \overline{\exp(j(\phi_t)^2)}) \}$, where

$$C = \frac{\int \sum_{n=m}^N E_o(n) E_o^*(n) du}{\int_{mainlobe} \hat{s}_h(u) \hat{s}_h^*(u) du}$$

which is related to the source properties only. When the

phase error is moderate, $1 - \overline{\exp(j(\phi_t))^2} \approx \sigma_{\phi_t}^2$ and $ER \approx C\{\sigma_{A_t}^2 + \sigma_{\phi_t}^2\}$.

REFERENCES

- [1] G. E. Trahey, P. D. Freiburger, L. F. Nock, and D. C. Sullivan "In Vivo Measurements of Ultrasonic Beam Distortion in the Breast," *Ultrason. Imag.* 13, 71-90 (1991).
- [2] M. Moshfeghi, and R.C. Waag, In Vivo and in Vitro Ultrasound Beam Distortion Measurements of a Large Aperture and a Conventional Aperture Focused Transducer, *Ultrasound Med. Biol.* 5, 415-428 (1988).
- [3] B.D.Steinberg, "Scattering from a Multiple Random Phase Screen Model of a Random Inhomogeneous Medium," submitted to J. Acoust. Soc. Am. (1995)
- [4] Q. Zhu and B. Steinberg, "Modelling, Measurements and Correction of Wavefront Distortion Produced by Breast Specimens", *Proc. IEEE Ultrasonic Symp.* 1613-1617(1994).
- [5] S. W. Flax and M. O'Donnell, "Phase Aberration Correction using Signals from Point Reflectors and Diffuse Scatterers: Basic Principles," *IEEE Trans. Ultrason., Ferroelec. and Freq. Contr.*, 35(6),758-767 (1988).
- [6] E. H. Attia and B. D. Steinberg, "Self-Cohering Large Antenna Arrays Using the Spatial Correlation Properties of Radar Clutter," *IEEE Trans. Antennas Prop.*, AP-37(1), 30-38 (1989).
- [7] L. Nock, G. E. Trahey, and S. W. Smith, "Phase Aberration Correction in Medical Ultrasound using Speckle Brightness as a Quality Factor," *J. Acoust. Soc. Am.* 85(5), (1989)
- [8] M. Fink, "Time reversal of ultrasonic fields – part I: basic principles," *IEEE Trans. Ultrason. Ferroelec. Freq. Contr.*, vol. 39, pp. 555-566, 1992.
- [9] D.-L. Liu and R. C. Waag, "Correction of Ultrasonic Wavefront Distortion Using Backpropagation and Reference Waveform Method for Time-shift Compensation," *J. Acoust. Soc. Am.* 96, 649-660 (1994).
- [10] Q. Zhu and B. D. Steinberg, "Large-Transducer Measurements of Wavefront Distortion in the Female Breast," *Ultrason. Imag.*, 14, 276-299 (1992).
- [11] Q. Zhu, B. D. Steinberg, "Deaberration of Incoherent Wavefront Distortion: An approach toward inverse filtering" submitted to *IEEE Trans. Ultrason. Ferroelec. Freq. Contr.*
- [12] Q. Zhu and B. Steinberg, "Coherent Cancellation of Refraction Artifacts," 20 Int. Symp. on Ultrasonic Imaging and Tissue Characterization (June 1995).
- [13] M. O'Donnell and S. W. Flax, "Phase Aberration Measurements in Medical Ultrasound: Human Studies," *Ultrasonic Imaging.* 10(1), 1-11 (1988).
- [14] D.-L. Liu and R. C. Waag, "Time-shift Compensation of Ultrasonic Pulse Focus Degradation Using Least-mean-square Error Estimates of Arrival Time, *J. Acoust. Soc. Am.* 95(1), 542-555 (1994).
- [15] Q. Zhu, Q., B. D. Steinberg and R. Arenson, "Wavefront amplitude distortion and image sidelobe levels – parts II, In vivo Experiments," *IEEE Trans. Ultrason. Ferroelec. Freq. Contr.* 40(6) 754-762 (1993).
- [16] L. M. Hinkelman, D-L. Liu, and R. C. Waag, Q. Zhu, and B.D. Steinberg, "Measurement and Correction of Ultrasonic Pulse Distortion Produced by the Human Breast", *J. Acoust. Soc. Am.* 97(3), 1958-1969 (1995).

- [17] D. Carpenter and G. Kossoff, "Correction of Distortion in US Images Caused by Subcutaneous Tissues: Results in Tissue Phantoms and Human Subjects," *Radiology* (195): 563-567, (1995).
- [18] Q. Zhu, Q. and B. D. Steinberg , "Wavefront amplitude distortion and image sidelobe levels – parts I, theory, " *IEEE Trans. Ultrason. Ferroelec. Freq. Contr.* 40(6) 747-753 (1993).
- [19] A. Ishimaru, *Wave Propagation and Scattering in Random Media*, Academic Press, New York (1978).
- [20] M. Born and E. Wolf, *Principles of Optics*, Pergamon Press (1980).
- [21] L. M. Hinkelman, D-L. Liu, L.A. Metlay, and R. C. Waag, "Measurements of Ultrasonic Pulse Arrival Time and Energy Level Variations Produced by Propagation through Abdominal Wall," *J. Acoust. Soc. Am.* 95, 530-541 (1994).
- [22] Y. Sumino and R.C. Waag, "Measurements of Ultrasonic Pulse Arrival Time Differences Produced by Abdominal Wall Specimens," *J. Acoust. Soc. Am.*, 90(6), 2924-2930 (1991).
- [23] B. D. Steinberg, *Principles of Aperture and Array System Design* (Hohn Wiley & Sons, New York, 1976).
- [24] B. D. Steinberg, "Radar Imaging from a Distorted Array: The Radio Camera Algorithm and Experiments," *IEEE Trans. Antennas Prop.* AP-29(5), 740-748 (1981).

Table I.

Table I Relation of ER and image contrast (predicted and measured)								
	w/o Corr.	TDC	PC	Wideband DSA	BPT	PC	BPT	PC
ER	214.7%	44.2%	25.1%	103.5%	12.8%	6.8%	3.7%	2.1%
Image Contrast								
measured	4.2 (dB)	19	19.5	14.8	24.0	25.4	29.4	31.1
predicted	10.2 (dB)	17	19.5	13.3	22.4	25.2	27.8	30.3

FIGURES

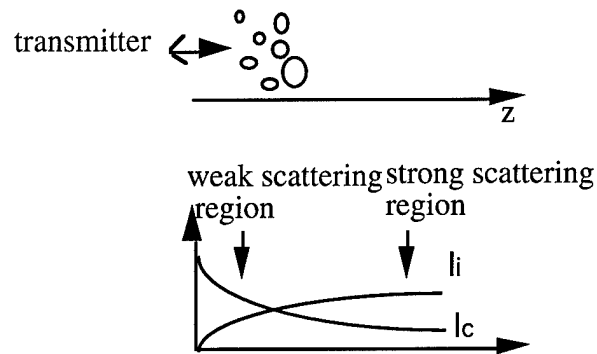
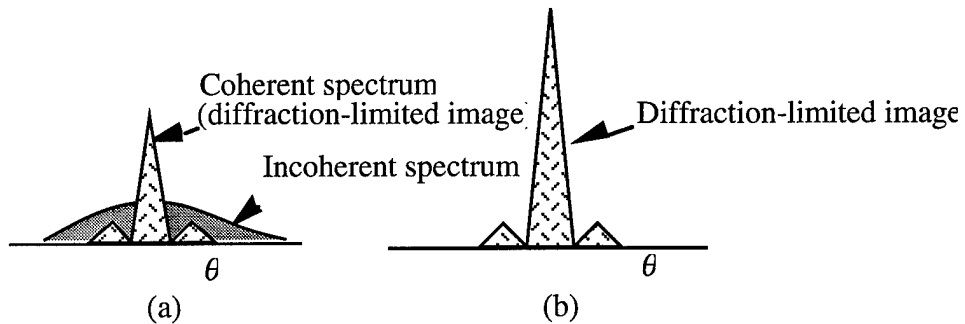
Figure 1. Approximate behavior of the coherent intensity I_c and the incoherent intensity I_i .

Fig.2. Angular source intensity distribution. Statistical model. (a) Before phase deaberration showing reduced coherent spectrum and of incoherent spectrum. (b) After phase deaberration.

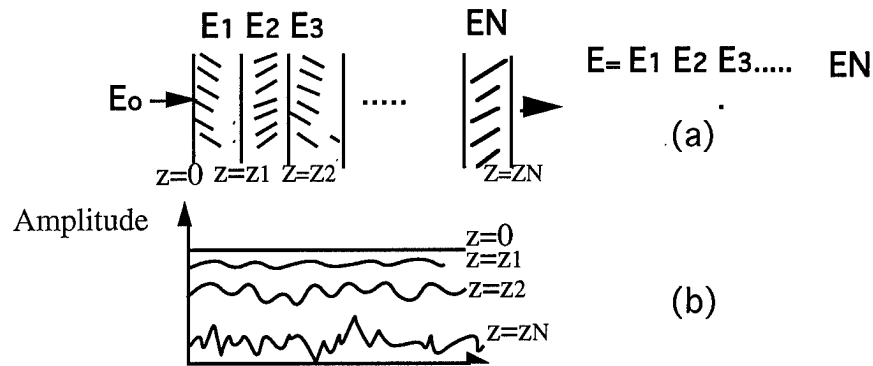


Fig.3 The field is the product of contributions from each layer. Wavefront amplitude fluctuation increases as wave propagates.

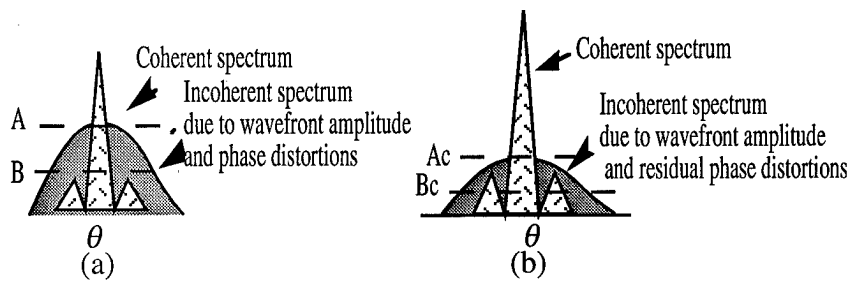


Fig.4. Statistical models of angular source intensity distribution. (a) Before phase correction. (b) After phase correction.

DEABERRATION TRANSFORMATIONS

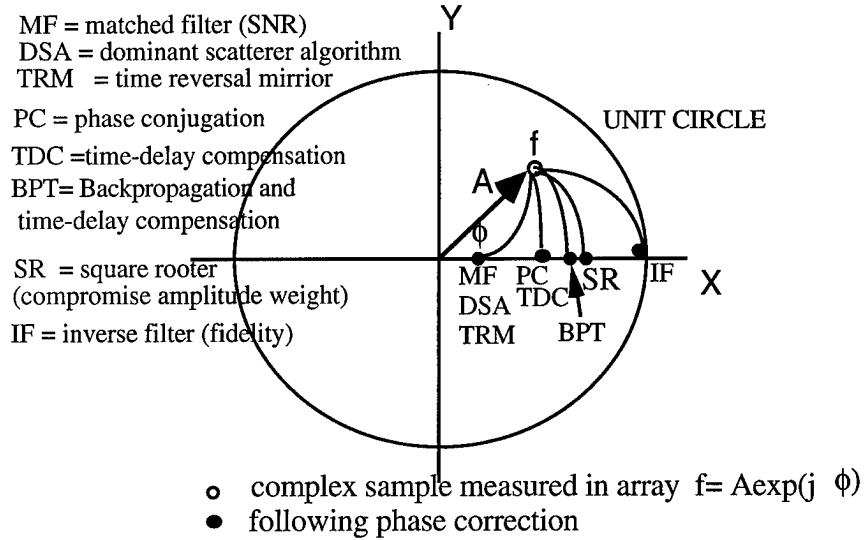


Fig.5. Deaberration transformations. f is distortion vector for instantaneous sample of the radiation field. Transformations to the real axis all correct phase. Left (MF) maximizes SNR but increases amplitude distortion. Right (IF) maximizes imaging fidelity but increases noise. SR is good compromise.

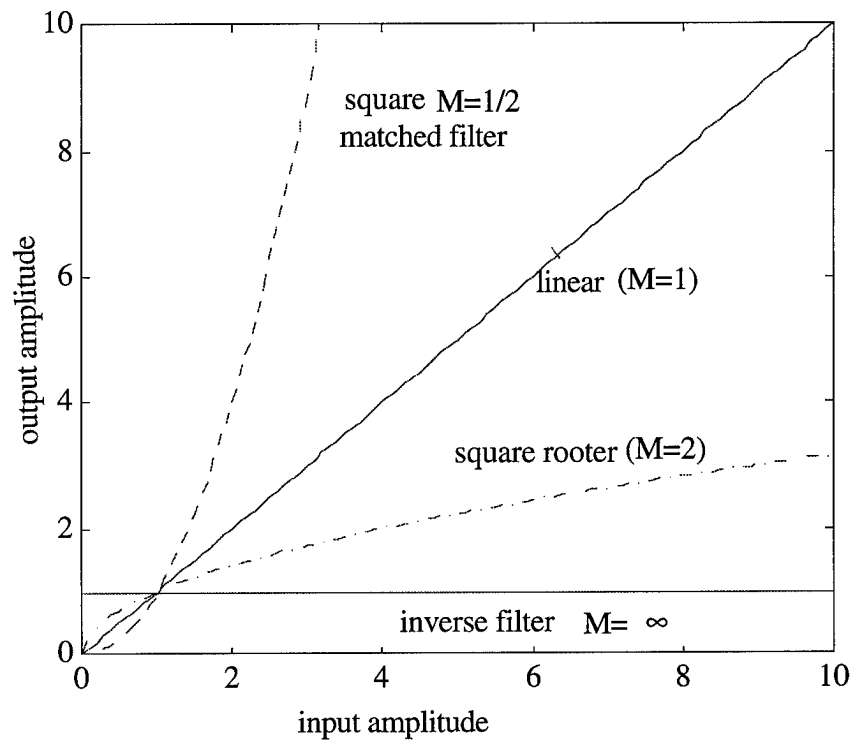
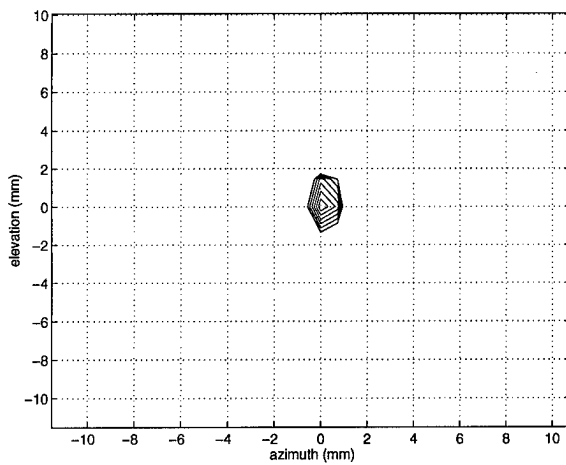
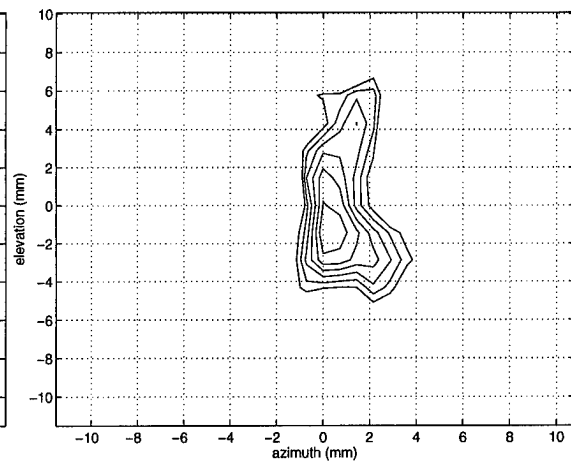


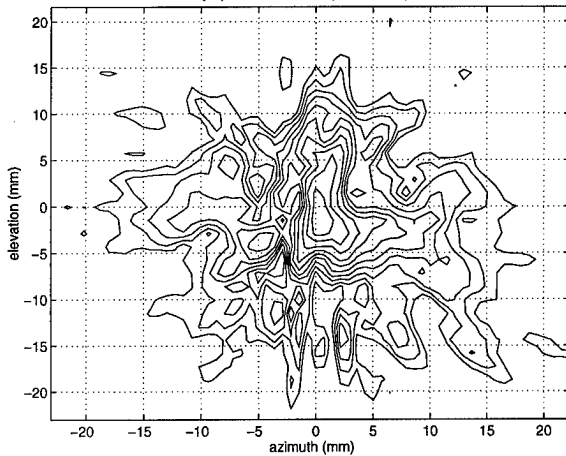
Fig.6. Plots of the input and output amplitude transforms.



(a) -6dB (water)



(b) -6 dB (brs005)



(c) -20 dB (brs005)

Fig.7. 2-D contour maps of point source images. (a) water data showing diffraction pattern of system. Outer contour is -6 dB level. (b) measured through the 3.5-cm tissue (brs005), showing asymmetric scattering effect. Outer contour is -6 dB level. (c) Image brs005 at -20 dB contour level. The outer contour shows symmetrical scattering pattern. No distinct structure or multipath is observed. Note the change of scale from (a) and (b).

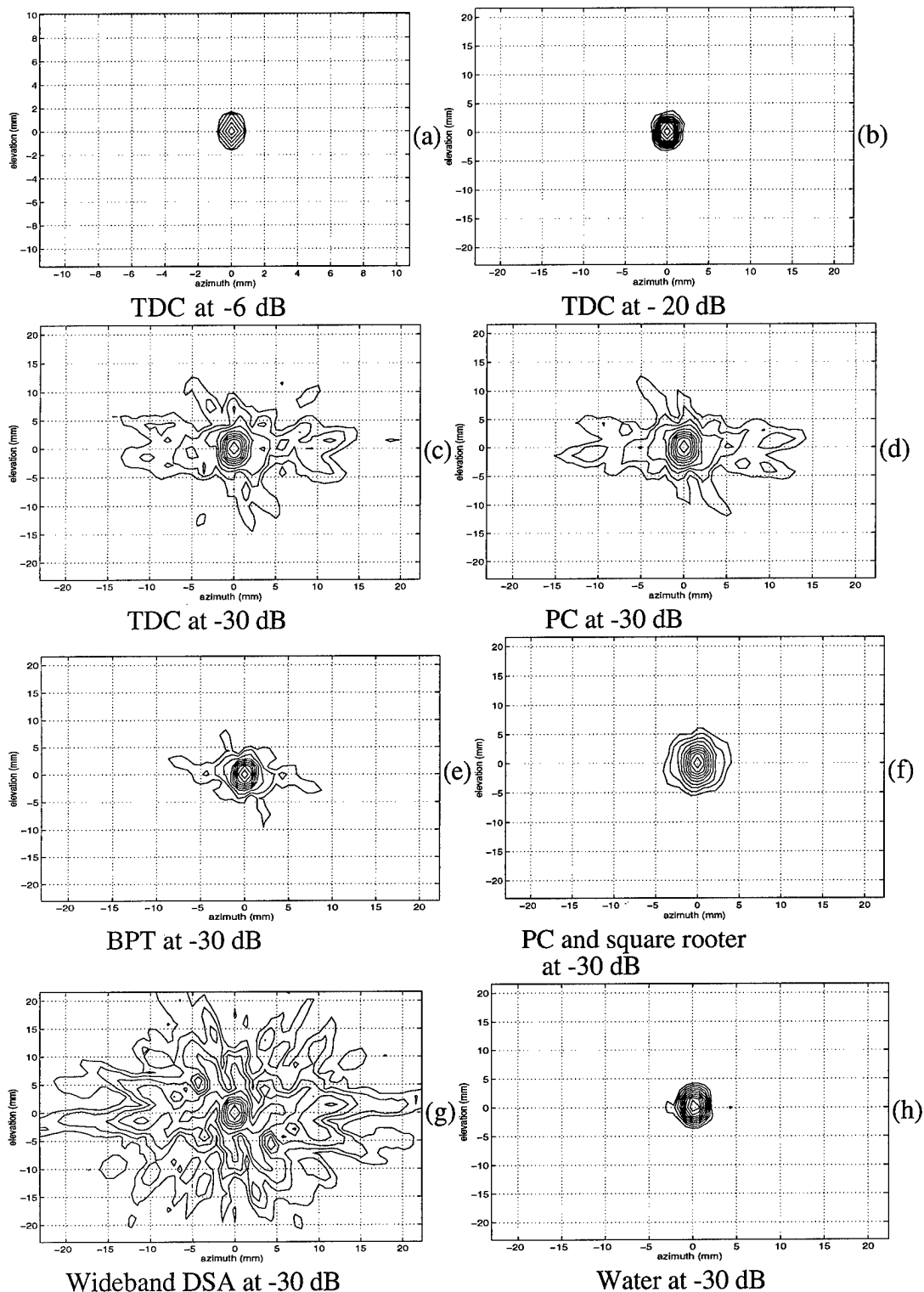


Fig.8. Distortion corrected contour maps of the sample image brs005 (see Fig.4(b) and (c) for comparison) (a) TDC at -6 dB. (b) TDC at -20 dB. (c) TDC at -30 dB. (d) PC at -30 dB. (e) BPT at -30 dB. (f) PC and square rooter at -30 dB. (g) Wideband DSA at -30 dB. (h) Water at -30 dB . Note the scale change of (b)-(h) from (a).

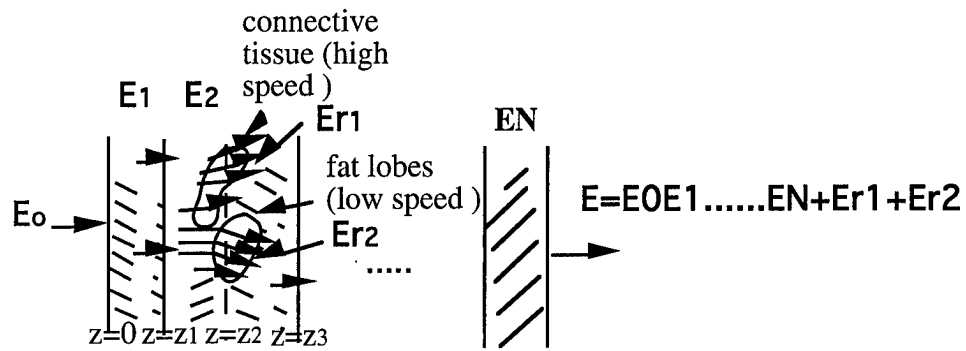


Fig.9 The field is the original field plus refracted fields.

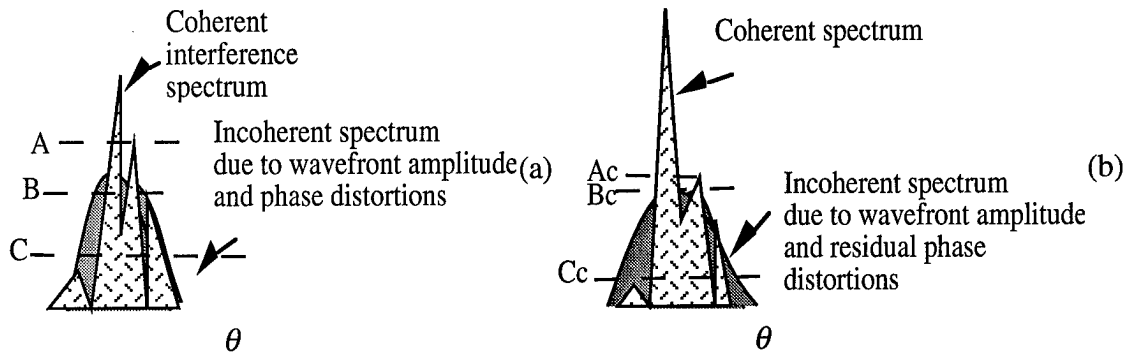


Fig.10. (a) Before phase compensation. (b) After.

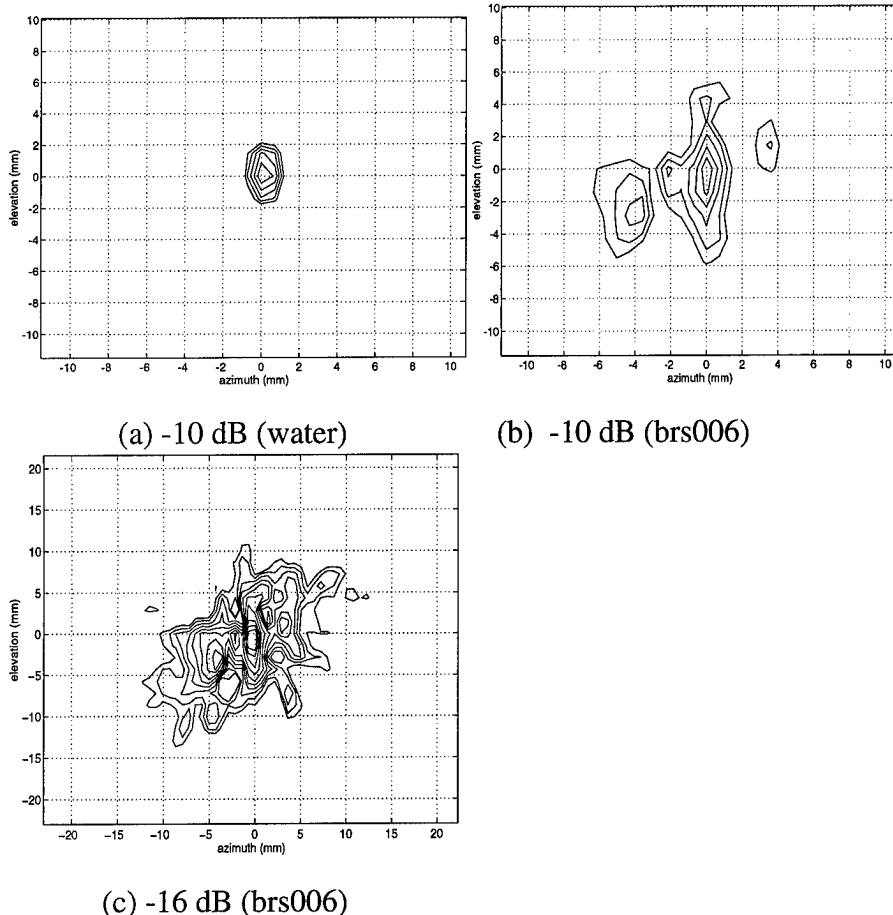


Fig.11. 2-D contour maps of point source images. (a) water data showing diffraction pattern of system. Outer contour is -10 dB level. (b) measured through the 4-cm tissue (brs006), showing highly asymmetric interference pattern. Outer contour is -10 dB level. (c) Image brs006 at -16 dB contour level. The outer contour shows more symmetrical scattering pattern. Note the change of scale from (a) and (b).

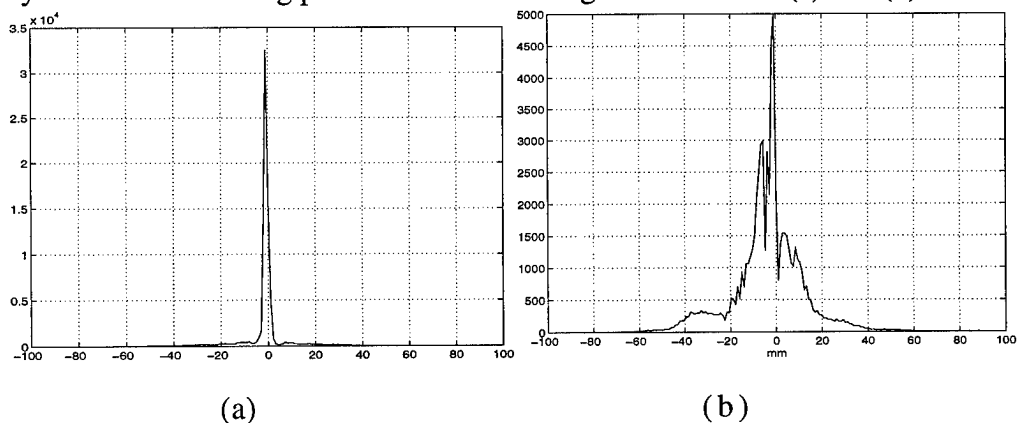


Fig. 12. (a) 45 degree cuts of 2-D images (a) water. (b) brs006.

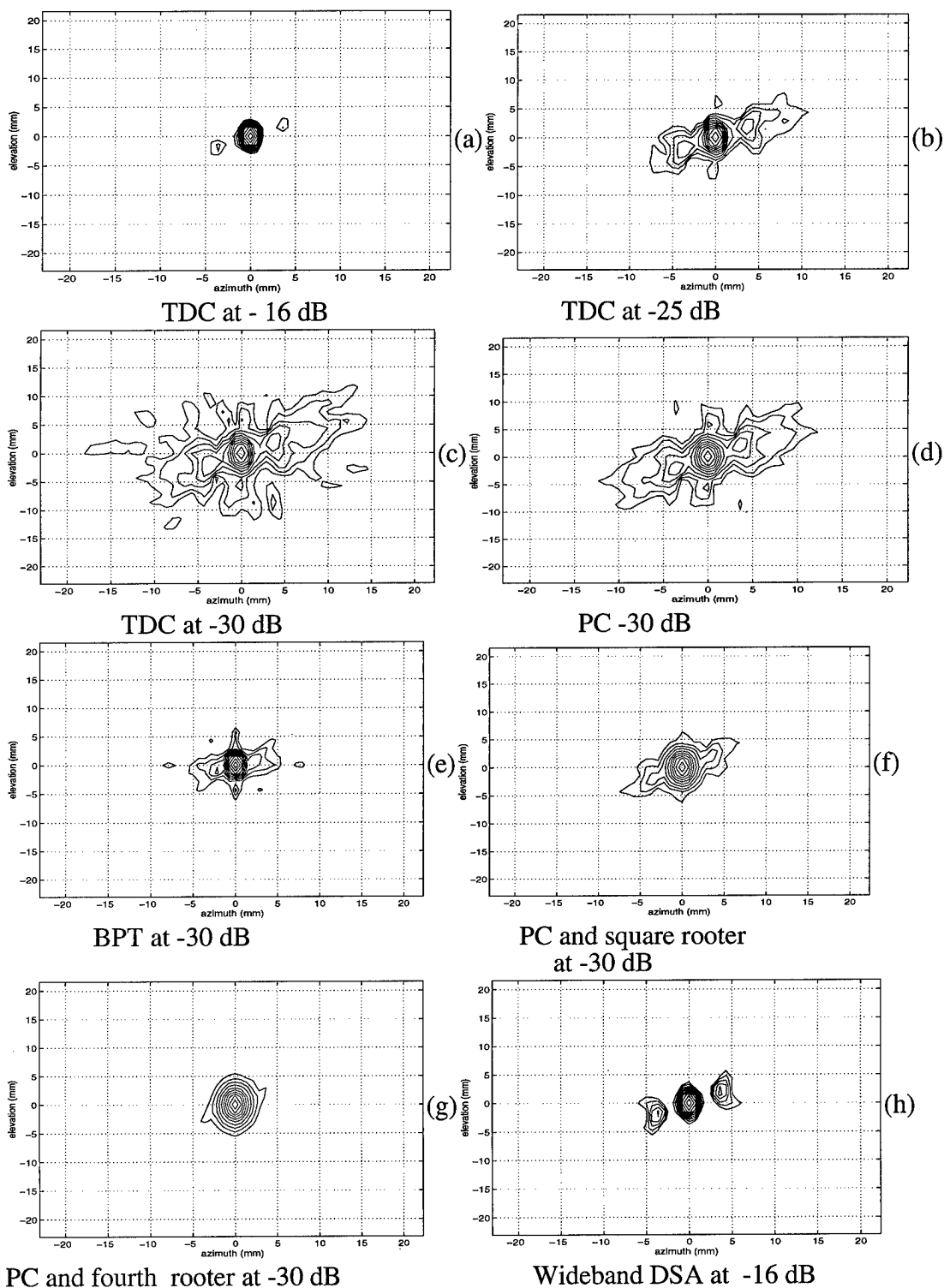


Fig.13. Distortion corrected contour maps of the sample image brs006 (see Fig.11 (b) and (c) for comparison) (a) TDC at -16 dB level. (b) TDC at -25 dB level and (c) TDC at -30 dB level. (d) PC at -30 dB level. (e) BPT at -30 dB. (f) PC and square rooter at -30 dB. (g) PC and fourth rooter at -30 dB. Wideband DSA at -16 dB. Artifacts are 5 dB higher than time-delayed correction shown in Fig.8(a).

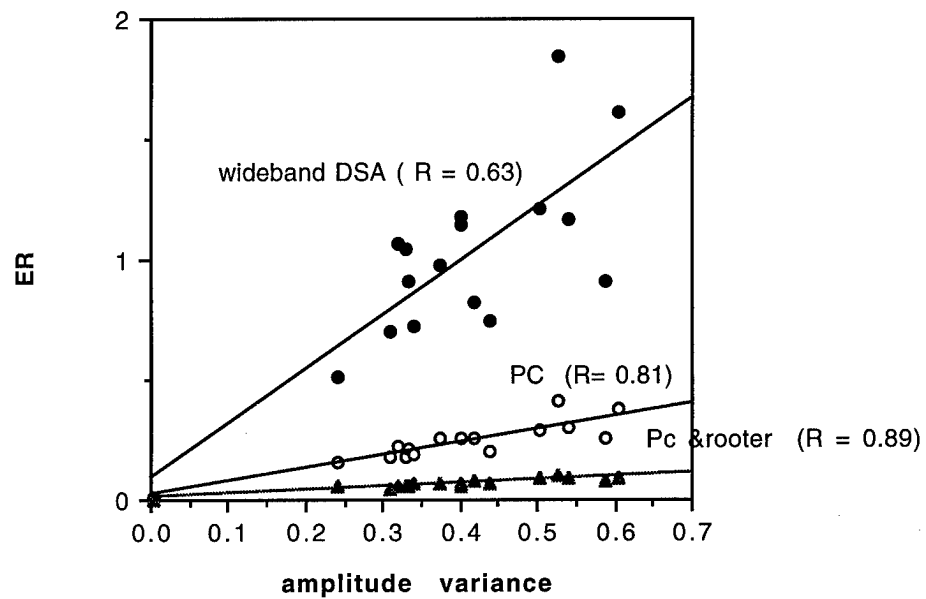


Fig.14. Linear regression plots of ER, after wideband DSA (upper), phase conjugation (middle) and phase conjugation & square rooter (bottom), vs. wavefront amplitude variance.

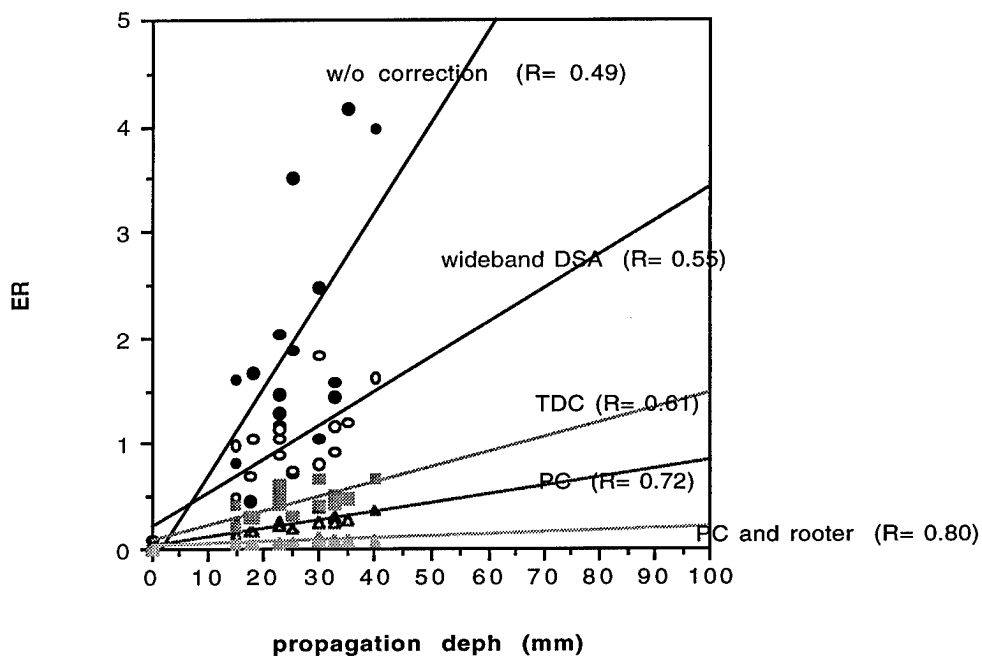


Fig.15. Linear regression plots of ER vs. propagation depth obtained from without correction (solid circle), wideband DSA (circle), TDC (solid square), PC (triangle) and PC and rooter (solid triangle). The correlation coefficients are give by R. One outlier was removed from (a).

Submitted to IEEE Ultrasonics,
Ferroelectrics, and Frequency Control
April 16, 1996*

Deaberration of Incoherent Wavefront Distortion: An Approach Toward Inverse Filtering

Qing Zhu, Member IEEE, Department of Radiology
Bernard Steinberg, Life Fellow IEEE, Valley Forge Research Center, The Moore School of
Electrical Engineering, University of Pennsylvania, Philadelphia, PA 19104

ABSTRACT — Techniques for the correction of ultrasonic wavefront distortion are compared using measured pulse transmission through human breast specimens. The measured data were obtained by recording the pulse signals on each element of a linear array that was moved in elevation to synthesize a two-dimensional aperture. The one-way point spread functions were reconstructed using matched filtering technique, phase conjugation, time-delay compensation and backpropagation followed by phase conjugation, each with and without amplitude compression. Two measures of performance were compared, beamwidth and the ratio of the energy outside the mainlobe to the energy inside the mainlobe. Matched filtering, which compensates the phase distortion but also increases the variation in the modulus, performs more poorly than other techniques with respect to both measures. Phase conjugation and time-delay compensation, which leave the magnitude of the wavefront unchanged, have similar beamwidths but phase conjugation is consistently superior with respect to energy ratio. The backpropagation method, which models wavefront distortion using a phase screen at a computed position between the source and aperture, is shown to perform better. The use of a novel amplitude compression that approaches inverse filtering improves the performance of the compensation techniques significantly. This is because inverse filtering optimizes image fidelity, in contrast, for example, to matched filtering, which optimizes SNR. With the amplitude compression method, the results of the one-way experiments show that the mainlobe shape can be recovered down to -30 dB.

* Address correspondence to Qing Zhu, 3400 Spruce Street, Radiology Department, University of Pennsylvania, Phila, PA 19104

I. INTRODUCTION

Adaptive compensation of wavefront distortion induced by tissue inhomogeneity is an active area of current research. Basic phase deaberration algorithms are recognized to be suitable only for weak scattering that can be modeled as a thin random phase screen located in the plane of the receiving aperture [1-3]. Extensions of the basic algorithms have been made to correct amplitude distortion in addition to phase distortion caused by strong scattering or distributed scattering [4-5]. However, it is shown analytically in [6] and experimentally in this paper that algorithms that take amplitude distortion into account can improve contrast resolution better than phase deaberration algorithms only if the algorithms reduce wavefront amplitude variance.

Consider complex signal vectors $\mathbf{S}_0(\mathbf{x})$ and $\mathbf{S}(\mathbf{x})$ received across an array in the absence and presence of distortion, respectively. The ratio of \mathbf{S} to \mathbf{S}_0 is a multiplicative distortion vector $\mathbf{f} = A \exp(j\phi)$. Fig.1 shows such a distortion vector \mathbf{f} for some instantaneous sample of the radiation field. The optimum compensation transformation is the right-most one which carries the distortion component of the complex sample to the intersection of the x-axis and the unit circle, for then both amplitude and phase are corrected. The left-most transformation is matched filtering (MF) which squares the amplitude and conjugates the phase. MF is theoretically optimum for maximizing SNR on a white, Gaussian channel. It is an optimum solution for detection (radar) but not so when fidelity is an important criterion, as in imaging. But it does satisfy the requirement for phase correction. Examples of MF algorithms are Dominant Scatterer Algorithm (DSA) [7] and Time Reversal Mirror (TRM) [4]. We should expect that MF algorithms are useful when wavefront distortion resides principally in phase, with amplitude relatively unaffected. Otherwise MF algorithms would be less effective than if amplitude were ignored and phase only were corrected. By squaring the wavefront amplitude, the MF

algorithms increase amplitude variance which contributes to the increase of energy in the sidelobe region [6].

A phantom consisting of a random phase screen placed at a receiving transducer models the situation where the element signal samples are correct in amplitude and are distorted only in phase by a random additive component. Phase aberration correction (PAC), consisting of phase conjugation (PC), is then the optimum compensator (See Section IV A). The signal amplitude is unchanged and the phase error is completely compensated by conjugation. This operator is represented by the 2nd (from the left) transformation. Time delay compensation (TDC) [1-3] is in the same class.

The right-most transformation which corrects both amplitude and phase is the inverse filter (IF). It is theoretically ideal for fidelity but has drawbacks. Because the IF adjusts the channel gain to be the reciprocal of the signal strength, at points in the receiving aperture where signal strength is weak the enhanced channel gain raises the noise to the point where SNR can be impaired. This is particularly troublesome when there is coherent refractive interference in the receiving array. A second potential problem, which we have avoided by not working too close to the IF point, is that an IF is unstable when the distorting medium has zeroes in the complex plane. Thus the right-most transformation carries the correction too far.

The complex weights of MF, PC and IF are, respectively, A , 1 and A^{-1} , each multiplied by $\exp(-j\phi)$. The signal after weighting is A^2 , A and 1 . The first and last are far from optimum for the reasons given. The 4th from the left transformation SR is a compromise. The correction vector is $A^{-1/2}\exp(-j\phi)$. The signal after weighting is $A^{1/2}$ (called later square rooter or rooter). Another transformation to the right of the square rooter is fourth rooter (signal amplitude is $A^{1/4}$ after weighting). In general, the correction

vector is $A^{-(M-1)/M} \exp(-j\phi)$ and signal amplitude is $A^{1/M}$ after transformation of the Mth rooter. In Section III, we demonstrate that low order rooters (square rooter and fourth rooter), in addition to phase deaberration at the aperture, can significantly improve contrast resolution without encountering the stability problem.

Backpropagating the received wavefront to an optimal backpropagation distance and performing phase deaberration at this optimal distance (BPT) [5] provides first order correction of wavefront amplitude distortion due to propagation from the backpropagation distance to the receiving aperture and therefore performs better than phase deaberration at the aperture. In Section III, we demonstrate experimentally that BPT transformation is somewhere to the right of TDC and PC and left of PC and rooter. We also demonstrate that square rooter in addition to BPT can significantly improve the performance of BPT.

The rooter transformation upon wavefront amplitude is a nonlinear compression operation (Fig.2). The detailed evaluation of the effects of this operation upon image can be performed by studying the amplitude distributions of images before and after the operation. This is a subject of a later study.

II. METHODS

A. *In Vitro Measurement*

The 2-D wavefront measurement system and procedure were described in detail in [8] and are summarized here for convenience. A breast tissue specimen was placed in the specimen holder with the skin facing the direction of the receiving transducer. The source was a hemispherical transducer emulating a virtual point source. The 2-D array consisted of a 92-mm 1-D linear array translated 46 mm perpendicular to its axis to form a synthetic 2-D array 92 mm x 46 mm. The element pitch in the receiving transducer was 0.72 mm and a reflecting mask reduced the receiving elevation to 1.44 mm. Transmission was one-way.

Frequency was 3.7 MHz. Bandwidth was 2 MHz. Waveforms were measured at each element, from which 2-D wavefronts were reconstructed as functions of time.

Breast tissue specimens were obtained fresh from reduction mammoplasty surgery and were stored frozen; they were later defrosted and degassed for the experiments. Each specimen was essentially planar and had a surface area of at least $7 \times 11 \text{ cm}^2$. The average thickness was 26.9 mm. The tissue donors were women ranging in age from 18 to 65 with a mean age of 34 years.

Three groups of measurements were made. The primary set consisted of independent measurements using nine different specimens. In addition, two specimens were employed for sequential measurements in which an approximately 1-cm layer was removed from the bottom of the specimen before each subsequent measurement. For three other specimens, a pair of measurements was made with the source in each of two positions located 12 mm apart in the array direction. A total of 16 measurements were made. Water measurement was also made for comparison. In the following analysis, the sequential measurements were treated as measurements from different samples because the samples resulting from approximately 1-cm removal from the original samples were replaced into the sample holder after cutting, and their relative positions to the 2-D transducer aperture changed unpredictably. The pair measurements resulting from 12 mm lateral source translation were also treated as measurements from different samples because the measured parameters and the point-source image properties were changed due to the highly inhomogeneous nature of the breast tissue.

B. Data Processing

Pulse arrival time at each element was calculated by using a differential edge detector to locate the first negative peak of the pulse. Geometric effects were removed by fitting a

two-dimensional, fourth-order polynomial to the calculated arrival time surface and subtracting the result. The reasons for using fourth-order polynomial fitting were given in [5]. 3-D image data were calculated by (1) Fourier decomposition of the temporal waveforms at each (x,y) position in the aperture, (2) calculation of a complex CW 2-D image at each Fourier frequency in the focal plane by using the angular spectrum technique [16], and (3) summation of the 2-D images to form the 3-D transient image. The final 2-D image used in this report was obtained by detecting the peak pressure value at each (xf,yf) position in the image plane within the transient period. Contour maps of 2-D point source images at different thresholds are used to quantitatively evaluate image quality.

Before Fourier decomposition, the received pulse at each element was temporally weighted by a 10-point cosine taper over the trailing 10 points of a 40-point time window that contained the main arrival pulse. The original 40-point interval was padded with zeros to a 128-point interval.

In step (1), a frequency range (0.31 - 6.25 MHz) that contained most of the signal energy was chosen. This range corresponds to the 3rd through 41st harmonic of the FFT of a signal sampled at 20 MHz over a 6.4 μ s interval containing 128 points.

In step (2), the complex signals in the 128×32 spatial aperture were zero padded symmetrically to 256×64 before each harmonic component in the 2-D aperture was focused in the image plane via the angular spectrum technique. Spatial raised cosine taper was employed. The system bandwidth is about 50%; therefore $Q = \frac{f_0}{\Delta f} \approx 2$, where f_0 is the central frequency. For such Q , the first sidelobes (due to finite aperture size) in both principal axes remain [9], and are reduced to about -30 dB level by employing the raised cosine taper [10].

C. Correction Methods

Two basic phase deaberration algorithms, time-delay compensation (TDC) and phase conjugation (PC), and two wavefront compensation algorithms, wideband DSA and BPT, were applied to each measured 2-D wavefront set and their effects upon focusing were compared. Square rooter and fourth rooter on wavefront amplitude in addition to PC and square rooter in addition to BPT were also implemented and their effects upon focusing were compared with the other four deaberration algorithms.

TDC: An arrival time fluctuation profile at the aperture is calculated in three steps.

Step 1: A reference waveform with good signal-to-noise ratio is first selected from geometrically corrected waveforms. The selected waveform is continuously modified to reduce the effect of the arbitrariness in the initial selection as waveforms in the aperture are cross-correlated with it. The modification is accomplished by time-shifting and adding a new waveform to the reference pulse if the peak value of the correlation function between the new waveform and the current reference waveform is greater than 0.8. The average total number of waveforms that are incorporated into the final reference waveform selection is 2690 (std. 391), which accounts for 66% (9.5%) of the total pulses. The average is calculated upon a total of 16 *in vitro* samples. This selection procedure is similar to the one developed in [5].

Step 2: The arrival time fluctuation profile is first calculated from cross-correlation peaks of geometrically corrected waveforms and the reference waveform when the peak values of the correlation function between the waveforms and the reference waveform are greater than 0.7. At this step, the average total number of waveforms that are incorporated into the calculation of the arrival time profile is 3518 (std. 173), which accounts for 86% (std. 4.2%) of the total pulses.

Step 3: For the bad waveforms with cross-correlation peaks less than 0.7, the arrival time fluctuations at these positions are calculated as follows: (1) calculate cross-correlation peaks between each bad waveform and neighbor waveforms (within a 5 by 5 spatial window) that are incorporated in Step 2; (2) select those neighbor waveforms having cross-correlation peaks, calculated in (1), greater than 0.5; (3) calculate the average of arrival time fluctuation from arrival time differences between the bad waveform and the selected neighbor waveforms, and the arrival time fluctuations of the corresponding neighbor positions. This average is assigned to the bad waveform position. A justification of this step is that for badly distorted waveforms, they are dissimilar to the reference waveform to a large extent, but they are somewhat similar to the waveforms in the closest neighborhood which are reasonably correlated with the reference waveform. After this step, the average total number of pulses that are incorporated into the calculation of the arrival time profile is 3966 (std. 41) which accounts for 97% (std. 1%) of the total pulses.

For the waveforms that have not been incorporated into the calculation of the arrival time profile after Step 3, arrival time fluctuations at these positions are assigned to zero. The calculated average arrival time fluctuation of the entire 16 profiles is 37.6 ns with a 10.5 ns standard deviation.

Except for TDC, the following correction procedures were implemented upon the complex wavefront at each frequency after Fourier decomposition. The image formation procedures after using each correction method were the same as the procedures described in part B steps (2) and (3).

PC: Let $A_f(x,y)\exp(j\phi_f(x,y))$ represent the complex signal at each frequency after Fourier decomposition, where A_f and ϕ_f are functions of positions (x,y) in the 2-D array at frequency f . The complex weight vector of phase conjugation is $w_f = \exp(-j\phi_f)$ and the

signal after weighting is A_f . The image formation after phase conjugation is the same as described in part B, steps (2) and (3). Phase conjugation at each frequency within the signal band (without amplitude weight) provides perfect phase compensation except for a 2π phase jump. The result is better than TDC because of the removal of residual phase error. The wavefront amplitude distortion remains, however. The objective here is to evaluate the limit of phase compensation and the extent of the wavefront amplitude distortion effect.

Wideband DSA: The complex weight vector of DSA at each frequency is $w_f = A_f \exp(-j\phi_f)$ and the signal after weighting is A_f^2 .

Wideband DSA is an approximation of the TRM receive mode developed in [11]. The difference between wideband DSA and TRM receive mode is the scanning procedure. At target position A (Fig.3), wideband DSA and TRM receive mode produce exactly the same responses, because of the reciprocity principle. At non-target position B, wideband DSA uses linear geometry between A and B to scan the beam while the TRM receive mode could backpropagate the wave to the aberrator position, and then use linear geometry to scan the beam [11]. However, for points that are within the correlation distance of A, wideband DSA and the TRM receive mode should produce similar responses. The correlation distance of the breast is about 4-5 mm [8],[12],[13-14]. Therefore within a 4 - 5 mm radius, we should expect similar performances of wideband DSA and TRM receive mode. The objective of using wideband DSA here is to evaluate the possible improvement of deaberration due to the additional SNR gain provided by amplitude weighting.

BPT: BPT, developed in [5], is implemented by backpropagating the complex wavefront at each frequency after Fourier decomposition to the optimal distance and then using *phase conjugation* at that distance. The use of phase conjugation instead of TDC at

the backpropagation distance reduces the complexity in the calculation. The backpropagation distances are taken from [8].

Rooters:

PC and square rooter: The weight vector of PC and square rooter at each frequency is $w_f = A_f^{-1/2} \exp(-j \phi_f)$ and the signal after weighting is $A_f^{1/2}$.

PC and fourth rooter: The weight vector at each frequency is $w_f = A_f^{-3/4} \exp(-j \phi_f)$ and the signal after weighting is $A_f^{1/4}$.

BPT and square rooter: BPT and square rooter was implemented the same as PC and square rooter but the procedure was done at the optimal back propagation distance after backpropagating each complex wavefront to the optimal distance.

III. EXPERIMENTAL RESULTS

A. Correction of Scattered Energy

1) Correction upon scattering samples

Figs.4 (a) and (b) show -6 dB contour plots of images obtained from the water path and the 3.5-cm breast tissue path (brs005). Contour spacing is 1 dB. Abscissa and ordinate are azimuth and elevation in mm in the image plane. Fig.4(a) shows the system diffraction pattern at -6 dB. The azimuthal beamwidth is about 1.5 mm (at a distance of 180 mm) meaning that the point (or lateral) resolution is $1.5/180$ or 8.3 mrad. Because the size of the receiving array in elevation is half the size in the array direction, the width of the image in elevation is twice as large as in azimuth. When tissue is present (b), the image lobe is broadened. In (b) the beamwidth has grown from 1.5 mm to 3 mm in azimuth and 3.1 mm to 9.3 mm in elevation and the point resolution has worsened approximately 2:1 in azimuth and 3:1 in elevation. A symmetrical scattering pattern appears when the threshold is

reduced. Fig.4 (c) shows a -20 dB contour plot of the sample image brs005. Contour spacing is 2 dB. Energy is spread out over a large area. No distinct structure or multipath lobe can be identified from the image.

Fig.5 (a)-(g) shows the correction result of the sample image brs005 by using different methods. Part (h) is the -30 dB level contour of a water path image. The contour spacings in Fig.5 are the outer contour levels divided by 10. Fig. 5 (a)-(c) shows TDC at -6, -20 and -30 dB levels (see Fig.4(b) and (c) for comparison). Image quality improved significantly and the system diffraction pattern is restored up to -20 dB level. The symmetric scattering pattern outlined by outer contours at the -30 dB level is caused by residual phase errors after phase deaberration and incoherent amplitude distortion. Fig.5 (d) is the correction result of PC at the -30 dB level. Because of the complete removal of phase errors except for a 2π jump, the scattering pattern is further improved as compared to (c). Fig. 5 (e) is the result of BPT, and the scattering pattern is much better than that of PC at the aperture. The optimum backpropagation distance of this tissue sample is 30 mm. It is interesting to note that the beamwidth is narrower than that obtained through other methods. The reason is that the actual aperture is moved 30 mm closer to the source and the beamwidth is $(R\text{-optimal backpropagation distance})\frac{\lambda}{L}$ instead of $R\frac{\lambda}{L}$, where R is the distance between source and the receiving aperture, and L is the aperture size. Fig.5 (f) is the correction result of PC and square rooter on wavefront amplitude at -30 dB. The pattern is very close to the system diffraction pattern (see (h) for comparison). Fig.5(g) is the result of wideband DSA at the -30 dB level. The correction result is worse than those of other methods (see Section IVC).

2) Correction upon samples with well-defined multipath

In most breast samples, scattering and coherent interference are both present. Fig.6 (a) and (b) are -10 dB contour plots of images obtained from the water path and the 4-cm

breast tissue path (brs006). Contour spacing is 2 dB. In tissue image (b), three lobes instead of one central image lobe appear. Inner contours of the image lobe are close to the system diffraction pattern (Fig.6(a)) while the outer contours are highly irregular due to scattering. The point resolution is worsened by approximately 2:1 in azimuth and 3:1 in elevation. Two refractive lobes appear at $(-4, -2.5)$ and $(3.5, 1.5)$, and their strengths are -6 and -8 dB. A closer examination is obtained from 45 degree cuts (Fig.7) of the Fig.6 (a) and (b) images. In Fig.7 (a), the peak sidelobe is -36dB, which is the best we can obtain from the measurement system. In the tissue image, two large sidelobes (-6 dB and -8 dB) appear on either side of the mainlobe. The two nulls between the lobes are deep (left : -13 dB below peak, right: -15 dB), which is a typical coherent interference phenomenon [15].

A symmetric scattering pattern generally appears when the threshold is reduced, as shown Fig.6(c) with a -16 dB threshold contour and contour spacings of approximately 1.5 dB. The outer contours show a roughly symmetric pattern typical of scattering while the inner contours show an asymmetric lobular interference pattern.

Fig.8 shows correction results of the sample image brs006 after applying different methods. The contour spacings are the outer contour levels divided by 10. Fig.8(a) is the -16 dB contour map of applying TDC (see Fig.6(c) for comparison)). Image quality improved significantly because of the minimization of the phasefront distortion caused by scattering. The area within the -16 dB inner contour is reduced by a factor of 11. The mainlobe pattern is close to the system diffraction pattern although the area is still 1.6 times larger than the area in water at the same level. Two large lobes remain as expected and appear as two additional sources. Fig.8(h) is the correction result at a -16 dB level of applying wideband DSA. It is evident that the procedure enhances interference in this example; the artifacts are 5 dB higher than in Fig.8(a). The reason is given in [6]. Figs.8(b) and (c) show -25 and -30 dB contour plots of TDC. In Fig.8(b) the outer

contours show an asymmetric interference pattern with scattered energy distributed around the two interference lobes. In Fig.8(c) the outer contours show the more symmetric scattering pattern caused by incoherent wavefront amplitude distortion and residual phase distortion. Fig.8(d) is the result of PC at -30 dB. The approximately symmetric scattering pattern outlined by outer contours in (c) is improved due to better phase deaberration. The energy is more concentrated around the image lobe and interference lobes. Part (e) is the result of BPT, and the scattering pattern is further improved as compared with the result of PC at the aperture. The backpropagation distance of this sample is 50 mm. Part (f) is the result of PC and square rooter at -30 dB. The pattern is very close to the system diffraction pattern. PC and fourth rooter shown in Fig.8(g) restores the diffraction-limited image to a -30 dB level.

It is interesting to note that the strengths of the two interference lobes are also reduced by 8 dB after TDC and PC. They are further reduced by 5, 7 and 15 dB after BPT, PC and square rooter, and PC and fourth rooter, respectively. The improvement comes from the scattered energy which is originally distributed around the mainlobe and each of the refracted multipath lobes. This energy is coherently added back, by the deaberration process, to the dominant lobe, which in this case is the mainlobe. The overall result is an improvement of the image lobe to the interference lobe ratio.

Determination of whether interference was coherent or scattered was based upon whether or not large lobes could be removed by applying phase-deaberration algorithms. Another indicator is whether or not a lobe location moves (scattering) or remains relatively the same (refraction) after the phase deaberration process. Both means were used to identify whether these lobes were produced by refraction or scattering. Large lobes in nine samples are believed to be caused by the interference process. In these samples, we have found an

average of a 10 dB (std. 4dB) improvement in the range of 5-16 dB after TDC, due to the coherent strengthening of the mainlobe.

B. Correction statistics

We analyzed images at different contour levels and classified the total of 16 samples into three categories: 1) Primarily scatter (4 samples); 2) More scatter than refraction (3 samples); and 3) Scatter plus well-defined refraction (9 samples). Statistics of -6 dB point resolution of three groups is given in Table I. The average beam-broadening as compared with water is 70% in azimuth and 57% in elevation. These numbers are larger than the result reported in [14] where an 18% increase in beamwidth at the same threshold is observed. This is likely due to the different aperture sizes used. For the samples with refractive artifacts, the point resolution is evaluated upon the central image lobe. The percentage increase in beamwidth of the scatter group is significantly larger than that of the other two groups. It is obvious that point resolution is not enough to evaluate image distortion when multiple lobes are present. Statistics of refractive lobes of the third group is given in Table II. In this group, we found 1-3 refractive lobes at levels between -4 and -17 dB (peak value), all within a radius of 1-3°.

A simple metric, the lowest level at which mainlobe diffraction shape is maintained, is used here to quantitatively evaluate improvement upon image quality by using different correction algorithms. The mainlobe diffraction shape is identified when the elevation-image width to the horizontal width is approximately a 2 to 1 ratio and the outermost image contour has an elliptical shape. At the levels selected, 65% of ratios are within 0.1 of 2 to 1, 27% within 0.2 of 2 to 1 and 8% within 0.3. This metric is closely related to contrast resolution for the multiple target case, because this is the level at which a smaller neighbor target would begin to be detectable. For a simple scattering case, the measurement of this

metric is straightforward. For a complicated scattering and multipath case, the meaningful measurement is the level at which the mainlobe diffraction shape is maintained and is also above any multipath artifacts.

The average levels (std. dev) of the restored mainlobe diffraction shape before and after corrections of the three groups classified earlier are given in Table III. The mainlobe shape is restored up to -19.3 (2.4) and -19.5 dB(2.6 dB) by using two phase-deaberration algorithms, TDC and PC, respectively. The fact that the correction result of TDC is very close to that of PC suggests that the limit of phase correction with respect to the selected metric has been achieved by TDC. Further improvement requires correction algorithms that can take wavefront amplitude distortion into account. Wideband DSA is able to restore the mainlobe shape to -14.8 dB (2.3 dB). This result is about 5 dB worse than that of using two phase-deaberration algorithms. The cause is the increase of wavefront amplitude variance by squaring the amplitude. Wavefront amplitude variance contributes to the energy in the sidelobe region [6]. BPT at an optimal backpropagation distance improves the performance of PC at aperture by 5 dB. PC and square rooter on wavefront amplitude restores the mainlobe diffraction shape to -25.4 dB (2.6 dB). The correction result of BPT is similar to PC and square rooter. PC and fourth rooter achieves a -31.1 dB (1.7 dB) level, which is about a 12 dB improvement beyond two phase deaberration algorithms. This level is very desirable for a high quality ultrasound echo scanner. BPT and square rooter at an optimal backpropagation distance further improves BPT by another 5 dB.

The restored mainlobe diffraction levels among different groups are similar when different correction methods are used. But the improvements are, in general, 6 dB larger in the scatter group than that of the other two groups because the mainlobe shape is distorted at zero dB in the scatter only group.

C. Depth-dependent Distortion and Correction

Scattered energy increases with the propagation depth D . Using first order approximation, it is shown analytically in [6] that wavefront amplitude variance $\sigma_{A_t}^2$, and phase variance or arrival time variance σ_t^2 , linearly increase with propagation depth. $\sigma_{A_t}^2$ is calculated as follows: 1) calculate energy at each (x,y) position at the aperture by summing the energy over the time window; 2) calculate amplitude at each (x,y) position by taking the square root of the energy; 3) calculate the reference amplitude profile which is the fourth order polynomial fit of the measured amplitude profile; and 4) calculate normalized amplitude variance of the measured amplitude profile divided by the reference amplitude profile. The calculation of σ_t^2 is described in Section II.C. Fig.9 shows the linear regression plots of $\log(\sigma_t^2)$ and $\log(\sigma_{A_t}^2)$ vs. $\log(D)$. The correlation coefficients are 0.55 and 0.74, respectively. Two outliers are removed from (a). The slopes are in the order of unity. In both plots, the linear relationships are statistically significant*.

A quantitative measure of scattered energy at the image plane is the energy ratio ER, which is defined as the energy outside the main image lobe to the energy inside the main image lobe. It is shown analytically in [6] that ER linearly grows with the propagation distance D . ER is directly related to image contrast and is calculated by taking the ratio of energies measured outside the mainlobe region and inside the mainlobe region. The mainlobe region is identified by linear extrapolation between the peak image value and the outer contour of the mainlobe diffraction pattern at the lowest recognizable level. Fig.10 illustrates the measurement procedure. Fig.11(a) upper curve is the linear regression plot of ER vs. D without correction. One outlier was removed from the data. ER in water

* The linear relationship is statistically significant ($\alpha=0.05$) if the correlation coefficient is greater than 0.53 for sample size 14 and 0.497 for sample size 16.

image is 0.088, which is included in the data points to represent system performance at zero depth. The correlation coefficient is 0.49 and the linear relationship is significant. The low correlation coefficient is due to the difficulty of identifying the diffraction pattern for some severely distorted images. In Fig.11, all regression lines are extrapolated to 100 mm propagation depth, which is considered the maximum penetration depth of breast under soft compression. The regions beyond 50 mm were shaded to represent lower confidence in extrapolation.

The performances of descattering algorithms deteriorate with propagation depth. The rest of the regression curves in Fig.11 (a) show ER vs. propagation depth obtained by using five different correction methods. ERs in water alone data provided the values at zero depth. The correlation coefficients of regression curves are indicated in the figure by R. The average values of ER (std. dev.) are given in Table IV. The linear relationships are statistically significant for all curves.

The performance of wideband DSA is the lowest among all correction procedures. Data sets of wideband DSA, PC and PC and rooter are clearly separated with averages 103% (std. 33.9%), 25% (6.9%) and 6.8% (1.6%), respectively. The ER ratios of wideband DSA and PC, and PC and PC and rooter are 4.1 and 3.7, respectively. These results agree very well with the factor of 4 prediction given by analysis in [6]. At 100 mm depth, ER after PC reaches 0.85, which is in the neighborhood of the average ER with DSA correction at the average 2.7 cm propagation depth. Therefore, the best linear phase correction procedure at the aperture is likely to result in only 15 dB image contrast at this depth. The average ER after TDC is 19% more than that of PC while the averages of the lowest level at which mainlobe diffraction shape is maintained are the same when TDC and PC are used. This implies that the residual phase error due to imperfect phase correction contributes primarily to energy in the sidelobe lobe region. BPT reduces the average ER by

12.2% below that of PC and is the best among the linear operations. The performance of PC and square rooter at the aperture is slightly better than that of BPT. At 100 mm, the PC and rooter curve reaches 0.22 which is about the average ER level of PC. The BPT curve reaches 0.38, which is about the average ER of TDC. These energy ratios are useful to provide image contrast of ~20 dB.

Fig. 11 (b) shows the results of ER by using BPT and square rooter and PC and fourth rooter at the aperture. Regression curves obtained from PC and square rooter and BPT are also included in (b) for comparison. At 100 mm depth, the regression curves of BPT and square rooter and PC and fourth rooter reach 0.11 and 0.05, respectively. These ERs are about the average levels of BPT and PC and square rooter obtained from the average 2.7 cm propagation depth (see Table IV). The result indicates that focusing with image contrast of ~25 dB throughout the 100 mm propagation depth may be achievable by taking the low order root on wavefront amplitude in addition to phase deaberration at the aperture or in addition to BPT.

Image contrast, the lowest level of the mainlobe diffraction shape, increases monotonically with ER. The relation of the two can be predicted by using ER and image contrast obtained with PC (or any correction method) as a base line (bold numbers in Table V). For example, the measured image contrast with PC is 19.5 dB. The ER ratio of PC alone to PC and rooter is $25.1/6.8 = 3.7$, corresponding to increase of 5.7 dB. Thus the predicted image contrast is $19.5 \text{ dB} + 5.7 \text{ dB} = 25.2 \text{ dB}$, which closely agrees with the measured value -25.4 dB. Table V lists the measured ER (first row), predicted image contrast from the measured ER (second row) and the measured image contrast (third row). The predicted and measured image contrasts are in reasonably good agreement except for the pair without correction. The reason is due to ER measurement error in images without

correction. For some severely distorted images, it is often difficult to identify the mainlobe region.

Refracted energy exhibits a different depth distortion effect than scattered energy. The strengths and the numbers of interference lobes depend on orientations, curvatures, sizes and numbers of refractive bodies in the insonified medium, and may not be directly related to propagation depth. Although the chance of incident rays passing through more refractive bodies increases with the propagation depth, the strengths of interference lobes resulting from multiple refraction may not be significant compared with those resulting from single refraction. One quantitative measure of coherent interference phenomenon is the ratio of a large interference lobe or artifact to image lobe. For nine samples that were determined to have significant levels of coherent interference, the ratio varied randomly from sample to sample and showed no increase with thickness. The average strength (peak value) is 10 dB (std. 4 dB). Another quantitative measure is the total number of large refractive lobes in each image (Table II). The average is 2 and standard deviation is 0.53. The lobe number is independent of propagation depth. The refractive lobes are tightly clustered around the main lobe with an average radius of 5.6 mm (std. 1.8 mm) which is about 2 degrees. This is because the speed variations across glandular tissue and fat boundaries are small (5-10%).

IV. DISCUSSION

A. Comparison of TDC and PC

Experimentally we found that PC and TDC, which leave the magnitude of the wavefront unchanged, have similar performance with respect to beamwidth but PC is consistently superior with respect to energy ratio. The following analysis explains the reason.

We model the received pulse as the transmitted pulse convolved with the medium induced distortion, i.e., $r(t, x_i) = p(t) * m(t, x_i)$, where $m(t, x_i)$ is the impulse response of the medium from the source position to the receiver element x_i . Assume that system noise is negligible. The estimation of the arrival time profile of $r(t, x)$ across the receiving aperture is calculated by cross correlation of neighboring signals as

$$O = \max_{\tau} \left[\int_{-\infty}^{+\infty} p(t) * m(t, x_i) \times p(t) * m(t - \tau, x_j) dt \right]$$

The quality of the estimated profile is highly affected by the waveform distortion $m(t, x_i)$ across the receiving aperture; i.e., the estimation of arrival time profile is coupled with the wavefront amplitude distortion. In the frequency domain, $R(\omega, x_i) = P(\omega) \times M(\omega, x_i)$, where the medium distortion $M(\omega, x_i)$ has amplitude $a(\omega, x_i)$ and phase $\exp(j\omega t_0(x_i))$. Since $\exp(j\omega t_0(x_i))$ is decoupled from the amplitude of $R(\omega, x_i)$ by multiplication, the phase conjugation operation at each frequency completely compensates $t_0(x_i)$ independent of amplitude error. Therefore, PC is better than TDC in correcting residual phase error, which primarily contributes to the energy in the sidelobe region.

B. Importance of Better Phase Correction

We have shown in Table IV that PC, the best phase deaberration procedure at the aperture and ideal for a point target, improves ER 19% more than TDC, while the averages of the lowest level at which mainlobe diffraction shape is maintained are the same by using both procedures. This implies that residual phase error due to imperfect phase correction of TDC primarily contributes to the energy in the sidelobe region. Therefore better phase deaberration procedures that improve the performance of TDC are valuable to improve the contrast resolution.

The procedure to calculate TDC profile used in this paper is ad hoc. Steps 2 and 3 in the TDC calculation (Section II) smooth the arrival time fluctuation estimate to a certain extent. To test the effect of the ad hoc smoothing, another TDC estimate procedure was used. We call this procedure nonsmoothing TDC. In this procedure, the reference waveform selection in the previous TDC estimate was unchanged but steps 2 and 3 were

replaced by simply calculating the cross-correlation peaks of correlation functions between geometrically corrected waveforms and the reference waveform. The image formation was the same as before. The simple metric, lowest level at which the mainlobe diffraction shape was maintained, and ER after using nonsmoothing TDC, were measured. The average level of the simple metric is -18.9 dB (std 2.4 dB) and the average ER is 41.4% (11.2%). The corresponding results of using smoothing TDC are -19.3 dB (std. 2.4 dB) and 44.2% (13%). Thus, smoothing does not significantly improve image quality. The reasons are 1) an average 86% of pulses are highly correlated with the reference waveform (correlation coefficient 0.7) and arrival time fluctuations calculated at these positions are reasonably good; and 2) for 14% of pulses that are not correlated well with the reference waveform, estimation errors of arrival time fluctuation occur at these positions. But signals at these positions are, in general, weak and therefore arrival time estimation errors at these positions contribute little to image quality.

C. Effects of Amplitude Weight of Compensation Vector

The complex weights of MF, PC and PC and square rooter are, respectively, A , 1 and $A^{-1/2}$, each multiplied by $\exp(-j\phi)$. The signal after weighting is A^2 , A and $A^{1/2}$. By using first order approximation, it is shown in [6] that the variance of A^2 is about 4 times larger than $\sigma_{A_t}^2$, while the variance of $A^{1/2}$ is about 4 times smaller when a narrowband waveform is used, where $\sigma_{A_t}^2$ denotes the variance of A . These increases and decreases in amplitude variance account for the linear increase and decrease in sidelobe energy ER [6]. Experimentally, we measured a 4.1 and 3.7 increase and decrease in ER compared with the ER of using PC when wideband DSA and PC and rooter are used, respectively (Table IV). The results agree with the analysis and indicate that intelligent use of amplitude weighting is crucial for improving image contrast.

D. Application to Diffuse Scattering Medium

The compression operation upon wavefront amplitude, in addition to phase deaberration or BPT, introduced in the paper is applicable to a diffuse scattering medium. Experiments with square root amplitude weighting and TDC show that ER can be reduced by 15.6% on average relative to TDC alone. Further comparison studies of image amplitude distributions before and after compression will be performed to quantify the nonlinear effects upon image quality. The required degree of compression will be optimized as a function of contrast resolution and SNR.

E. Significance of Coherent Interference in Pulse-echo Imaging

A coherent interference phenomenon was demonstrated in the 1-way transmission model and experiments. Its impact upon 2-way echo scanning is illustrated in Fig.12. A transmitting beam illuminates a tumor or target T (part a). Because of refraction, a subbeam is split from the original beam and insonifies targets along θ_1 . On reception, if no echo signal is coming back from the targets illuminated by the subbeam (simplest case), the receiving beam upon T (part b) may split in the same fashion as the transmitting beam (reciprocity) and a dual image may result. This simplest case corresponds exactly to the situation in the 1-way transmission experiments reported in this paper, and in [13-15], where an active point source instead of a passive point target is used. In reality, refracted energy from the targets insonified by the subbeam will arrive at angles of $1 - 30^\circ$ from the target direction and therefore in the sidelobe region of array. The sidelobe level of the receiving beam will be ~ -30 dB as achieved by the procedure described in this paper. The average level of refracted multipath is found to be -10 dB relative to the target image and therefore the average multipath signal level entering the system is $\sim (10+30)$ dB below the echo strength of the illuminated target. Cancellation algorithms [15] must further suppress

these multipath signals to achieve a -60 dB contrast resolution, which is essential for preventing contamination of otherwise black cysts with scattered and/or refracted echo energy and thereby causing them to look like speckled tumors.

V. CONCLUSIONS

The evidence of both scattering and refraction is observed from point source images obtained from *in vitro* breast samples with thickness varying from 1-4 cm. Scattering reduces target strength, broadens the mainlobe and increases background level and therefore lowers the image contrast. Refraction creates coherent multipath interference that produces false targets in addition to the true target in the image. Scattered energy increases with the propagation depth while refracted energy does not appear to increase with the depth.

Phase deaberration algorithms are useful to partially remove scattered energy and build up the strength of the coherent image. As a result, the diffraction-limited image is restored up to -20 dB level for average thickness of 2.7 cm. Better phase deaberration procedures are valuable to improve energy ratio and therefore image contrast. Improvement of a diffraction-limited image to the -30 dB region requires wavefront-deaberration algorithms that can further remove scattered energy caused by wavefront amplitude distortion and consequently strengthen the coherent image. BPT reduces wavefront amplitude variance and provides 5 dB improvement in addition to that of using phase deaberration procedures at the aperture. Wideband DSA increases wavefront amplitude variance and the result is 5 dB worse than phase-deaberration procedures alone for the tissue thickness studied. A low order root of the wavefront amplitude, in addition to phase-deaberration at the aperture or BPT, can further reduce the amplitude variance and restore the diffraction-limited image to the -30 dB region. Linear regression analysis of ER vs

propagation depth indicates that high quality focusing as far as 50 - 100 mm propagation depth is possible.

The ratio of multipath artifact to image lobe is improved by an average of 10 dB when phase deaberration is used and further improved by another 10 dB when the low order root upon wavefront amplitude, in addition to phase deaberration or in addition to backpropagation and phase deaberration, is used. The improvement comes from the coherent build up of the target strength by descattering.

ACKNOWLEDGMENTS

The authors would like to thank Professor Robert Waag, Departments of Electrical Engineering and Radiology, University of Rochester, Rochester, for his helpful comments and suggestions on the manuscript. The *in vitro* measurements were done with the collaboration of Ms. Laura M. Hinkelman and Professor Waag. Invaluable consultation was provided by Dr. Kai Thomenius, Director of Research, Interspec, Inc., Ambler, PA., a division of ATL, in the course of this study. Funding was provided by the Army (DAMD 17-93-J-3014 and DAMD 17-94-J-4133).

REFERENCES

- [1] S. W. Flax and M. O'Donnell, "Phase Aberration Correction using Signals from Point Reflectors and Diffuse Scatterers: Basic Principles," IEEE Trans. Ultrason., Ferroelec. and Freq. Contr., 35(6), 758-767 (1988).
- [2] E. H. Attia and B. D. Steinberg, "Self-Cohering Large Antenna Arrays Using the Spatial Correlation Properties of Radar Clutter," IEEE Trans. Antennas Prop., AP-37(1), 30-38 (1989).
- [3] L. Nock, G. E. Trahey, and S. W. Smith, "Phase Aberration Correction in Medical Ultrasound using Speckle Brightness as a Quality Factor," J. Acoust. Soc. Am. 85(5), (1989)
- [4] M. Fink, "Time reversal of ultrasonic fields - part I: basic principles," IEEE Trans. Ultrason. Ferroelec. Freq. Contr., vol. 39, pp. 555-566, 1992.
- [5] D.-L. Liu and R. C. Waag, "Correction of Ultrasonic Wavefront Distortion Using Backpropagation and Reference Waveform Method for Time-shift Compensation," J. Acoust. Soc. Am. 96, 649-660 (1994).

- [6] Q. Zhu and B. Steinberg, "Modelling and Correction of Incoherent Wavefront Distortion," Will appear in Special Issue of International Journal of Imaging Systems and Technology.
- [7] B. D. Steinberg, "Radar Imaging from a Distorted Array: The Radio Camera Algorithm and Experiments," IEEE Trans. Antennas Prop. AP-29(5), 740-748 (1981).
- [8] L. M. Hinkelman, D-L. Liu, and R. C. Waag, Q. Zhu, and B.D. Steinberg, "Measurement and Correction of Ultrasonic Pulse Distortion Produced by the Human Breast", J. Acoust. Soc. Am. 97(3), 1958-1969 (1995).
- [9] B. D. Steinberg and H. Subbaram, *Microwave Imaging Techniques*, Chapter 3, John Wiley and Sons, New York (1991).
- [10] B. D. Steinberg, *Principles of Aperture and Array System Design* (Hohn Wiley & Sons, New York, 1976).
- [11] C. Dorme and M. Fink, "Focusig in transmit-receive mode through inhomogeneous media: The time reversal matched filter approach," J. Acoust. Soc. Am. 98, 1155-1162 (1995).
- [12] Q. Zhu, B. D. Steinberg and R. Arenson, "Correlation Distance of the Female Breast," J. Acoust. Soc. Am. August (1995).
- [13] G. E. Trahey, P. D. Freiburger, L. F. Nock, and D. C. Sullivan "In Vivo Measurements of Ultrasonic Beam Distortion in the Breast," Ultrason. Imag. 13, 71-90 (1991).
- [14] P. D. Freiburger, D. C. Sullivan, B. H. LeBlanc, S. W. Smith, and G. E. Trahey, "Two Dimensional Ultrasonic Beam Distortion in the Breast: In vivo measurements and effects," Ultrason. Imag. 14(4), 398-414 (1992).
- [15] Q. Zhu and B. D. Steinberg, "Correction of Multipath Interference Using Coherent CLEAN Deconvolution Technique and Spatial Location Diversity," 1995 IEEE Ultrasonics Symposium Proceedings 13670-1370.
- [16] J. W. Goodman, *Introduction to Fourier Optics* (McGraw-Hill, New York, 1968).

Table I. Statistics of increase in -6 dB beamwidth (percent)

Sample size	Classification	Azimuth	Elevation
4	A	130 (std. 131.3)	100(std. 96.5)
3	B	50 (std. 53.3)	30 (std. 30.0)
9	C	30 (std. 33.3)	40 (std. 42.2)

A. Primarily scatter

B. More scatter than refraction

C. Scatter plus well-defined refraction

Table II. Statistics of refracted lobes from 9 *in vitro* breast samples

	Average	Std.Dev.
Number of refractive lobes	2	0.53
Relative peak strength (dB)	10	4.7
Distance from primary lobe (deg)	1.8	0.57

Table III Statistics of mainlobe diffraction shape (dB)

Diffraction pattern (dB)		Diffraction pattern after correction (dB)						
w/o correction	TDC	PC	Wideband DSA	BPT	PC &square rooter	BPT &square rooter	PC &fourth rooter	
A	-0(0)	-18.8 (1.9)	-19.0 (2.2)	-14.8 (2.6)	-24.3(2.1)	-25.3(3.0)	-29.5(2.7)	-32.3 (2.8)
B	-5.8(1.3)	-19.7 (2.3)	-19.7 (3.5)	-14.7 (1.5)	- 23.7(0.6)	- 25.3(2.1)	-29.3(2.3)	-30.7(1.2)
C	-6.1(3.5)	-19.3 (2.7)	-19.6 (2.5)	-14.8 (2.5)	-23.9(2.4)	-25.4(2.5)	-29.3(3.0)	-30.7(1.4)

Table IV Statistics of ER before and after corrections

w/o Corr.	TDC	PC	Wideband DSA	BPT	PC & square rooter	BPT &square rooter	PC &fourth rooter
214.7% (std.130.1%)	44.2% (13.4%)	25.1% (6.9%)	103.5% (33.9%)	12.8% (2.9%)	6.8% (1.6%)	3.7% (0.7%)	2.1% (0.4%)

Table V Relation of ER and image contrast (predicted and measured)

	w/o Corr.	TDC	PC	Wideband DSA	BPT	PC &square rooter	BPT &square rooter	PC &fourth rooter
ER	214.7%	44.2%	25.1%	103.5%	12.8%	6.8%	3.7%	2.1%
(predicted)	-10.2 (dB)	-17.1	-19.5	-13.3	-22.4	-25.2	-27.8	-30.3
(measured)	-4.2 (dB)	-19.3	-19.5	-14.8	-24.0	-25.4	-29.4	-31.1

FIGURES

DEABERRATION TRANSFORMATIONS

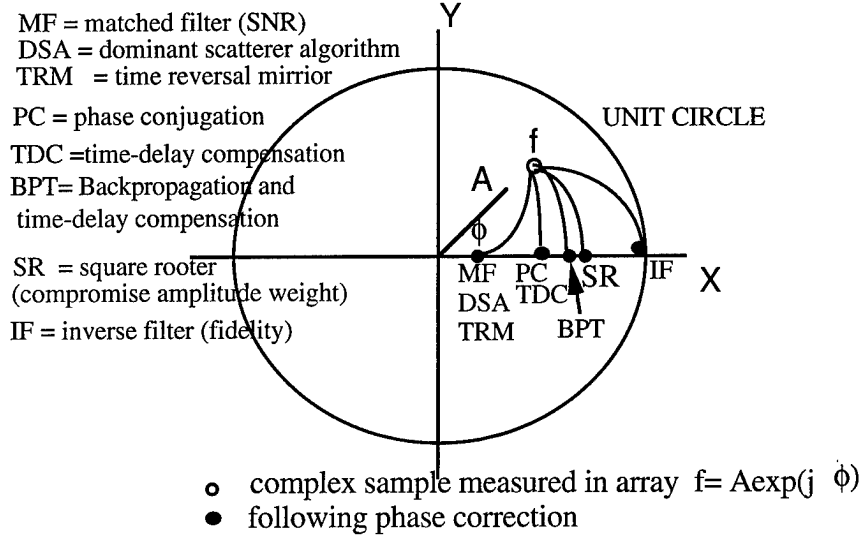


Fig.1. Deaberration transformations. \mathbf{f} is distortion vector for instantaneous sample of the radiation field. Transformations to the real axis all correct phase. Left (MF) maximizes SNR but increases amplitude distortion. Right (IF) maximizes imaging fidelity but increases noise. SR is good compromise.

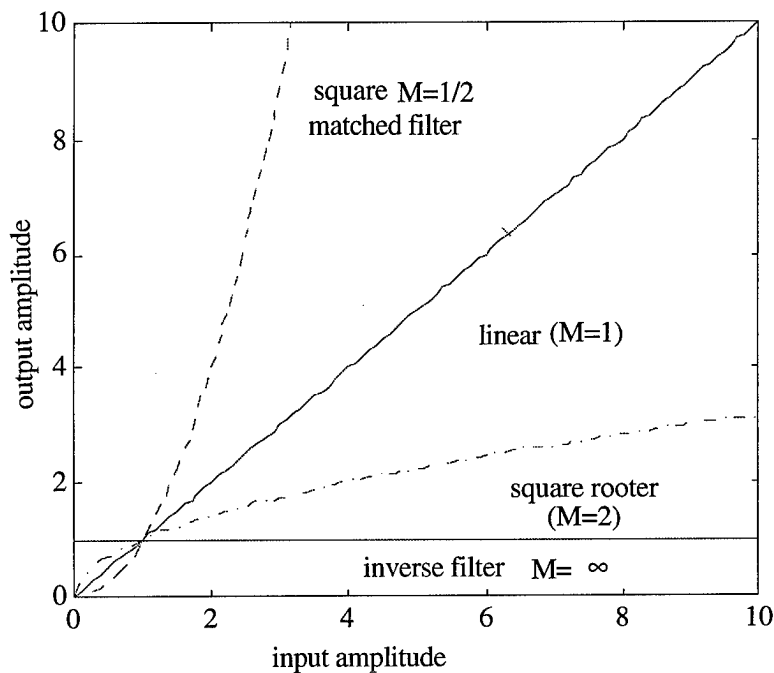


Fig.2. Plots of the input and output amplitude transforms.

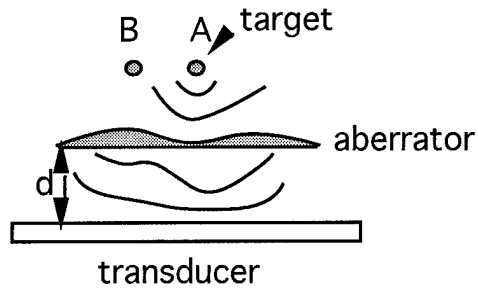


Fig.3. Illustration of scanning configuration.

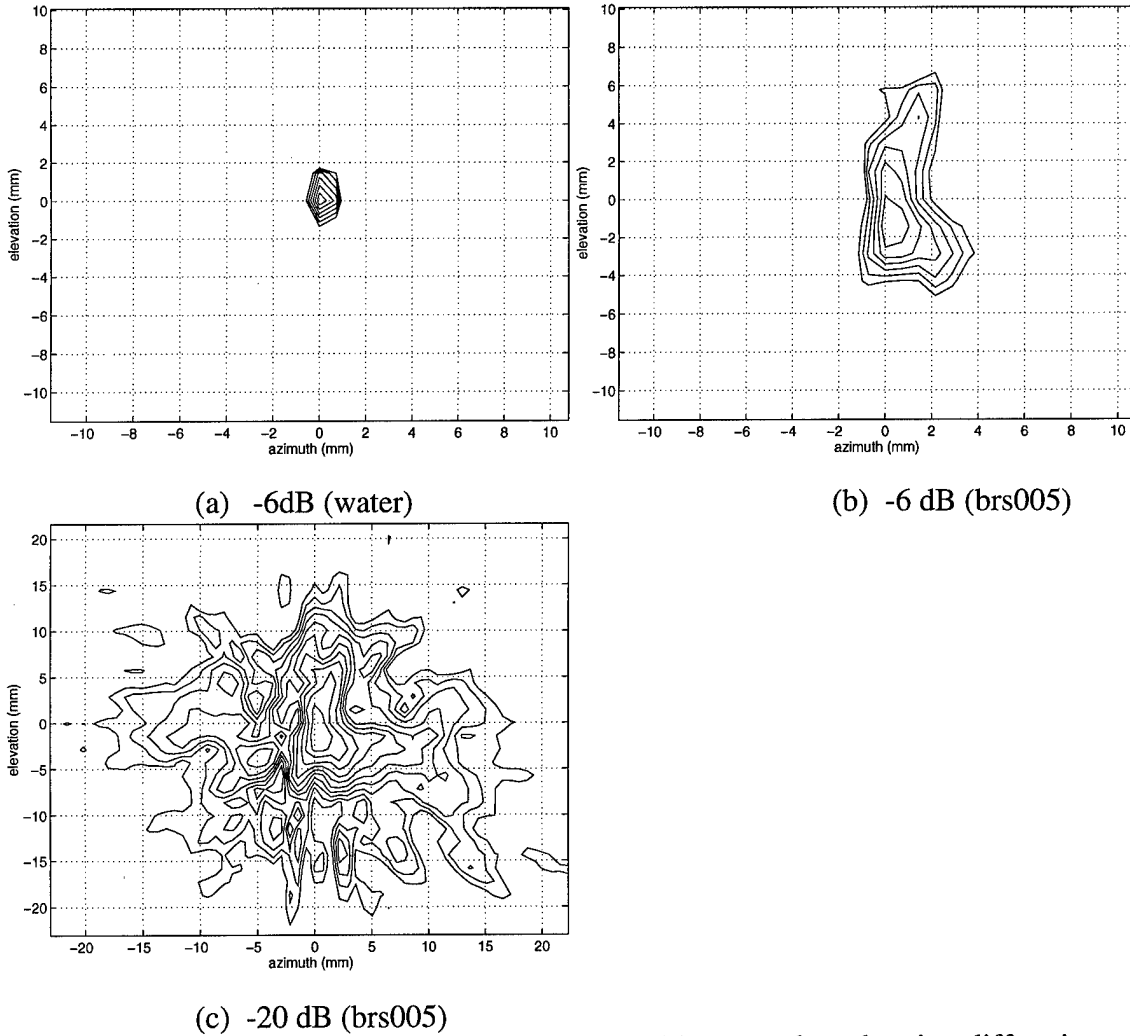


Fig.4. 2-D contour maps of point source images. (a) water data showing diffraction pattern of system. Outer contour is -6 dB level. (b) measured through the 3.5-cm tissue (brs005), showing asymmetric scattering effect. Outer contour is -6 dB level. (c) Image brs005 at -20 dB contour level. The outer contour shows symmetrical scattering pattern. No distinct structure or multipath is observed. Note the change of scale from (a) and (b).

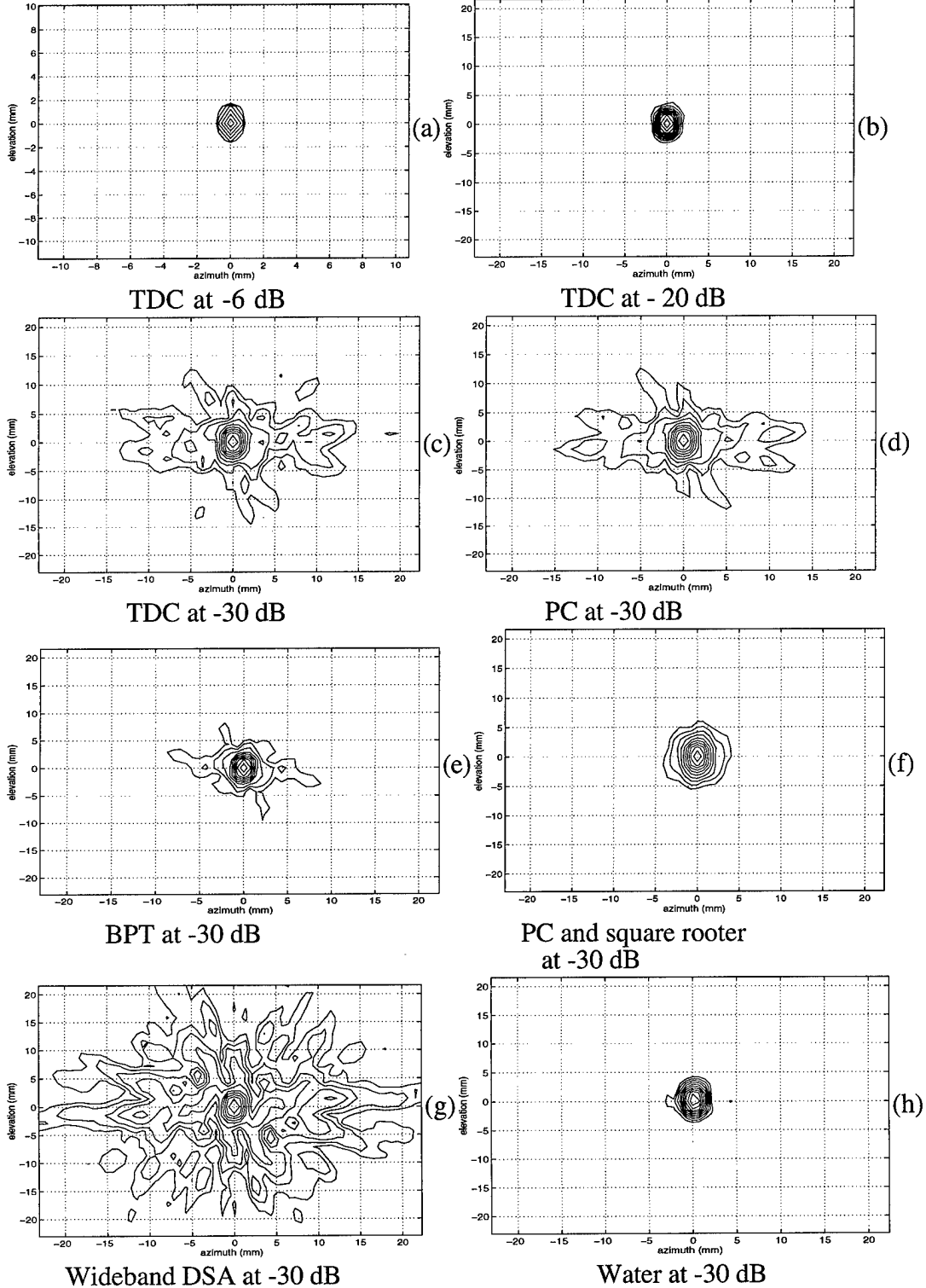


Fig.5. Distortion corrected contour maps of the sample image brs005 (see Fig.4(b) and (c) for comparison) (a) TDC at -6 dB. (b) TDC at -20 dB. (c) TDC at -30 dB. (d) PC at -30 dB. (e) BPT at -30 dB. (f) PC and square rooter at -30 dB. (g) Wideband DSA at -30 dB. (h) Water at -30 dB . Note the scale change of (b)-(h) from (a).

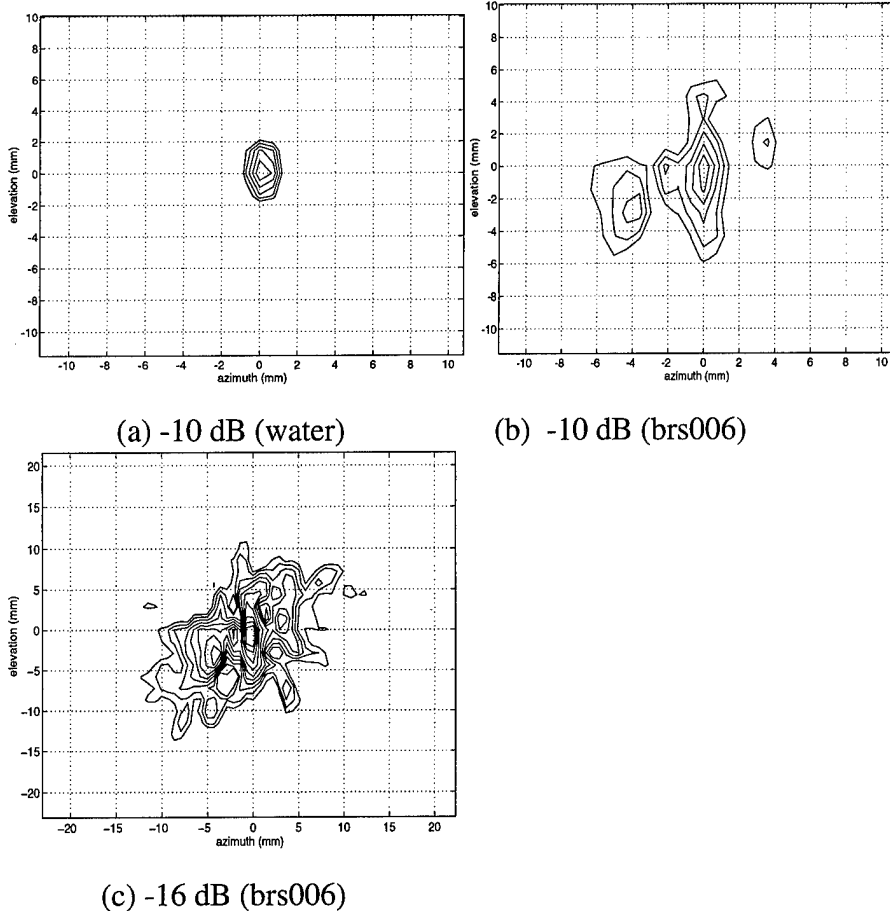


Fig.6. 2-D contour maps of point source images. (a) water data showing diffraction pattern of system. Outer contour is -10 dB level. (b) measured through the 4-cm tissue (brs006), showing highly asymmetric interference pattern. Outer contour is -10 dB level. (c) Image brs006 at -16 dB contour level. The outer contour shows more symmetrical scattering pattern. Note the change of scale from (a) and (b).

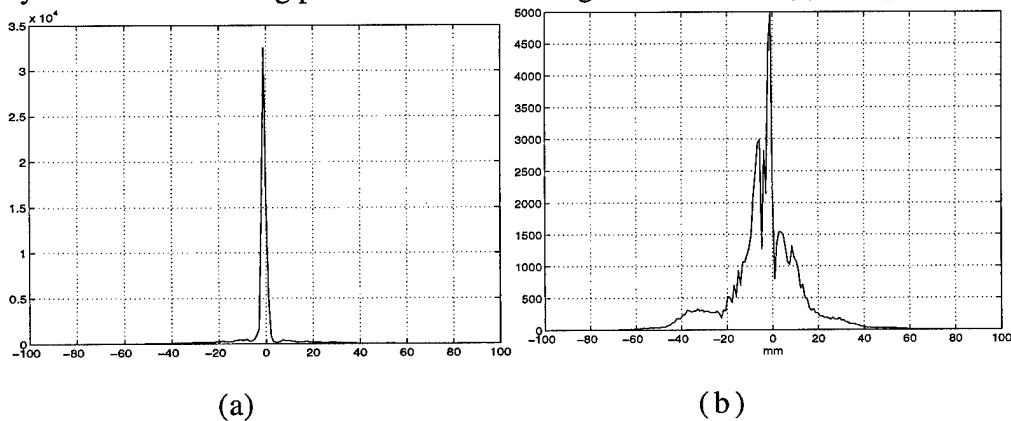


Fig. 7. (a) 45 degree cuts of 2-D images (a) water. (b) brs006.

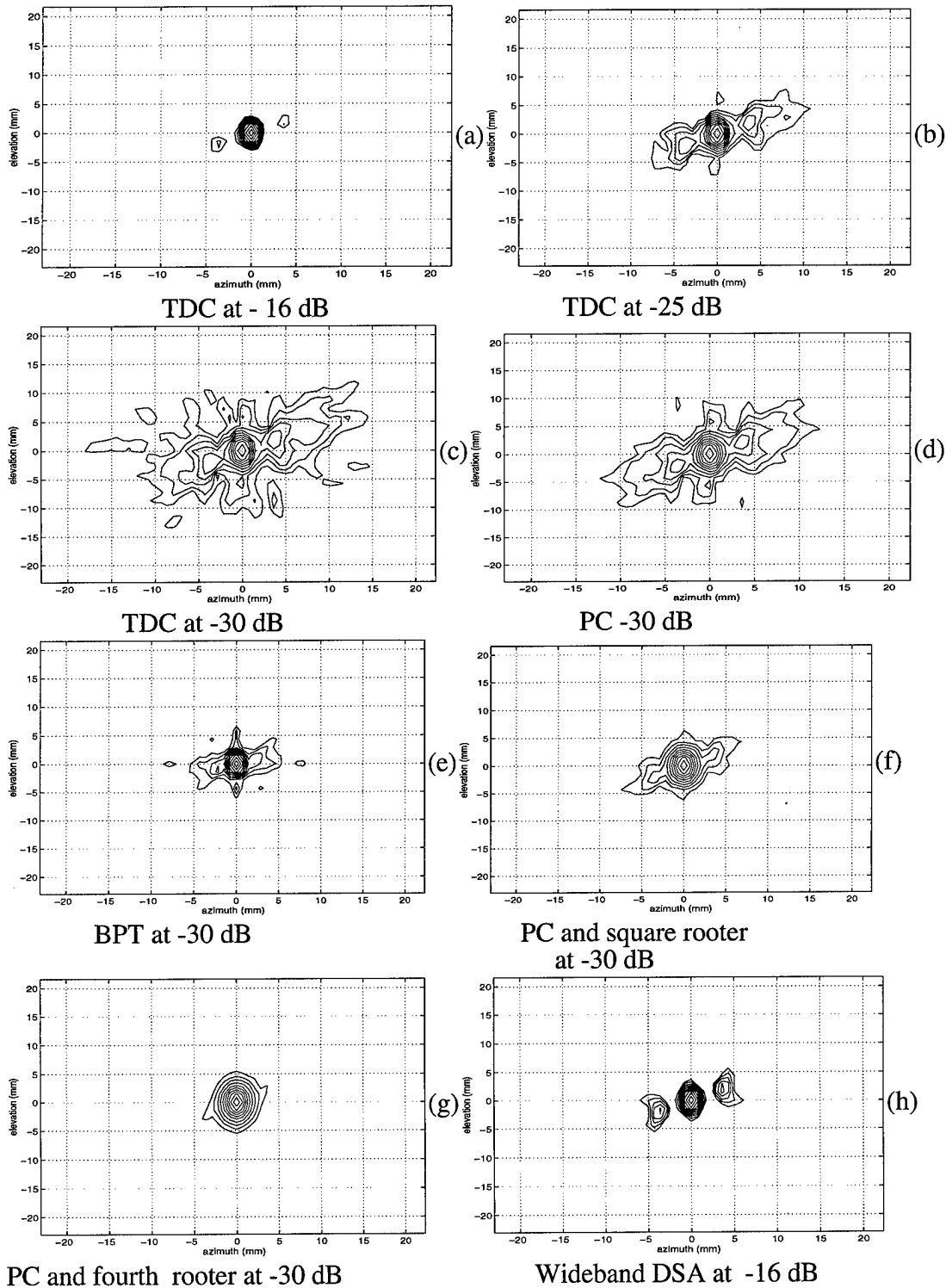
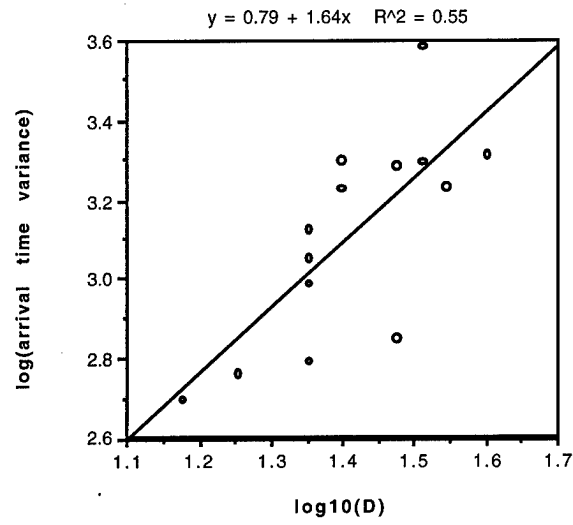
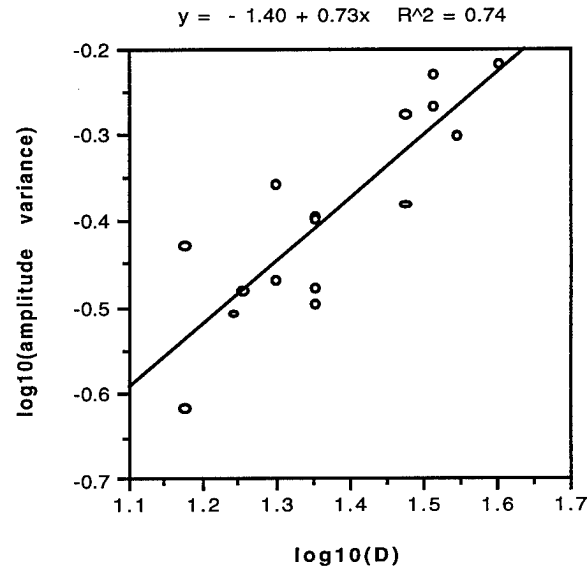


Fig.8. Distortion corrected contour maps of the sample image brs006 (see Fig.6 (b) and (c) for comparison) (a) TDC at -16 dB level. (b) TDC at -25 dB level and (c) TDC at -30 dB level. (d) PC at -30 dB level. (e) BPT at -30 dB. (f) PC and square rooter at -30 dB. (g) PC and fourth rooter at -30 dB. Wideband DSA at -16 dB. Artifacts are 5 dB higher than time-delayed correction shown in Fig.8(a).



(a)



(b)

Fig.9. Linear regression of (a) $\log(\sigma_{\tau}^2)$ vs. $\log(D)$ and (b) $\log(\sigma_{A_t}^2)$ vs. $\log(D)$. D is in mm, arrival time variance σ_{τ}^2 is in ns^2 and $\sigma_{A_t}^2$ is the normalized amplitude variance (no dimension).

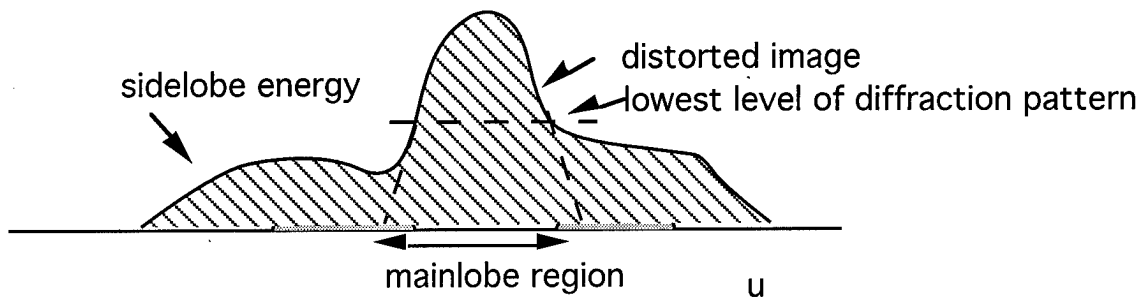
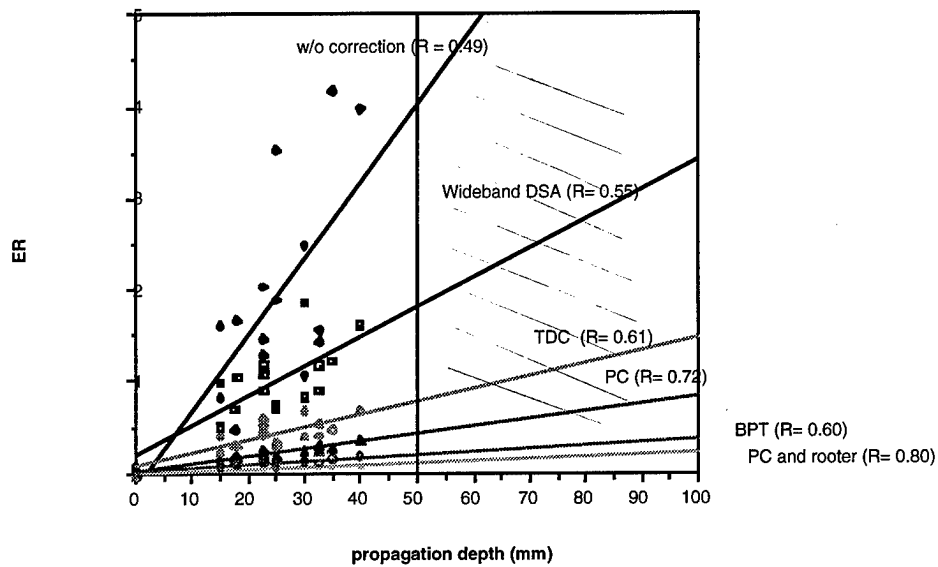
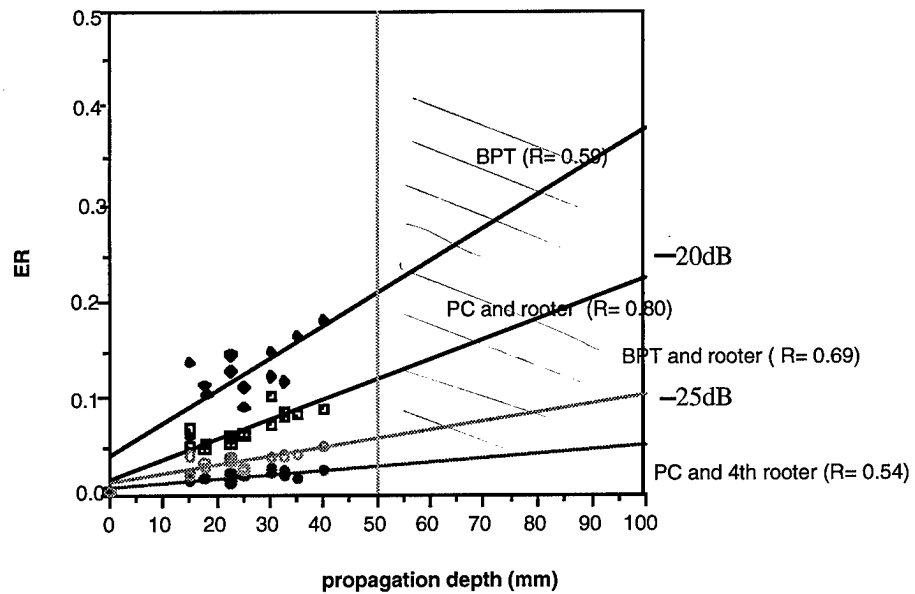


Fig.10. Illustration of ER measurement. Mainlobe region of distorted image is identified by extrapolating between image peak and the lowest level of diffraction pattern (see the two dashed lines). Mainlobe and sidelobe energies of the distorted image are obtained by integrating the energy inside and outside the mainlobe region.



(a)



(b)

Fig.11. (a) Linear regression curves of ER vs. propagation depth obtained from five correction procedures. (b) Results of ER vs. propagation depth obtained from four correction procedures. The vertical scales of part b is the predicted image contrast (see text).

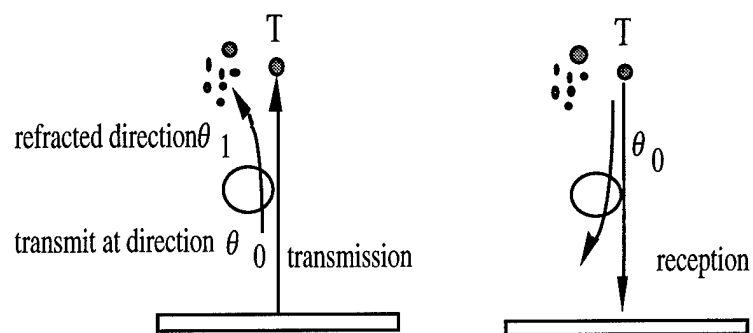


Fig.12. Illustration of effect of refraction upon pulse echo imaging (simplest case with no interference echo signal coming back from targets insonified by subbeam).

Correction of Multipath Interference Using CLEAN and Spatial Location Diversity

Qing Zhu, Radiology Department and Valley Forge Research Center
 Bernard D. Steinberg, Valley Forge Research Center, Electrical Engineering Department
 University of Pennsylvania, PA 19104

1. INTRODUCTION

Previous studies indicate that ultrasonic wavefront distortion inside the female breast falls into two categories, incoherent scattering and coherent multipath. Scattering reduces target strength, broadens image lobe and lowers the image contrast while refraction creates coherent multipath interference that produces false targets in the image. Time-delay type compensation algorithms are useful to minimize scattered energy and to improve image contrast to a large extent (15 dB) [1]. Further improvement of contrast resolution requires compensation algorithms that can remove false targets. Multipath interference is a much more difficult problem than scattering. Because it is not a stationary, stochastic process, two distinct steps are required to deaberrate refraction-contaminated image. It is first necessary to recognize which target is the true target and which is the false one caused by interference. In Section 2 we demonstrate that when a cluster of true and false targets is imaged from several different array locations the true target remains in position and changes very little in size and shape. The images of false targets, on the other hand, are highly sensitive to the direction from which they are viewed. Therefore, they change sufficiently in location, size and shape to classify them as false. In this way the recognition problem is solved. The second key problem is the elimination of the multipath arrivals. In Section 3, we show that coherent clean technique can be used as a tool to solve the second problem.

2. RECOGNITION OF TRUE TARGETS

A. Diversity Principle

We have found that geometric techniques may be able to separate nonisotropic from isotropic scattered energy. Fig.1 illustrates the case where a single source and 1-D reception are used for descriptive convenience. The same principle is applicable to a multiple source distribution and 2-D configuration. A source radiates into a scattering and refractive medium and its radiation field is received by a receiving aperture. The source image obtained from any aperture is the superposition of the image lobe, image artifacts caused by coherent interference and an incoherent scatter spectrum. The location and shape of the image lobe generally remains

the same when viewed from different apertures, such as the left and right halves of the aperture, while the locations, sizes and shapes of the image artifacts are likely to change because the fields intercepted by different subapertures encounter refractive bodies with different orientations, curvatures and sizes. The incoherent spectrum is statistically the same in each subaperture image. Therefore, the locations and shapes of the large lobes in different subaperture images can be used to distinguish the image lobe from image artifacts. We found experimentally that 2-D large subarray diversity images are in general useful for identification while 1-D subarray images fail to provide identification most of the time because of incomplete distortion information.

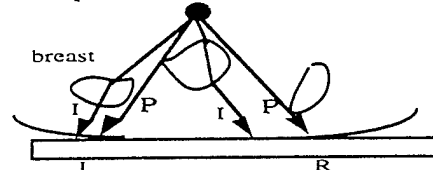


Fig.1 Illustration of diversity. P refers primary field and I interference field. The interference fields change with propagation path.

B. 2-D Experiments

To develop an understanding of deaberration, our studies have concentrated on one-way propagation measurements and corrections of point source fields. The 2-D measurement system and procedure were described in [2]. Briefly, a breast specimen was placed between hemispherical source and receiving array. The 2-D array consisted of a 92-mm 1-D linear array translated 46 mm perpendicular to its axis to form a synthetic 2-D array 92 mm x 46 mm. Element pitch in the receiving transducer was 0.72 mm and a reflecting mask reduced the receiving elevation to 1.44 mm. Frequency was 3.7 MHz. Bandwidth was 2 MHz. Waveforms were measured at each element, from which 2-D wavefronts were reconstructed as functions of time. 3-D image data were calculated by (1) Fourier decomposition of the temporal waveforms at each (x,y) position in the aperture, (2) calculation of a complex CW 2-D image at each Fourier frequency in the focal plane by using the angular spectrum technique, and (3) summation of the 2-D images to form the 3-D transient image.

C. In Vitro Example

Fig. 2 shows an example of single-frequency diversity images. Part (a) is the -20 dB contour plot of 2-D water path image. It is the system diffraction pattern at that contour level. Part (b) is the -20 dB contour plot of the 2-D image of a 4 cm tissue path (brs006) obtained from the entire aperture (92 mm by 46 mm), and (c) is the -20 dB contour of the same image after applying time-delay correction. The improvement is significant because of partial removal of scattered energy. Large multipath lobes remain and decrease image contrast. (d)-(g) are obtained from four subapertures after applying time-delay correction. The real target remains in the same location. False targets move and change size and shapes when viewed from the different subapertures. For example, the lobe with -13 targets located at (4.3 mm, 2.9 mm) in (c) does not appear in (d), therefore it is a false target and should be removed.

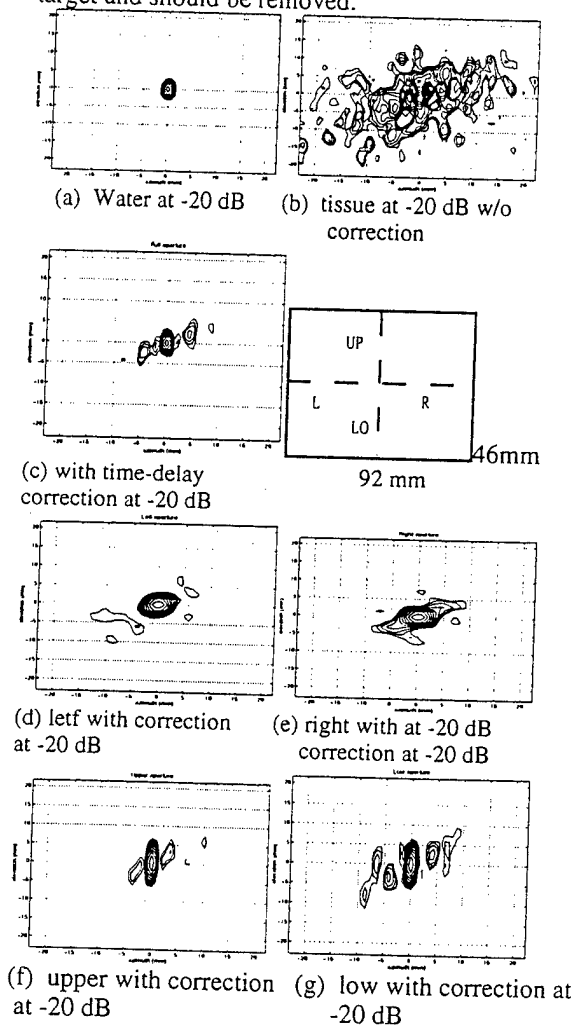


Fig.2 Quadruple spatial diversity discloses false targets. Images are obtained at central frequency. Contour maps are at -20 dB level. Real target remains

in place in subarray images while multipath target changes location, size and shape. (a) Contour map of water path image. (b) Contour map of full-aperture tissue image (brs006) at -20 dB. (c) Contour map of the full-aperture image brs006 at -20 dB after time-delay correction. (d) Image from left half of array. 46x 46 mm. (e) From right half. (f) From upper half (23x92mm). (g) From low half. Point source remains in center in all images. Shape change is due to the change of aperture size.

3. COHERENT CLEAN

A. CLEAN

CLEAN is a nonlinear deconvolution procedure originated in radio astronomy in the 1960s [3], extended to radar by Tsao and Steinberg [4] and applied to ultrasound by Cohen (1992) [5]. The simplest CLEAN procedure is described as following. The diffraction pattern $f(u)$ is shown upper left in Fig.3. The procedure begins with the original dirty image $A_0(u)$ (Fig.3a). The strongest source is found and its complex amplitude a_0 and coordinates u_0 are measured. An image of that source is found by convolving the radiation pattern with a δ -function of strength a_0 located at u_0 . Some fraction of this image is subtracted from $A_0(u)$. The result of this first iteration is a new image, $A_1(u)$, from which all energy from the strongest source has been removed, including its sidelobe energy (Fig.3b). The process continues until the subtraction procedure produces images with negative values or increases energy in the residual image. The result at this stage is a list of detected sources. The next step is to calculate a CLEAN beam that has the resolving power of $f(u)$ but without its sidelobe distortion. The final image is the convolution of the CLEAN beam and each of the detected sources (Fig.3c).

However, the CLEAN procedure cannot be directly applied to an image that is contaminated by image artifacts, because CLEAN will pick up true targets as well as false targets. A clever use of CLEAN is the following.

Step 1 (descattering): Apply time-delay type descattering algorithms upon each diversity image and original image to reduce the scattering induced distortion upon images. This descattering procedure strengthens targets (see Fig. 2(b) and (c)) and improves the performance of CLEAN by providing better target subtraction and consequently exposing more weak targets.

Step 2 (coherent CLEAN): Clean each diversity image and the full aperture image using the approximate system diffraction patterns of the corresponding subarray and the full array.

The result is a set of lists of targets (real and false). Each list is a CLEANed result of each diversity image.

Step 3 (location diversity): Select targets which appear on all lists by using location or neighborhood matching procedures. These targets are considered as true targets.

Step 4 (image reconstruction): Reconstruct a full aperture image from the true targets.

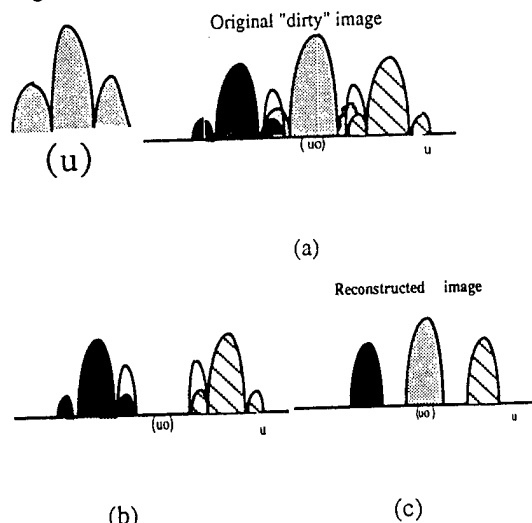


Fig. 3. Illustration of the clean procedure. (a) "Dirty image" of three point targets is the envelope of the coherent sum of the three images. (b) After the first iteration of the clean procedure. The strongest target is subtracted out as well as its sidelobes. Final result of cancellation process is a list of targets (strengths and locations) $A_i \delta(u - u_i)$. (c) Final reconstructed image = $\sum_i A_i \delta(u - u_i) * f(u)$.

The above CLEAN procedure was done at each frequency except for Step 1 which was done in time domain before the Fourier decomposition. The 3-D transient image was obtained by summation of the 2-D CLEANed images at all discrete frequencies obtained from Step 4.

Also, CLEAN is *modified* to change the diffraction pattern $f(u)$ to produce better subtraction result at each iteration. We call this modified CLEAN procedure MCLEAN in the following text. MCLEAN differs from CLEAN in step 3.

B. Experimental Results

Fig. 4 is the CLEANed image of Fig. 2(c) at -30 dB contour after step 2. CLEAN has picked up 30 false targets in addition to the true target. After location diversity, all false targets

are identified. Table I gives the identification result of this example. Each triple represents the x and y locations of the target in mm in full-aperture image identified by CLEAN, and corresponding matching result in bold letter. For example, the first triple indicates that the target located at (0.0 0.0) appeared in four subapertures and therefore can be identified as true target. The 2-D neighborhood distance used

for matching is calculated as $R \sqrt{\left(\frac{\lambda}{L_1}\right)^2 + \left(\frac{\lambda}{L_2}\right)^2}$,

where aperture dimensions L_1 and L_2 are 46.08 mm and 92.16 mm, R is the focussing distance and λ is the wavelength of each discrete frequency. No misclassification occurs in this frequency. The peak of the noise floor after CLEAN is 23.4 dB lower than the peak value before CLEAN. Since the original peak artifact to peak target ratio is -13.0 dB, the dynamic range has been improved by 10.4 dB using MCLEAN. MCLEAN has been repeated on all 39 discrete frequencies. Two misclassifications occur in two CW images. In one case, a false target was identified as true and in another true was identified as false. However, these cases happen in CW images obtained from the low and/or high frequency ends where the signal to noise ratio is low. Fig. 5(a) is the MCLEANed wideband sample image, after peak detection of the 3-D transient image, at -30 dB level. Fig. 5(b) is the wideband water path image at -30 dB for comparison. The false target which appeared at one frequency does not contribute much to the final wideband image because of its low strength. The true target, which was identified as false, was removed at step 4 before the summation to form the 3-D wideband image. The result is the 0.01 dB reduction of the true target strength compared with its strength before MCLEAN. The peak of the wideband noise floor after MCLEAN is -25.1 dB lower than the peak value of the true target before MCLEAN. Since the peak artifact to peak target ratio in wideband image before MCLEAN is -14.5 dB, the dynamic range has been improved by 10.6 dB by MCLEAN.

The average location of the true target in all frequencies in this example is (0.0 mm, 0.0 mm) with (0.73 mm, 0.82 mm) or $d = 1.1$ mm perturbation, which is well within the weighted neighborhood distance

$$\frac{\sum (\lambda_i R \sqrt{(\frac{\lambda_i}{L_1})^2 + (\frac{\lambda_i}{L_2})^2})}{\sum \lambda_i} = 7.9 \text{ mm over all}$$

frequencies. This implies that spatial diversity is an effective method for identification of true target.

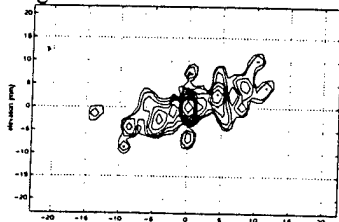


Fig. 4. Reconstructed image of Fig. 2(c) at -30 dB level after step 2 coherent CLEAN.

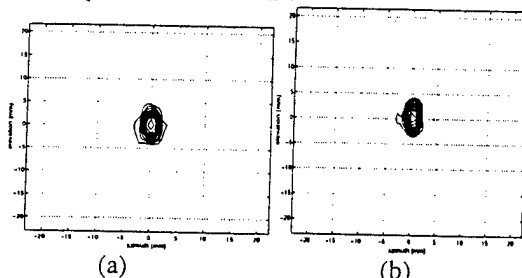


Fig. 5. (a) -30 dB contour of 3-D transient MCLEANed image of brs006 after peak detection. (b) -30 dB contour of 3-D transient water path image after peak detection.

Table I. Locations of the targets and results of spatial matching

(0.0, 0.0, 4),	(4.3, 2.9, 3),	(-4.3, -2.9, 3),
(-2.2, -1.4, 2),	(2.2, 0.0, 2),	(-5.0, -4.3, 0),
(-4.3, -1.4, 0),	(8.6, 4.3, 1),	(5.0, -1.4, 0),
(7.9, 0.0, 2),	(-8.6, -4.3, 0),	(3.6, 1.4, 1),
(-6.5, 0.0, 1),	(-0.7, 2.9, 0),	(4.3, 7.2, 0),
(1.4, 2.9, 0),	(-5.8, 1.4, 0),	(7.2, 5.8, 0),
(11.5, 4.3, 0),	(-2.2, 1.4, 1),	(-7.2, -1.4, 0),
(9.4, 8.6, 0),	(10.1, 10.1, 0),	(-13.7, -1.4, 0),
(0.0, -7.2, 0),	(0.0, 7.2, 0),	(5.8, -2.9, 1),
(10.8, 2.9, 0),	(-9.4, -8.6, 0),	(0.0, -4.3, 0),
(-2.2, -4.3, 0),		

The bold number in each triple is the matching result.

The statistics of the performance of MCLEAN upon 7 samples with well-defined multipath artifacts are given in Table II. The data are self explanatory.

4. DISCUSSION/CONCLUSION

2-D spatial diversity images are useful for identification of true target vs. refractive artifacts. Cohere CLEAN in conjunction with diversity is a useful tool to reconstruct artifact-free high resolution images. The preliminary results with 7 in vitro samples show 7.3 dB

dynamic range improvement with negligible target strength change.

The diffraction pattern used in this report was only modified by varying the focusing speed to match the distorted mainlobe as well as refractive lobes to obtain better subtraction in step 2. The dynamic range can be further improved if the diffraction pattern is modified by perturbing higher order focusing terms to improve the subtraction. This is a subject of for future study.

Table II. Statistics of MCLEAN of 7 breast samples

Target strength reduction (dB)	0.06 (std. 0.06)
Dynamic range improvement (dB)	7.3 (std. 1.92)
Location stability of true target (mm)	1.7 mm (std. 2.9)
Misclassification:	
True as false	4.0% (std. 3.9%)
False as true	11.0% (std. 12.7%)

ACKNOWLEDGMENTS

The *in vitro* measurements were done with the collaboration of Ms. Laura M. Hinkelman and Prof. Robert C. Waag, Departments of Electrical Engineering and Radiology, University of Rochester, Rochester. Invaluable comments were given by Dr. Kai Thomenius, Director of Research, Interspec, Inc., Ambler, PA., a division of ATL. Funding was provided by the Army (DAMD 17-93-J-3014 and DAMD 17-94-J-4133) and NSF (BCS92-09680).

REFERENCE

- [1] Q. Zhu, B. D. Steinberg, "Modelling and Correction of Incoherent Wavefront Distortion," submitted to International Journal of Imaging Systems and Technology (Sept. 1995).
- [2] L. M. Hinkelman, D-L. Liu, and R. C. Waag, Q. Zhu, and B.D. Steinberg, "Measurement and Correction of Ultrasonic Pulse Distortion Produced by the Human Breast", J. Acoust. Soc. Am. 97(3), 1958-1969 (1995).
- [3] Hojbom, J. A., "Aperture Synthesis with Non-Regular Distribution of Interferometer Baselines," Astron. Astrophys. Suppl., Vol. 15, pp. 417-426, 1974.
- [4] Tsao, J. and B.D. Steinberg, "Reduction of Sidelobe and Speckle Artifacts in Microwave Imaging: The Clean Technique," IEEE Trans. Antennas and Prop., Vol. 36, No. 4, April 1988, pp. 543- 556.
- [5] Cohen, N., "Practical real-time deconvolution and image enhancement of medical ultrasound," Biological Image Processing and 3D Microscopy, ed. by R. Acharya, C. Cogswell and D. Goldgof, SPIE, Bellingham WA 1992.